University of Alberta

Magnetotelluric Imaging of Precambrian Lithosphere Beneath Southern Alberta

by

Greg Nieuwenhuis

A thesis submitted to the Faculty of Graduate Studies and Research
in partial fulfillment of the requirements for the degree of

Master of Science
in
Geophysics

Department of Physics

©Greg Nieuwenhuis

Fall 2011

Edmonton, Alberta

Examining Committee

Dr. Martyn Unsworth, Department of Physics, Earth and Atmospheric Sciences

Dr. Thomas Chacko, Department of Earth and Atmospheric Sciences

Dr. Claire Currie, Department of Physics

Dr. Larry Heaman, Department of Earth and Atmospheric Sciences

Abstract

Magnetotelluric (MT) data were collected at 67 stations during the 2008, 2009, and 2010 field seasons in southern Alberta. These have been combined with more than 300 MT stations previously collected in Alberta, allowing a three dimensional electrical resistivity model of the lithosphere to be developed to depths of 250 km. Initial modelling attempts of the MT data in southern Alberta showed that two dimensional data analysis could not be used to model these data. Therefore this study was undertaken to determine a three dimensional model that fits the data.

The resulting 3-D resistivity model has shown a regionally pervasive conductor in the upper mantle below the Loverna Block, coincident with a north dipping reflector. A similar regional conductor and north dipping reflector occurs below part of the Medicine Hat Block, further characterizing the Precambrian subduction zones below southern Alberta.

Acknowledgements

Table of Contents

List of figures

Figure 3.2: Maps of the MT stations collected throughout Alberta, (a) data collected in the 1960's, (b) shows the data collected in the 1970's and 1980's. The large dots indicate the approximate location of historical MT data in Alberta (where they are split, data was either collected for more than one study, or the same data was used for both studies). (a): the white dot is from Niblett & Sayn-Wittgenstein (1960); red dots are from Vozoff et al. (1963); blue dots are from Srivastava et al. (1963); orange dots are from Vozoff & Ellis (1966); and the yellow dot is from Rankin & Reddy (1969). The red lines indicate the direction of minimum apparent resistivity, and the blue lines indicate the direction of maximum apparent resistivity (from Srivastava et al., 1963). (b): the purple and blue dots are all from Reddy & Rankin (1971), the blue dots indicate the first measurements of the Red Deer Conductor (see further text); the purple line shows the location of the profile over the Vulcan Structure by Peeples & Rankin (1973).

Figure 3.3: From Rankin & Reddy (1969); a depiction of the polarization of the electric field at a station near Kavanagh (Figure 3.2). Each dot represents a vector measured at a specific point in time, and the elliptical spread of the dots represent how polarized the measured electric field is (ellipticity), and at what direction it is polarized (azimuth).

Figure 3.4: Apparent resistivity sounding curves measured by Vozoff et al. (1963) near Edmonton, displayed in the measurement coordinate system. The Cooking Lake station (a) shows little difference between the xy and yx modes, while the Kavanagh station (b) shows a large split between the modes. This was originally referred to as anisotropy, but is likely caused by 2-D or 3-D structure. The phase was not calculated for these soundings, likely because the data was too noisy. (Note that the original soundings had the xy and yx data opposite to what is shown here, i.e. the xy displayed here is the yx displayed in the original study).

Figure 3.5: MT sounding from Leduc collected by Rankin & Reddy (1969), displayed in the measurement coordinate system. The split between the modes always begins at a period near the top of the Precambrian basement.

Figure 3.6: From Vozoff & Ellis (1966), displayed in the measured coordinate system (x is north). This sounding was been collected near Brooks (Figure 3.2), the theoretical model is based on the yx data, since the electric field in the x direction (north) had a low signal level (corresponding to a low coherency in the xy mode). The $\boldsymbol{Hx} - \boldsymbol{Ey}$ points are the yx mode, and the $\boldsymbol{Hy} - \boldsymbol{Ex}$ points are the xy mode.

The PC label on the theoretical model represents the location of the Precambrian basement rocks.

Figure 3.7: From Vozoff & Ellis (1966), sounding collected at Beiseker again showing very few points from *xy* mode due to low signal in Ex (where x points north). The PC label on the theoretical model represents the location of the Precambrian basement rocks.

Figure 3.8: From Vozoff & Ellis (1966), MT sounding collected from near the town of Vulcan (in the measurement coordinate system – x points north). The PC label on the theoretical model represents the location of the Precambrian basement rocks.

Figure 3.9: From Reddy & Rankin (1971); solid vector lines represent the maximum apparent resistivity angle at a period of 200 seconds, and the dotted vector lines represent the angle of electric field polarization at stations where apparent resistivity curves were impossible to determine. The contour lines represent the depth of the sedimentary basin.

Figure 3.10: From Reddy & Rankin (1971); Apparent resistivity curves from 16 stations located in central Alberta (see Figure 3.2 or Figure 3.9 for locations). These show the apparent resistivity curves obtained from rotating each station to their maximum apparent axis. The top is the apparent resistivity in the direction of maximum apparent resistivity, while the bottom shows the apparent resistivity in the minimum direction.

Figure 3.11: Reproduced from Reddy & Rankin (1972); The top shows a 2-D model used to generate the *xy* and *yx* curves in the bottom figure (at point 'P'). The result from 1-D modelling assuming no horizontal boundaries in the model is shown as a dotted line.

Figure 3.12: From Peeples & Rankin (1973); A profile oriented from north to south across the Vulcan Structure (see Figure 3.2). The top figure shows the TE mode pseudo section, and the bottom figure shows the TM mode pseudo- section. The Vulcan Structure occurs directly beneath Location 5, with Location 7 to the north, and Kilcardy to the south.

Figure 3.13: The gradient of the total residual magnetic field in the background, the southern Alberta British Columbia (SABC) conductor defined by Gough (1986a) is shown by the honeycombed area, the SABC line current model from (Wang, 1988b) is the large gray line, and the bold black line shows the Red Deer Conductor along the edge of the Lacombe Domain (Boerner et al., 2000).

Figure 3.14: From Boerner et al. (2000). Map showing the locations of the Lithoprobe ABT data collected throughout Alberta. Several profiles are denoted, as is the general location of the Southern Alberta - British Columbia (SABC) conductor. The filled in circles indicate stations collected by Reddy & Rankin (1971) which are affected by the RDC.

Figure 3.15: Redrawn from Jones et al. (2002), Geoelectric complexity of MT stations collected as part of the Lithoprobe Alberta Basement Transect, gray shaded area is the location of a strong conductor present in the TE mode data (with a strike direction of N45°E), and the location of the Red Deer Conductor (RDC) is based on the 2-D MT inversions by Boerner et al. (2000). At a relatively short period of 213.3 seconds (a), the data shows 3-D effects associated with the RDC and the Paleoproterozoic terranes to the north. The long period MT data of 1280 seconds (b) shows 3-D effects widespread throughout the Archean Loverna Block, which appear to be associated with the TE conductor indicated by the gray shading.

Figure 3.16: A 1-D MT sounding from southern Saskatchewan. Both TE and TM curves shows a very similar structure to the TM modes collected near the RDC and within the Loverna Block. This sounding has been rotated to N45°E.

Figure 3.17: MT sounding which characterizes the conductor denoted by the gray area in Figure 3.15. Similar to the RDC sounding in Figure 3.20, the conductor only affects the TE mode, and the TM mode shows a very similar structure to many other places in Alberta. (The sounding has been rotated to a strike angle of N45°E).

Figure 3.18: From Boerner et al. (1999). The results of a 2-D isotropic inversion of the TM mode data along profile D-D' in Figure 3.14. Note that gray represents low resistivity, and white is high resistivity. The upper mantle underlying the Archean Loverna Block is an order of magnitude less resistive than the upper mantle underlying the Proterozoic terranes to the northwest.

Figure 3.19: From Boerner et al. (2000); Inversion results from three profiles which cross the RDC in central Alberta (profile locations are in Figure 3.14). The profiles show unrealistic structure which does not fit either mode very well.

Figure 3.20: MT soundings collected near the RDC. On the left the sounding ABT070 collected as part of the Lithoprobe ABT project very close to the axis of the RDC. The right plot shows SAB110, an MT sounding collected further from the axis of the RDC than ABT070, but still indicating the effects from the RDC.

Both soundings have been rotated following the strike of the RDC (coordinate system rotation of N45°E), and both show an obvious notch around 100 seconds in the TE mode.

Figure 4.1: Map of the long period MT stations in southern Alberta. Black dots represent the Lithoprobe ABT data, red dots are the SAB stations collected by the University of Alberta as part of this thesis.

Figure 4.2: (a) - map view of an typical MT setup, (b) – MT equipment used by the University of Alberta. Photo courtesy of Ted Bertrand.

Figure 4.3: An example of the time series collected at a long period MT station (sab140). This section of time series was collected on October 8, 2010 between about 5 and 6 am (this section of time series is 5,000 seconds long). The top three channels are the magnetic field in the x, y, and z directions, the bottom two channels are the electric field in the x and y directions.

Figure 4.4: MT sounding curve obtained from station SAB140. The top panel shows apparent resistivity, the second panel shows the phase, and the two bottom panels show the tipper (T_{zx} and T_{zy} respectively).

Figure 4.5: Southern Alberta can be generally characterized by three different types of MT soundings. In the south (dark gray), the Medicine Hat Block is characterized by relatively 1-D MT data, The Vulcan Structure and eastern Loverna Block show a split in the TE and TM modes which is relatively consistent to long periods, the western Loverna Block shows affects from a conductor in the TE mode, but none in the TM mode, and north of the Loverna Block there is a split between the modes, but they both show effects from the conductive asthenosphere at long periods.

Figure 4.6: Regional strike determination for data in southern Alberta. (a) shows strike directions for the period range of 1 to 1000 seconds, (b) shows strike directions determined for the period band 1000 to 10,000 seconds. The rose diagrams in (c) and (d) are stacked images of all the strike directions in southern Alberta, and the misfit map in (e) shows the small misfit values which result from trying to fit the data in the period band 1000s to 10,000s.

Figure 4.7: Rose diagrams of strike angles within the period range 1000s to 10,000s for each 1° by 1° block in southern Alberta. The strike angles show a large change between different regions, indicating the difficulty for 2-D data analysis to accurately describe this data.

poor fit which characterized many of the initial models. The right sounding shows the response from the final model.

Figure 5.16: This model could not fit the data along the Rocky Mountain foothills. The depth slice on the right shows a slice from within the sedimentary basin. Since the inversion could not fit the data with a realistic model, it has placed an unrealistic conductor in the sedimentary basin. The top left shows an east-west profile through this very large feature with very low resistivity, and the north-south profile shows the extent of this feature. The data was not fit well with this model.

Figure 5.17: A model generated from a length scale of 0.8. The left shows a map of the resistivity at a depth near 200km, and the right shows an east-west oriented profile taken from the model. The black line and box mark the location of each profile and depth slice in relation to one another. With this length scale value the deep structure shows extreme highs and lows, and seems to be smeared into depth.

Figure 5.18: A comparison of two models generated with different initial models. The left is with a 100 Ω-m half space initial model, and the right is with a model including a 30 Ω-m asthenosphere at ~240 km depth. The top shows a map from both models of the resistivity at a depth ~215 km. The middle shows north-south profiles from the models, and the bottom shows east-west profiles. The black lines indicate where the slices intersect one another.

Figure 5.19: Maps of the residual, calculated as the difference between the observed data and model data, displayed as a percentage of the observed data (0.5 is 50%). The top two maps are from the same models as displayed in Figure 5.18, and the bottom map is from a model with a smaller error floor (10% diagonal, and 5% off-diagonal).

Figure 5.20: Examples of the data fit obtained by the 3-D model. The map in the middle indicates where each sounding is located. The small circles are the measured data, and the solid lines are the 3-D model responses.

Figure 5.21: Residuals after the data and responses have been rotated to N45°E from the final model.

Figure 5.22: Three soundings from along Line 2. The top left shows the 2-D and 3-D models, and each sounding shows a comparison between the measured data

List of symbols and abbreviations

1-D	One Dimensional
2-D	Two Dimensional
3-D	Three Dimensional
ABT	Alberta Basement Transect
GFTZ	Great Falls Tectonic Zone
GSLZ	Great Slave lake Shear Zone
LAB	Lithosphere - Asthenosphere Boundary
LIMS	Long period Intelligent Magnetotelluric System
MHB	Medicine Hat Block
MT	Magnetotelluric
MV	Magnetovariational
NIMS	Narod Intelligent Magnetotelluric System
RDC	Red Deer Conductor
SAB	southern Alberta
STZ	Snowbird Tectonic Zone
TE	Transverse Electric
THO	Trans Hudson Orogen
TM	Transverse Magnetic
VS	Vulcan Structure
WCSB	Western Canada Sedimentary Basin

Chapter 1

Introduction

The majority of Alberta is covered by rocks of the 2-3 km thick Western Canada Sedimentary Basin (WCSB).These sedimentary rocks have been studied extensively owing to their economic potential, while the Precambrian basement rocks which underlie them remain relatively unexplored. Much of what is known about these rocks is from drill core which penetrated the very top of the Precambrian rocks, originally studied by Dr. Ron Burwash (e.g. Burwash et al., 1962). Our understanding of these Precambrian rocks was expanded by a correlation of geochronological ages with regional potential field data (Ross et al., 1991). In the 1990's the Lithoprobe Alberta Basement Transect sought to learn more about these rocks through crustal scale seismic surveys and magnetotelluric (MT) studies (Ross, 2000).

The Lithoprobe MT studies showed that the MT data that sampled the crust underlying Alberta were not easily modelled with a two dimensional (2-D) approach (Boerner et al., 2000; Jones et al., 2002). A three dimensional (3-D) study was needed to understand the electrical structure of the crust, and therefore this thesis was undertaken. A grid of MT stations was collected over southern Alberta, and both 2-D and 3-D inversions of the MT data have been completed.

The potential field data (gravity and aeromagnetic) in southern Alberta comprise two main anomalies associated with the Precambrian basement rocks: the Vulcan Structure and the Snowbird Tectonic Zone.

The Vulcan Structure is an east-west trending anomaly which truncates a northwest – southeast tending potential field fabric to its south. This feature has been the subject of a number of crustal-scale studies in the past. It was originally interpreted as a Precambrian rift zone (Kanasewich, 1968), and was more recently explained as a suture zone between distinct crustal blocks (Gorman et al., 2002; Hoffman, 1988). Since the Vulcan Structure does not outcrop, interpretations have been based on sparse core samples which have penetrated the very top of the basement rock, the potential field data, and crustal scale seismic studies (refraction, reflection, and teleseismic). The newly available MT data from this study has the advantage of being sensitive to different rock properties than the seismic data and can offer new constraints to help define the nature of this anomaly.

The second major potential field anomaly in southern Alberta is the Snowbird Tectonic Zone (STZ). This zone outcrops in the Athabasca basin, where it is defined by a mylonitic zone of rocks whose tectonic significance is debated. The exposed portion of the STZ has been suggested to be an entirely intra-continental feature (Hanmer et al., 1994, 1995), whereas the Rimbey granites suggest that the STZ in Alberta may be best explained as a Paleoproterozoic subduction zone (Ross et al., 2000). Again, the MT data collected as part of this study may add new constraints to the nature of the STZ hidden below the WCSB.

This thesis outlines the current knowledge of the Precambrian basement beneath southern Alberta. It describes the currently available magnetotelluric data, presents the 2-D and 3-D modelling of that data, and uses these models to constrain the structure and evolution of the Precambrian Alberta basement.

<h1 style="text-align: center">Chapter 2</h1>
<h1 style="text-align: center">Background</h1>

The study area is located in southern Alberta, near the western edge of the North American craton, also known as Laurentia (Figure 2.1). This area is underlain by the 2-3 km thick Phanerozoic Western Canada Sedimentary Basin (WCSB), which overlies the crystalline Precambrian rocks.

Because the Precambrian basement rocks cannot be mapped from outcrops, geophysical data and core samples are required to study them. Large quantities of geophysical data have been collected in Alberta over the last 60 years for hydrocarbon exploration, but these studies have largely focussed on structures within the WCSB.

Studies of the crystalline Precambrian basement rocks were greatly advanced by the Lithoprobe Alberta Basement Transect (ABT), described by Ross (2000). This project involved seismic studies (reflection, refraction and teleseismic), potential field modelling, and magnetotellurics to delineate structures within the crust and mantle of the lithosphere beneath Alberta.

The ancient Precambrian rocks which make up the lithosphere below Alberta have recorded events from early in the Earth's evolution, and the stability of the core of North America throughout history has preserved large parts of this record over geologic time.

Evidence from some of the oldest rocks found suggests that some continental crust existed as early as the Hadean (>4.0 Ga; Wilde et al., 2001). The style of plate tectonics at that time is poorly understood (e.g. Bedard, 2006), although there is evidence that some kind of plate tectonics similar to Phanerozoic style plate tectonics with convergent and divergent margins was active at least as far back as 3.0 Ga (Furnes et al., 2009; Nair & Chacko, 2008).

There is evidence that much of Laurentia was formed during suturing events in the Paleoproterozoic, with the most obvious suture along the Trans Hudson Orogen (Hoffman, 1988). The obduction of ophiolites within the Trans Hudson Orogen has shown that some form of modern plate tectonics must have occurred during the formation of Laurentia (Corrigan et al., 2007), after which it has remained a coherent block for a very long period of time. The reason for its stabilization is unclear, and through further

studies of Laurentia and its assembly, we may gain a deeper understanding of the stabilization of cratons and the nature of Precambrian plate tectonics.

This chapter gives a general overview of Laurentia's Paleoproterozoic assembly and a focussed discussion dealing with the part of Laurentia which underlies southern Alberta.

2.1   Regional Tectonic Framework

The North American craton (Laurentia) was assembled between 1.8 and 2.0 Ga by the suturing together of seven Archean blocks, bound together by Paleoproterozoic boundary zones. These boundary zones represent either collisional sutures with evidence for the consumption of oceanic lithosphere, or tectonic scale fault zones between the blocks.
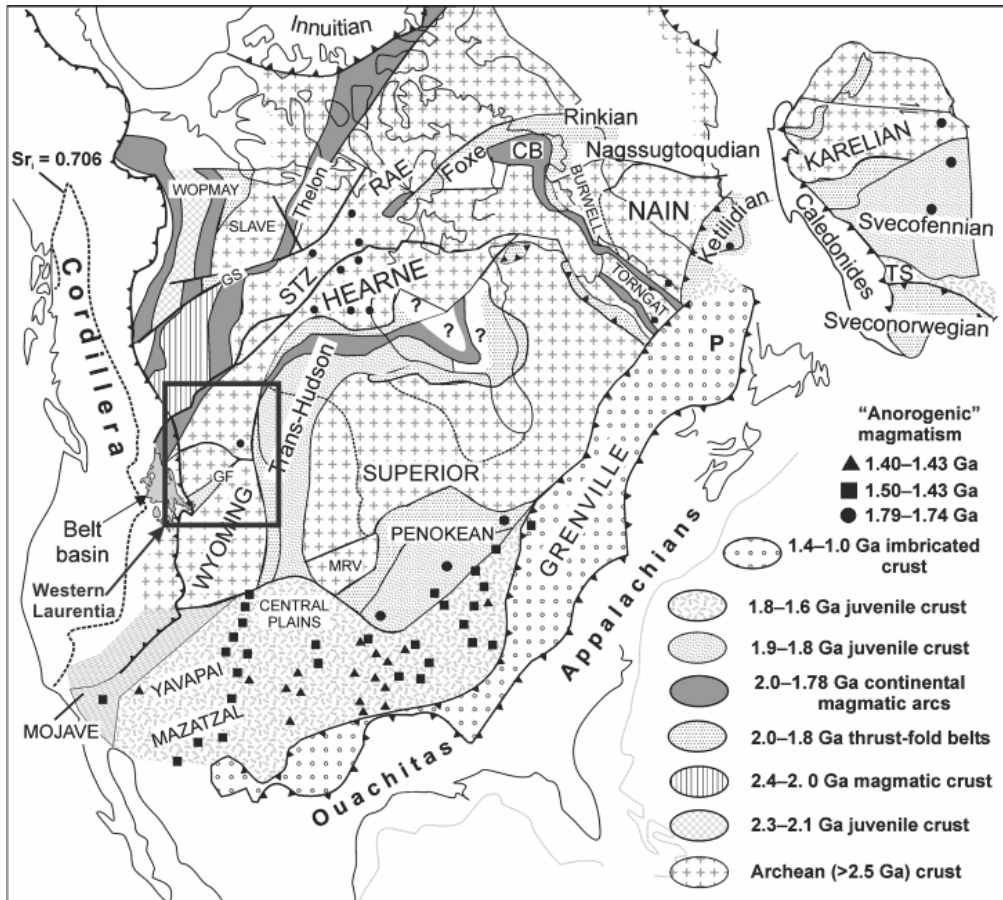
Figure 2.1: From Figure 1 of Ross & Villeneuve (2003). Precambrian Tectonic map of North America. [**Sr$_i$**] – initial strontium line represents the western boundary of Laurentia (see section 2.2), GS – Great Slave Lake Shear Zone, STZ – Snowbird Tectonic Zone, GF – Great Falls Tectonic Zone. The black box highlights western Laurentia, defined in the text.

Current studies suggest that many of the Archean blocks were sutured together at the same time, meaning subduction of oceanic crust was occurring beneath a number of these blocks during the period 2.0-1.8 Ga (Hoffman, 1989a).

2.1.1   Assembly of Laurentia

Compared to other continental cratons, Laurentia has been a coherent block for a very long time (since ca. 1.7 Ga). Other continental cratons such as the South American (0.7 Ga), African (0.7 Ga) and Eurasian cratons (0.3 Ga) were assembled long after Laurentia was an independent and coherent block (Hoffman, 1989b).

As explained by Hoffman (1989a), the majority of the assembly and deformation of Laurentia happened in four stages:

1) 2.0 – 1.8 Ga, the assembly of Laurentia;
2) 1.8 – 1.6 Ga, both subduction and anorogenic magmatism;
3) 1.6 – 1.3 Ga, large scale anorogenic magmatism; and
4) 1.3 – 1.0 Ga, orogenic events.

1) The first stage between 2.0 and 1.8 Ga saw the amalgamation of 7 microcontinents, which now survive as the Wyoming, Superior, Hearne, Rae, Slave, Nain and Burwell Archean cratons (Figure 2.1). Large areas of juvenile crust were also accreted onto the western, southern, and south-eastern edges of the protocraton during this stage (Hoffman, 1989a).

The Paleoproterozoic zones which weld the Archean terranes together show a remarkable similarity in timing and correlate well with other orogenic belts found worldwide. This gives considerable evidence for a Paleoproterozoic supercontinent (Hoffman, 1989b; Zhao, 2004) and means that it is possible that the amalgamation of Laurentia between 2.0 – 1.8 Ga was only one part of the amalgamation of a much larger supercontinent given the name Columbia. This conjecture is intriguing, yet quite unconstrained due to the lack of Precambrian seafloor record, few available apparent polar wander paths, and the deformation and overprinting of plate margins (Karlstrom et al., 2001).

The major Paleoproterozoic orogenic zone in Laurentia is known as the Trans Hudson Orogen (THO), and divides the Archean Superior Province from the

Churchill Province (Figure 2.1). This zone highlights the complexity of the Paleoproterozoic zones in Laurentia, showing a history of intraplate magmatism, rifting, formation of oceanic crust, intraoceanic and continental margin terrane accretion, subduction, and ending in terminal collision with a small Archean craton trapped between (Corrigan et al., 2007).

2) The second major time period in the assembly of Laurentia was between 1.8 and 1.6 Ga. This was a transitional time with continued tectonic accretion, and initiation of anorogenic magmatism within Laurentia. This anorogenic magmatism occurred as far as 2000 km from the nearest plate margin (Hoffman, 1988).

3) The widespread outbreak of anorogenic magmatism over Laurentia at 1.6 Ga signals the start of the third stage of Laurentia's development, and the end of tectonic accretion, lasting until 1.3 Ga (Hoffman, 1988).

Based on ideas of Anderson (1983), Hoffman (1988) suggested that this anorogenic magmatism in Laurentia could be explained by mantle upwelling and melting which in turn led to melting and underplating of the continental crust. Rifting followed from this upwelling, and led to the breakup of a supercontinent (presumably Columbia in this case), and a mechanism for the periodicity of the supercontinent cycle (Hoffman, 1989a). The original cause of the anorogenic magmatism is not understood, some attributing it to deep mantle plumes, while others have modeled cracks in the lithosphere caused by insulating, heating, and consequential bulging of the lithosphere (see Sears et al., 2005; and references within).

The persistence of anorogenic magmatism to 1.1 Ga in Laurentia suggests that Laurentia was positioned above the mantle upwelling after the breakup of Columbia, analogous to present day Africa (Hoffman, 1989a).

4) The fourth and final stage of Laurentia's assembly was characterized by orogenic activity along the Grenville orogen (Figure 2.1), as well as a thrust belt bordering the Beaufort Sea in Northwest Laurentia (Hoffman, 1989a). The Grenville orogen was a continental collision between the main core of Laurentia and other Archean cratons which made up the supercontinent of Rodinia (including Amazonia and Paragua, now located within Africa; Tohver et al., 2006).

This stage ended by 1.0 Ga marked by the end of orogenic activity along the Grenville Orogen, and is generally considered to mark the final amalgamation of Rodinia. Unlike its predecessor Columbia, the paleogeography of the supercontinent of Rodinia is well defined between about 1.0 and 0.5 Ga. The eventual breakup of Rodinia is coincident with the Cambrian period, defined by an explosion of life on Earth and has aided theories such as the Snowball Earth (Kirschivink, 1992).

Following the breakup of Rodinia around 0.5 Ga, Laurentia has remained relatively unchanged other than losing Greenland and northwest Scotland in the late Cretaceous as the modern Atlantic Ocean was formed (Hoffman, 1989b). The margins on the other hand have undergone significant deformation. Rodinia was rifted apart, Pangea was formed as another supercontinent, and it too was torn apart into the geography we see today.

2.2   Geological Structure and history of western Laurentia

Given the craton wide history summarized above, attention is now given to details of western Laurentia. Western Laurentia is defined here as the area south of the Great Slave Lake Shear Zone (GSLZ) in Alberta, north of and including the Wyoming craton, east to the Trans-Hudson Orogen (THO), and as far west as the western margin of Laurentia (see Figure 2.1). The study area for this thesis is located within western Laurentia, and focus is given to what is both known and unknown about the study area.

The western margin of Laurentia in particular underwent a complex history of accretion and deformation to form the present day crust. Currently, the western edge of North America is characterized by young mountain belts which make up the North American Cordillera and the edge of Laurentia is hidden beneath these rocks.

Sediment deposition began in the Late Proterozoic, associated with rifting of Rodinia. This rifting left a passive margin along western Laurentia where sediments were deposited up until the Late Jurassic (Price, 1994).

Between the Late Jurassic and Early Eocene, subduction began along the western margin of Laurentia, causing the deposition of sediments in a foreland basin. The subduction of oceanic crust closed ocean basins and accreted Cordilleran terranes along the edge of Laurentia (Price, 1994).

Following terrane accretion, the Laramide Orogeny occurred from the Late Cretaceous to the early - middle Eocene. The Laramide Orogeny is associated with the topography change that formed the Rocky Mountain belt, Laramide block uplifts in the USA, and the Sierra Madre Oriental belt in Mexico. In Canada and Mexico, this event is attributed to normal subduction, while magmatism in the United States occurred more than 600 km from the plate margin and is often explained as the result of flat slab subduction (English et al., 2003).

The current western edge of Laurentia is generally considered to extend as far as the initial strontium line indicated in Figure 2.1 (defined by $^{87}Sr/^{86}Sr = 0.706$ [Sr_i], with a higher ratio in the granitoid rocks associated with the craton (Armstrong, 1988). This line is a general boundary, and evidence exists that puts the edge of the craton west of this line (based on the existence of cratonic rocks to the west; Erdmer et al., 2001).
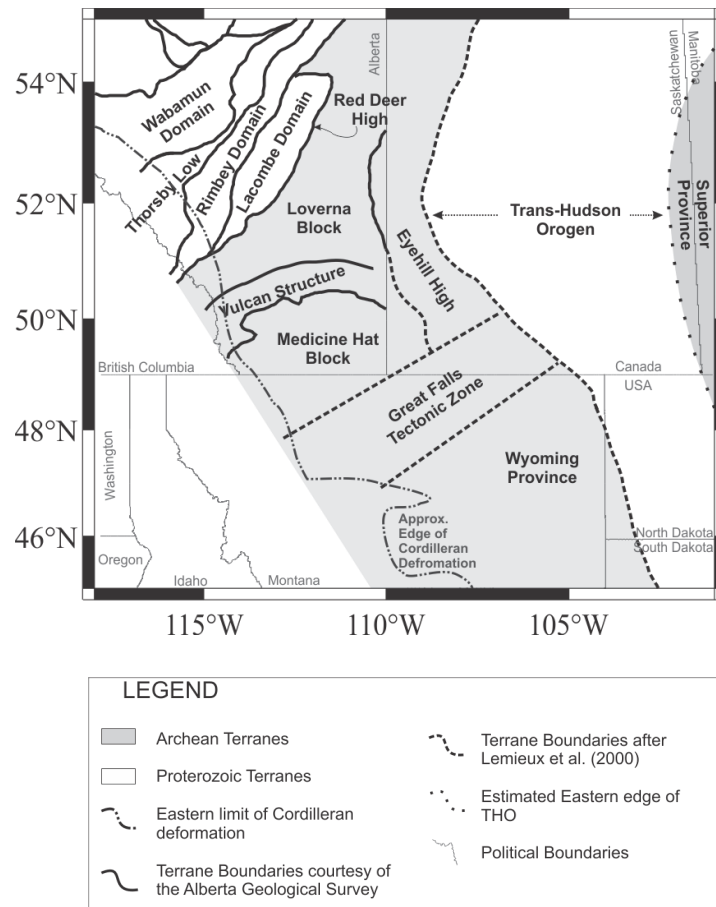
Figure 2.2: Regional map showing the Precambrian Terrane Boundaries, after Lemieux et al. (2000).

In Alberta, the Precambrian terrane boundaries seen in Figure 2.2 have been delineated beneath the WCSB using magnetic and gravity anomaly maps (Figure 2.3) in conjunction with the dating and analysis of rocks sampled by drilling beneath the WCSB (Ross et al., 1991).

The potential field anomalies associated with the Precambrian terranes become indistinguishable below the stronger potential field responses of the Cordilleran terranes to the west (Figure 2.3). This makes it impossible to map the Precambrian terranes beneath the Canadian Cordillera, so it is unclear both how far these terranes extend to the west, and how they lie relative to one another.

The Snowbird Tectonic Zone can be traced from the exposed basement in northern Saskatchewan southwest along the Thorsby Low. This zone is approximately 3000 km long, traced from the Hudson Bay to the edge of Cordilleran deformation. The Proterozoic terranes in the northwest corner of Figure 2.2 are all associated with the Snowbird Tectonic Zone, which is located to the north of the Archean Hearne Domain.

The Hearne Domain is part of the Western Churchill Province, which also includes the Rae Domain depicted in Figure 2.1. The Hearne Domain in Alberta is divided into the Eyehill High and the Loverna Block based on an aeromagnetic high which separates them (Figure 2.3). Both terranes represent Archean blocks which have been extensively reworked during the assembly of Laurentia (Ross, 2002).

The Vulcan Structure is a boundary zone separating the Loverna Block from the Medicine Hat Block (MHB). As mentioned earlier, it was originally interpreted as an intracontinental rift zone (Kanasewich, 1968), although since then many other researchers have reinterpreted it as a tectonic boundary between distinct Archean Blocks (e.g. Hoffman, 1988; Eaton et al., 1999). Since this structure is a main feature of the study area and it will be discussed in detail later.
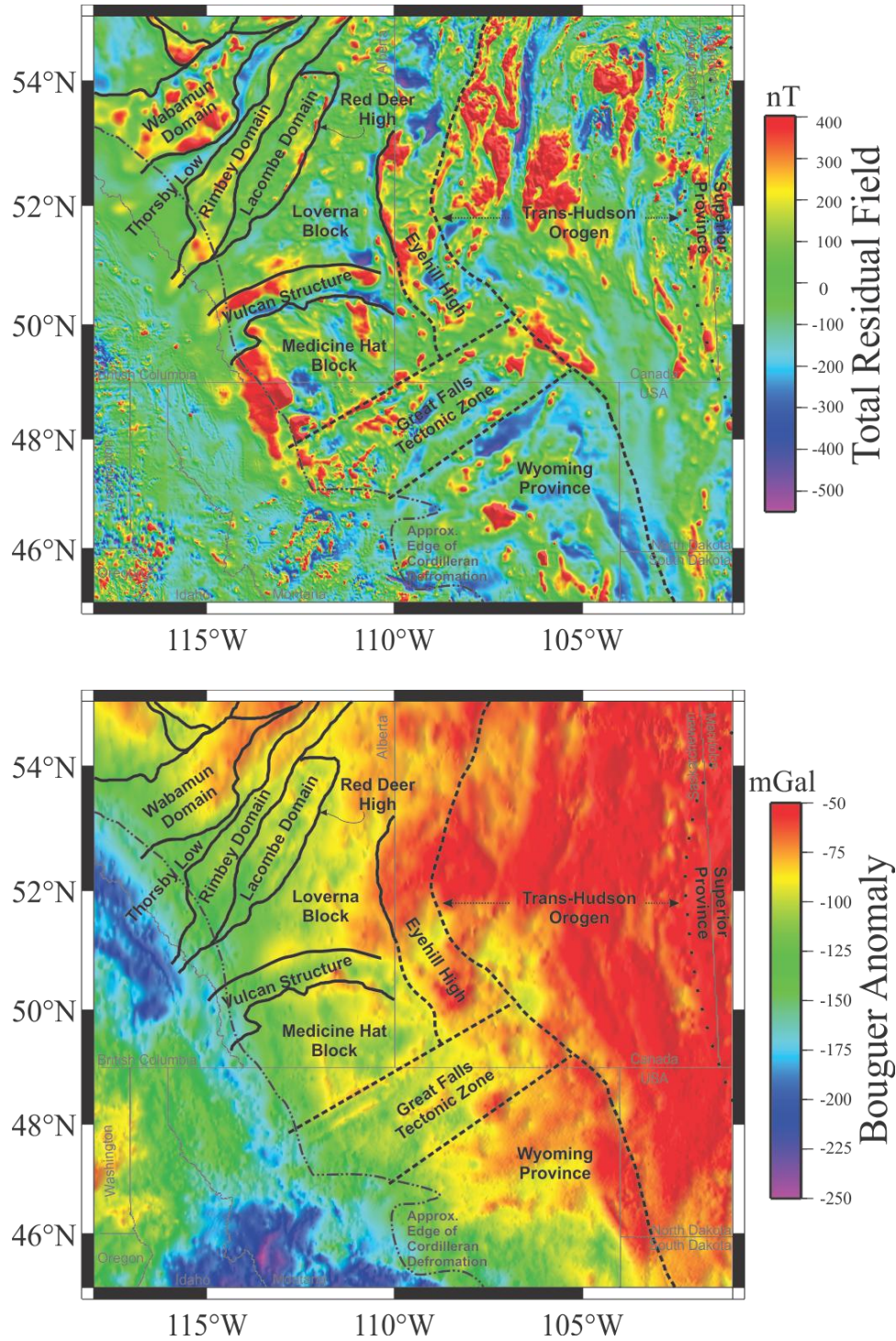
Figure 2.3: Potential field maps of western Laurentia, same legend as Figure 2.2. TOP: Total residual magnetic field anomaly map; the thin Red Deer High is a very thin and linear magnetic high along the edge of the Lacombe domain, the Vulcan structure is a relatively narrow magnetic high – low, the GFTZ is characterized by linearly trending magnetic highs, and the boundary of the Eyehill High is defined by a sharp magnetic high. BOTTOM: Bouguer gravity anomaly map; The Vulcan structure shows a broad gravity low along its length, the lineaments in the GFTZ from the magnetic map also show as gravity highs, and the MHB shows linear structures in both the magnetic and gravity field (one north – south trend is spatially coincident in both the gravity and magnetic maps). Gravity data is from Phillips et al., (1993) and Natural Resources Canada (2010); Magnetic data is from Bankey et al. (2002).

The MHB is an Archean block which is fully buried beneath the WCSB, with minettes exposed in southern Alberta which contain xenoliths originating from the crust and mantle of the MHB (Buhlmann et al., 2000; Davis et al., 1995). The overall age constraints on this block are sparse, although geochronological evidence has been used to identify it as either part of the Hearne Domain (Hoffman, 1989b) or part of the Wyoming Province (Buhlmann et al., 2000).

Based on geological mapping in the Canadian Cordillera, Deiss (1941) recognized a basement domain he named 'Montania', which is remarkably coincident with the MHB (Gorman et al., 2002). The sedimentary records studied by Deiss span more than 1.5 Ga, indicating that Montania was a basement topographic high with respect to the surrounding crust. The bounding structures to the north and south (Vulcan Structure and GFTZ) also show a long record of reactivation (Clowes et al., 1997). This indicates that the MHB experienced a very different geological history than either the Wyoming Province or Loverna Block (although they may or may not share a similar origin).

The Great Falls Tectonic Zone (GFTZ) is a linear potential field anomaly which separates the Wyoming Province from the MHB and is equally as enigmatic as the Vulcan Structure. Inherently related to interpretations about the uniqueness of the MHB, interpretations of this structure range from intra-continental in origin (Boerner et al., 1998) to an Archean suture zone between distinct blocks (Hoffman, 1989b), although it has most recently been interpreted as a Paleoproterozoic suture (Mueller et al., 2002).

The Wyoming Province is an Archean block which can be studied in greater detail than other Archean blocks beneath sedimentary basins owing to numerous locations of exposed basement in Laramide-aged uplifts (Gorman et al., 2002).

To the east in Figure 2.2 lies the Trans Hudson Orogen (THO), which separates the Hearne Domain from the Superior Province. The THO is the most evident Precambrian orogenic zone within Laurentia (Figure 2.1) and was caused by the consumption of oceanic lithosphere followed by the collision of the Superior Province with the Hearne Domain ca. 1.8 Ga.

Crustal thickness estimates obtained from much of the Lithoprobe ABT seismic reflection data show both smoothly varying crustal thicknesses (between 44 and 47 km), and one

sharp 'step' of the Moho within the MHB. The thickest crust found in the ABT data is coincident with the Vulcan Structure in southern Alberta (Bouzidi et al., 2002).

2.2.1 Paleoproterozoic Events in western Laurentia

Many changes occurred throughout Laurentia during the Paleoproterozoic era, and many of these events appear to be linked to subduction events occurring simultaneously at both the STZ and the THO (ca. 2.0 - 1.8 Ga; Ross, 2002).

Xenoliths collected from the MHB by Davis et al. (1995) indicate that the lower crust of the MHB was either underplated or reheated during the Paleoproterozoic (ca.1.8 Ga). This corresponds to a Paleoproterozoic thermal overprinting of the lower and upper crust along the margins of the Wyoming Province (Lemieux et al., 2000) and mantle metasomatism in the Wyoming Province (Davis et al., 1995).

A link between the events within the Wyoming Province and the lower crust thermal overprinting/reworking in the MHB is suggested by a high velocity zone detected in a crustal scale seismic refraction survey (Gorman et al. 2002; Figure 2.4). This high velocity zone appears to coincide with the estimated depths of the lower crust xenoliths (indicated as white diamonds in Figure 2.4), suggesting that the same event which caused mantle metasomatism and crustal overprinting in the Wyoming Province occurred beneath the MHB.

The GFTZ also shows indications of activity in the Paleoproterozoic, with magmatic outcrops in the Little Belt Mountains of Montana which indicate Paleoproterozoic U-Pb ages (ca. 1.9 Ga). These outcrops indicate that they likely came from a depleted mantle source, not an older crustal source, and suggest that oceanic crust was consumed along part of the GFTZ (Mueller et al., 2002). It has been suggested by Gorman et al. (2002) that this subduction was north – dipping based on north dipping reflectors located in the upper mantle of their seismic refraction model (Figure 2.4).

Other authors have disputed the presence of an intracontinental suture (implied by the consumption of oceanic crust) at the GFTZ (e.g. Boerner et al., 1998; Buhlmann et al. 2000), but either way it appears the GFTZ was active in the Paleoproterozoic era.

Further studies of the xenoliths that represent portions of the have shown that a Paleoproterozoic mantle enrichment event occurred beneath the MHB, coincident with similar mantle enrichment below the Wyoming Province (Buhlmann et al., 2000).

2.2.2   The Vulcan Structure

The Vulcan structure is defined by coincident east – west trending aeromagnetic and gravity anomalies greater than 350 km in length and a width around 40-70 km (Eaton et al., 1999). It defines the boundary between the Medicine Hat Block and the Loverna Block (Figure 2.2). To the west, this anomaly fades below the edge of Cordilleran deformation. To the east, this anomaly merges with potential field fabrics associated with the Eyehill High.

It appears that the Vulcan Structure underwent various periods of reactivation. Palinspastic reconstructions of the Belt Basin (see Figure 2.1) place a major fault (> 7 km of throw) west of, and in line with, the Vulcan structure (Price & Sears, 2000). Price & Sears (2000) associate the movements along this fault with reactivation of the Vulcan structure below the Belt Basin repeatedly in the Mesoproterozoic, Neoproterozoic, early Paleozoic, and Mesozoic times.

Originally the Vulcan Structure was attributed to an intracontinental Precambrian rift zone within an Archean block (Kanasewich, 1968), but the magnetic high in the north of the structure was later interpreted as a magmatic terrane, suggesting a north dipping subduction zone between distinct Archean blocks (e.g. Ross et al.; 1991). But further work by Eaton et al. (1999) and Hope & Eaton (2002) showed that a simpler explanation of the magnetic structure is a low density body within the crust (10-15 km deep) containing a significant amount of remnant magnetization oriented anti-parallel to today's magnetic field. This means that the magnetic high to the north of the Vulcan Structure does not necessarily imply subduction on its own.

Evidence for subduction at this structure comes from reflection and refraction seismic data collected as part of the Lithoprobe project and the Deep Probe project (Gorman et al., 2002). The reflection seismic data shows evidence for south dipping features within the lower crust (Eaton et al., 1999), and crustal thickening that is spatially coincident with the Vulcan Structure (Bouzidi et al., 2002). Refraction seismic data showed two north dipping reflectors within the upper mantle, which were interpreted as northward
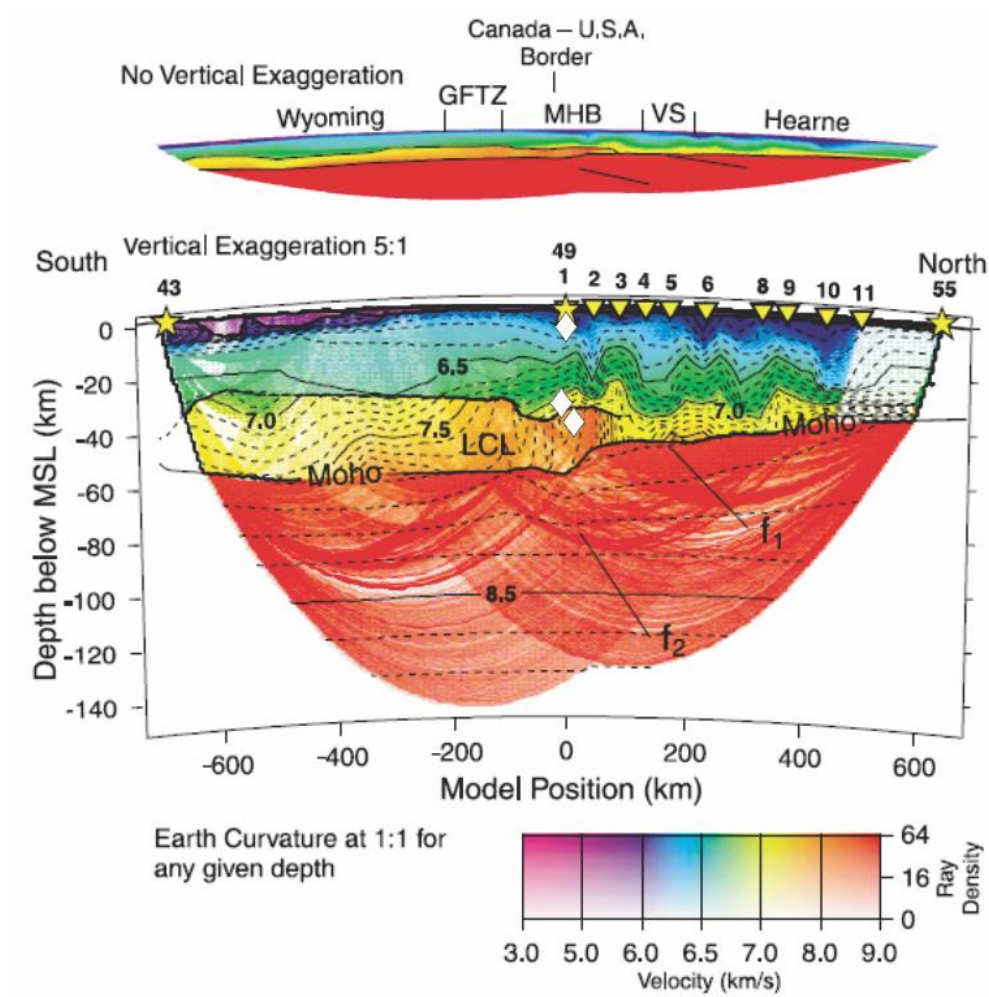
Figure 2.4: Seismic refraction model from Fig 10 of Gorman et al. (2002). GFTZ – Great Falls Tectonic Zone; LCL – lower crustal layer; VS – Vulcan Structure. Yellow stars and triangles represent shot points, sloping lines marked f1 and f2 represent north dipping reflectors recognized in the refraction data, and white diamonds represent approximate depths of xenoliths obtained by Davis et al. (1995). The upper crust xenoliths were dated ca. 2.6 Ga (Archean), while the lower crustal xenoliths are dated as ca. 1.78 Ga (Paleoproterozoic) and spatially coincide with the lower crust layer showing fast seismic velocities. MSL - meters above sea level.

subduction at both the Vulcan Structure and the GFTZ (Gorman et al., 2002). Therefore, the lower crust dips south and the upper mantle structure dips north, making it difficult to determine subduction polarity based on the seismic data alone.

The truncation of potential field anomalies by the Vulcan Structure also suggest that the Vulcan Structure represents a major tectonic boundary between distinct blocks. North – northwest trending potential field anomalies which exist within the MHB are truncated by the Vulcan Structure (Lemieux et al., 2000).

The subduction hypothesis for the Vulcan Structure appears to have the most evidence, but the potential field signature does not appear to delineate a subduction zone. Typically a magnetic high associated with a magmatic arc terrane occurs down-dip from the surface trace of the subduction zone. The potential field modelling discussed above indicates that the magnetic high is due to a single low density body with a high magnetic susceptibility buried 10 - 15 km in depth, which is not an expected subduction related magmatic arc. Therefore the seismic evidence points to subduction at the Vulcan Structure whose polarity is unclear, and the potential field data suggests that the Vulcan Structure is a tectonic boundary between distinct blocks but lacking features which are typically associated with subduction. Regardless, it is most likely that the Loverna Block and the MHB on either side of the Vulcan Structure are distinct blocks, colliding together at some point along the Vulcan Structure.

The high velocity lower crust layer modelled by Gorman et al. (2002) beneath the MHB and the Wyoming Province is bounded to the north by the Vulcan Structure. As discussed earlier, this lower crustal layer is spatially coincident with xenoliths which indicate overprinting/reworking contemporaneous with terminal collision at the THO. Because it ends at the Vulcan Structure, it means that the lower crust on either side of the Vulcan Structure is structurally different, reiterating that the Archean blocks on either side of the Vulcan Structure represent distinct blocks. The fact that the 1.8 Ga overprinting/reworking occurs only on one side of the structure led (Gorman et al., 2002) to suggest that terminal collision along the Vulcan Structure occurred either while subduction was ongoing at the THO, or possible even earlier.

There is only one geochronological date obtained for the Vulcan Structure, indicating a thermal and/or metamorphic event ca. 2.1 Ga (Lemieux et al., 2000). The crosscutting of the Vulcan Structure by the Eyehill High suggests that the Vulcan Structure is older than terminal collision within the THO (ca. 1.8 Ga; Eaton et al., 1999). It is unclear if the 2.1 Ga date obtained from drill core at the top of the basement is associated with the Vulcan Structure, or if it is from en event which occurred in either the Loverna Block or the MHB previous to terminal collision along the Vulcan Structure. The high velocity lower crust, and the crosscutting by the Eyehill High provides a better way to date, because both of these features have a clear relationship to the Vulcan Structure. Both of these pieces of evidence suggest that the Vulcan Structure was active before terminal collision of the Superior Province with the Hearne Domain ca. 1.8 Ga, which in turn suggests that the 2.1

Ga thermal / metamorphic events could be related to the formation of the Vulcan Structure, although this timing is tentative and better age constraints are needed.

2.2.3   The Snowbird Tectonic Zone and the Hearne Domain

Within Alberta, the Hearne Domain is thought to represent the hinterland for coeval subduction within both the THO and the STZ, trapping the Hearne Domain in a sort of tectonic vice (Ross et al., 2000). Where it is exposed in northern Canada it is not clear that the STZ represents a subduction zone, although the Hearne Domain appears to have undergone compressional deformation coeval with terminal collision at the THO (Maclachlan et al., 2005).

The Hearne Domain more or less follows the Trans Hudson Orogen (THO) along its entire length. The Hearne Domain occurs to the south of the Snowbird Tectonic Zone (STZ), which separates the Hearne Domain from the Archean Rae Domain. Beneath Alberta, the STZ also separates the Hearne Domain from younger terranes thought to be associated with accretionary processes (Figure 2.1).

In Alberta, the Hearne Domain is divided into the Archean Eyehill High and Loverna Block, and both are affected by high-grade metamorphic overprinting dated at 1.79 – 1.81 Ga (Ross et al., 1995), although this is not a diagnostic feature of the Hearne Province elsewhere. The Eyehill High shows Archean ages of 2.6 – 2.7 Ga (Ross et al., 1991) and a single zircon age of 1.78 Ga, which implies either reworking or crystallization contemporaneous with terminal collision of the THO (Eaton et al., 1999).

The magnetic anomaly associated with the western edge of the Eyehill high has been modelled as a near vertical, linear dike in the upper crust by Hope & Eaton (2002). Combined gravity and magnetic modelling found that this near vertical dike bounds the eastern edge of a large block of dense material in the lower crust (coincident with lower crustal anomaly below the MHB described in the previous section). They attribute this dyke to a change from the deformed hinterland of the THO to the east (within the Eyehill High), to a dense block associated with the MHB.

P- wave traveltime tomography from a profile of teleseismic stations found that the Loverna Block is characterized by high velocities within the upper 200 km of the mantle (Shragge et al., 2002). This is complemented by low resistivities within the upper mantle of the Loverna Block found in the Lithoprobe MT data (Boerner et al., 1999; see Chapter

3). This means that the upper mantle of the Loverna block is characterized by high velocities and low resistivities.

Within Alberta, the STZ is associated with the Lacombe Domain supracrustal rocks, Rimbey High magmatic terrane, Thorsby Low, and the Red Deer Conductor, all of which parallel the trace of the STZ. The Wabamun Domain is a piece of juvenile Proterozoic crust which shows a different geometry than the other terranes and whose tectonic significance is unknown.

The Rimbey High is associated with granites showing ages between 1.78 and 1.85 Ga, coincident with the timing of Laurentia's amalgamation (Eaton & Cassidy, 1996). Teleseismic receiver function analysis shows evidence for low S wave velocities between 13 and 16 km under the Rimbey High (Eaton & Cassidy, 1996).

The Thorsby Low is a gravity and magnetic anomaly generally considered to be the trace of the STZ into Alberta (Boerner et al., 1995), and is associated with a step of 10 km in Moho topography (Hope & Eaton, 2002).

The exposed portion of the STZ shows a wide band of mylonitic rocks, and seismic profiles in Alberta show a zone of east dipping crustal reflectivity interpreted as crustal scale imbrication with a northwest vergence (Ross, 2002). This imbrication is evident in both the Lacombe and Rimbey Domains which can be traced into the lower crust (Ross, 2002).

2.3   Lithosphere – Asthenosphere Boundary

The Laurentian craton that we see today has escaped recycling by plate tectonics over a long period of geological time due to the thick, buoyant, viscous, and high brittle yield stress of the lithospheric mantle underlying the crust (Bedard, 2006). This lithospheric mantle remains buoyant above the asthenosphere, and movement of the lithosphere over the asthenosphere is accommodated at the lithosphere – asthenosphere boundary (LAB).

The LAB has proven a difficult target for geophysical exploration. Many studies define its location as the base of a high velocity mantle lid, and some define it based on a distinct change in seismic anisotropy (Eaton et al., 2009). Additionally, the LAB has been seen in magnetotelluric (MT) studies as a low in resistivity consistent with seismic low

velocity zones, most easily explained by the presence of water or partial melt at the LAB boundary (Eaton et al., 2009).

Eaton et al. (2009) have also shown through mechanical modelling of common lithospheric minerals that the LAB probably moves through dislocation creep. In places where fluids are present at the boundary, the LAB would be a wide zone of dislocation creep whereas a lack of fluid will cause a much sharper boundary.

Magnetotelluric data (see the next chapter) collected in northern Alberta has shown that the 'electrical LAB' occurs at depths on the order of 200 km below the WCSB (Turkoglu et al., 2009). Knowledge of this boundary is important to our understanding of plate tectonics and mantle convection, as well as surficial structures such as diamondiferous kimberlites (Jones & Craven, 2004).

Diamondiferous kimberlites are thought to exist mainly in very old, thick lithosphere. Previous MT studies by Jones & Craven (2004) and Jones et al. (2009) have indicated the usefulness of MT studies in further narrowing the search for diamondiferous kimberlites within the old and thick lithosphere.

The diamond stability field is the depth range within the lithosphere where carbon is stable in diamond form. Within the Slave craton this is expected to be seen at depths around 160 km (Jones & Craven, 2004). Above 160 km, the carbon is present as graphite, a mineral which can be detected using MT owing to its very low electrical resistivity.

An upper mantle conductor interpreted as graphite was detected below the Slave craton, spatially coincident with diamondiferous kimberlites. This conductor was interpreted as graphite and indicated the presence of carbon within the lithosphere (Jones & Craven, 2004).

Other MT studies in southern Africa have shown that previous assumptions that diamonds occur at the center of old cratons may not be universal. Instead, large gradients of electrical parameters such as resistivity associated with the LAB may better describe the locations of diamondiferous kimberlites (Jones et al., 2009). The lithosphere is the thickest in the center of a craton, and thins towards the edges. Therefore based on their South African example, Jones et al. (2009) suggest diamondiferous kimberlite magmas may occur along the boundaries of cratons, not the thickest portion as previously believed. This means that diamondiferous kimberlites may occur along the edges of old,

thick cratons, whose lithosphere is thick enough to remain within the diamond stability field.

MT studies can be used to detect areas where diamondiferous kimberlites may occur in two ways: detecting the presence of carbon in the lithosphere and finding large gradients in the electrical LAB (Jones & Craven, 2004; Jones et al., 2009).

2.4   Unanswered Questions

Limited geophysical and geological data from the Precambrian basement in southern Alberta means that many important tectonic features are poorly understood. The evidence for widespread Paleoproterozoic tectonic events throughout southern Alberta is relatively extensive, but the precise relationship between those events and the Vulcan Structure remains unknown. A better understanding of how some of the Paleoproterozoic features (like the STZ and the Eyehill High) relate to the Vulcan Structure is important to our understanding of what the Vulcan Structure represents.

There is significant evidence that the Hearne Domain has been caught in a tectonic vice between the STZ and the THO (Ross et al., 2000), but little data exists indicating how the LAB and upper mantle have been affected by these events.

The topography of the LAB within Alberta is quite variable, but it is difficult to precisely determine the depths. In Alberta it is expected to be around 200 – 250 km deep, but no study to date has explicitly defined it in southern Alberta.

Magnetotelluric (MT) exploration is a useful way to study the structure of the lithosphere It provides an electrical resistivity model which can be used to answer the tectonic questions listed above. The next chapter summarizes what previous MT studies have revealed about the structure and history of the crust and upper mantle beneath Alberta.

Chapter 3

Previous magnetotelluric studies in Alberta

There has been a long history of magnetotelluric (MT) investigations in Alberta. This began with the pioneering studies of Niblett & Sayn-Wittgenstein (1960) in the 1960s that validated the idea of the MT method that had been proposed by Cagniard (1953). This led to the large scale Lithoprobe Alberta Basement project throughout the 1990's which collected more than 300 long period MT stations (Boerner et al., 2000) and showed that 2-D models of subsurface resistivity could be derived from MT data and used to study the style of tectonic evolution.

In addition to these MT studies, a number of magnetovariational (MV) studies took place in Alberta using grids of three component magnetometers. These surveys identified the locations of a number of conductors within the lithosphere of western Canada (Gough, 1992). MV data have good lateral resolution, but the lack of electric field data results in poorer vertical resolution than with MT data.

This chapter will give an overview of previous MT data collection in Alberta and summarize what these studies have revealed about the electrical resistivity structure of the Albertan lithosphere. Appendix A contains an explanation of how MT works, as well as a detailed explanation of the terminology used here.

3.1 Summary of the MT method

MT instruments measures the orthogonal components of naturally occurring electric and
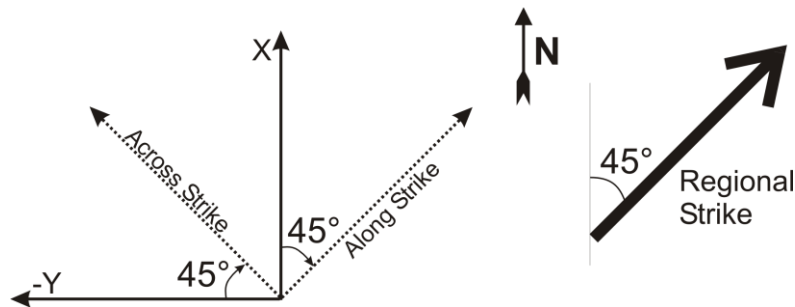
Figure 3.1: The electric and magnetic fields are measured in the x and y coordinate frame, and for the 2-D case they are rotated into the regional strike coordinate frame. The *yx* data becomes the TM mode after rotation (E_y is rotated across strike), and the *xy* data becomes the TE mode (H_y is rotated across strike).

magnetic fields. It can be shown that E_x-H_y and E_y-H_x are correlated, where E is the electric field, H is the magnetic field and the subscript denotes the direction of the field component, with the x direction conventionally chosen to point north (x is chosen to point north throughout this thesis, unless specified otherwise). Apparent resistivity and phase measurements can be computed for the *xy* and *yx* data.

In a region where electrical resistivity only changes with depth, the resistivity structure is 1-D, and apparent resistivity and phase computed from E_x-H_y and E_y-H_x will be the same. This will not be the case for a 2-D or 3-D region.

If the Earth has a 2-D resistivity structure, there will be a direction in which the electrical resistivity does not change. This is known as the geo-electrical strike direction. The angle between the strike direction and geographic north is known as the strike angle. MT measurements are routinely made with respect to geographic north and are rotated to a co-ordinate frame that is parallel to the regional geo-electrical strike direction (Figure 3.1). It can be shown that in this co-ordinate system, the EM fields can be described by

Figure 3.2: Maps of the MT stations collected throughout Alberta, (a) data collected in the 1960's, (b) shows the data collected in the 1970's and 1980's. The large dots indicate the approximate location of historical MT data in Alberta (where they are split, data was either collected for more than one study, or the same data was used for both studies). (a): the white dot is from Niblett & Sayn-Wittgenstein (1960); red dots are from Vozoff et al. (1963); blue dots are from Srivastava et al. (1963); orange dots are from Vozoff & Ellis (1966); and the yellow dot is from Rankin & Reddy (1969). The red lines indicate the direction of minimum apparent resistivity, and the blue lines indicate the direction of maximum apparent resistivity (from Srivastava et al., 1963). (b): the purple and blue dots are all from Reddy & Rankin (1971), the blue dots indicate the first measurements of the Red Deer Conductor (see further text); the purple line shows the location of the profile over the Vulcan Structure by Peeples & Rankin (1973).

two independent modes. One mode has the electric field polarized parallel to the strike direction (TE – Transverse Electric), and the other mode has the magnetic field polarized parallel to the strike direction (TM – Transverse Magnetic). Figure 3.1 shows an example where the strike direction is N45°E. MT measurements were made in geographic coordinate system and were then rotated into the regional strike direction (45° counter-clockwise). In this case the rotated *xy* data corresponds to the TE mode, and the rotated *yx* data is the TM mode. Data for these two modes can be collected simultaneously with an MT survey and are jointly interpreted with modern inversion algorithms.

In a 3-D region the electrical resistivity varies in all three directions, the TE and TM modes do not exist separately. This means that modes cannot be defined separately.

In the 1960's, MT data was analysed in terms of 1-D modelling because 2-D and 3-D modelling software had not been developed. In the older literature, differences between the *xy* and *yx* data was called anisotropy. This referred to a directional dependence of the MT data (i.e. a 2-D or 3-D effect) and was not necessarily an intrinsic anisotropy in the subsurface resistivity structure.

3.2   Historical magnetotelluric data collection in Alberta

The first MT study in Alberta recorded magnetic data from an observatory in Meanook, and measured the electric field over long dipoles nearby (Niblett & Sayn-Wittgenstein, 1960). This study was one of the first field tests of the MT method that had been proposed by Cagniard (1953).

3.2.1   Data from the 1960's

Analysis by Niblett & Sayn-Wittgenstein (1960) and Srivastava et al. (1963) showed that the *xy* and *yx* data recorded at Meanook were significantly different. The xy data required a large conductor at depths of 80-90 km in the 1-D resistivity model, derived from NS electric fields (x-direction) and EW magnetic fields (y-direction). The *yx* data was derived from the perpendicular field components and did not require this same conductor.
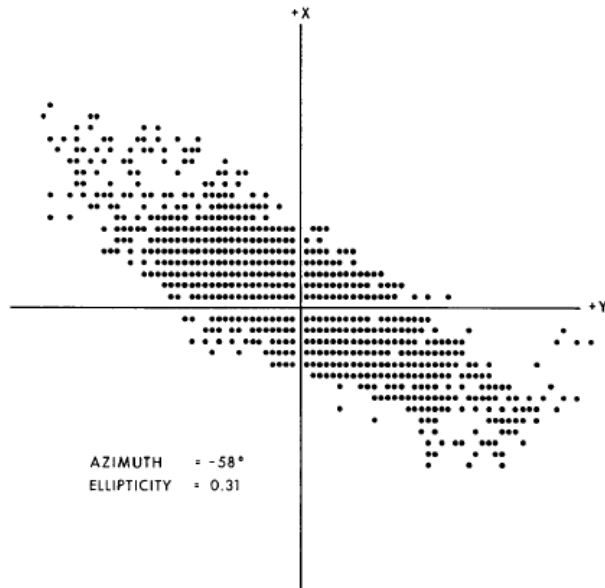
Figure 3.3: From Rankin & Reddy (1969); a depiction of the polarization of the electric field at a station near Kavanagh (Figure 3.2). Each dot represents a vector measured at a specific point in time, and the elliptical spread of the dots represent how polarized the measured electric field is (ellipticity), and at what direction it is polarized (azimuth).

Srivastava et al. (1963) collected MT data along a north-south profile stretching across all of southern and central Alberta as shown in Figure 3.2a. From south to north their profile included stations in Cardston, Champion, Beiseker, Clive, Cooking Lake, and Meanook (Figure 3.2a). These locations were chosen in order to test the validity of Cagniard's (1953) plane wave assumption over large distances with relatively little topography change. They were able to model the depth to the Precambrian basement with 1-D resistivity models, which showed that the resistivity of the sedimentary basin was quite low (between 5 and 10 Ω-m), and the Precambrian basement is quite resistive (over 1000 Ω-m).

Srivastava et al. (1963) also analysed the departures of the MT data from the 1-D case (when *xy* does not equal *yx*) by calculating the polarization angles of the electric field. The polarization of the electric field is caused by the fact that currents preferentially flow in the direction of minimum apparent resistivity, which cancels the electric field in that direction. The more elliptical the polarization ellipse, the larger the difference between minimum and maximum apparent resistivity. Figure 3.3 shows an example from a different study located near Kavanagh Alberta, which also used the polarization angles of the electric field (Rankin & Reddy, 1969). The electric field in Figure 3.3 is clearly polarized, and the minimum apparent resistivity direction lies ~N45°E.
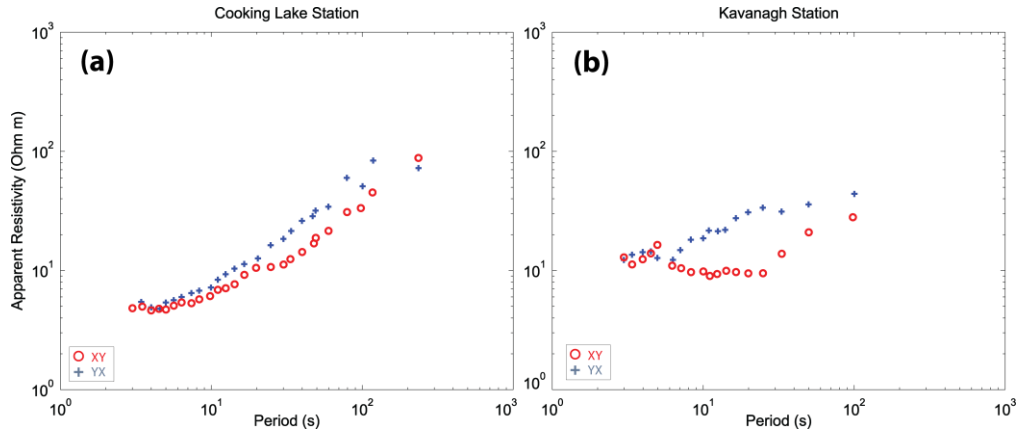
Figure 3.4: Apparent resistivity sounding curves measured by Vozoff et al. (1963) near Edmonton, displayed in the measurement coordinate system. The Cooking Lake station (a) shows little difference between the *xy* and *yx* modes, while the Kavanagh station (b) shows a large split between the modes. This was originally referred to as anisotropy, but is likely caused by 2-D or 3-D structure. The phase was not calculated for these soundings, likely because the data was too noisy. (Note that the original soundings had the xy and yx data opposite to what is shown here, i.e. the xy displayed here is the yx displayed in the original study).

Srivastava et al. (1963) showed that north of and near Edmonton the angle was approximately N45°W, which became N30°W at Beiseker, N15°W at Champion, and back to N40°W at their Cardston station (left side of Figure 3.2). These angles can be thought of as a rough strike angle determination, and they highlight the 90° ambiguity in any strike angle determination. For example, based on Figure 3.3 alone, there is no way to know if the strike is N45°W or N45°E (i.e. whether it follows the direction of maximum or minimum apparent resistivity, or neither in the case of galvanic distortion – see appendix A).

Vozoff et al. (1963) recorded MT data at 4 sites near Edmonton (Cooking Lake, Kavanagh, Onoway, and Bon Accord) with the purpose of field testing the theory of Cagniard (1953). The short period response from these stations (less than ~4 seconds) indicated the expected 1-D nature of the sedimentary basin at all 4 stations, and periods greater than ~4 seconds correspond to the Precambrian basement, showing large differences between each of the four stations. Figure 3.4 shows apparent resistivity soundings from two of the stations collected by Vozoff et al. (1963).

The two stations depicted in Figure 3.4 are separated by about 40 km, and they show that the Precambrian basement is quite different over this short distance. The Cooking Lake station in Figure 3.4(a) shows a small difference between the *xy* and *yx* modes, whereas the Kavanagh station in Figure 3.4(b) shows a much larger split between them. This was attributed by Vozoff et al. (1963) to anisotropy in a layer near the top of the basement rocks and was modelled in two of their stations as a layer which required different resistivity values for the *xy* and *yx* data. For the Kavanagh station in Figure 3.4(b), it was not possible to model the data using an anisotropic layer, showing that the difference between *xy* and *yx* data may be related to 2-D or 3-D structure as opposed to anisotropy.

As MT instrumentation improved with time, a wider period band could be measured. At first, 60 Hz power was needed at each site to power the induction coils, but later batteries could be used, and a significant source of noise from power lines was no longer an issue. The ability to automatically digitize data (as opposed to manually) also removed a source of error, and computing power which allowed for the easy computation of the coherency between the electric and magnetic field improved the choice of data used for processing.

The complexity of the Precambrian basement continued to be a focus of MT studies in central Alberta. Figure 3.5 shows an apparent resistivity sounding collected near Leduc (next to Kavanagh in Figure 3.2) by Rankin & Reddy (1969). This sounding shows that the split between the *xy* and *yx* data is still present at periods up to 1000 seconds, indicating that the source of the geo-electric complexity is obvious in all the data

Figure 3.5: MT sounding from Leduc collected by Rankin & Reddy (1969), displayed in the measurement coordinate system. The split between the modes always begins at a period near the top of the Precambrian basement.

Figure 3.6: From Vozoff & Ellis (1966), displayed in the measured coordinate system (x is north). This sounding was been collected near Brooks (Figure 3.2), the theoretical model is based on the *yx* data, since the electric field in the x direction (north) had a low signal level (corresponding to a low coherency in the *xy* mode). The $H_x - E_y$ points are the *yx* mode, and the $H_y - E_x$ points are the *xy* mode. The PC label on the theoretical model represents the location of the Precambrian basement rocks.

sensitive to the basement.

Data collected at three MT stations in southern Alberta by Vozoff & Ellis (1966) found that the strong E-W polarization of the electric field caused the N-S electric field to be quite weak. This caused the signal to noise ratio in the *xy* data to be quite small (corresponding to a small electric field in the north-south direction). Their stations were located in Brooks, Beiseker, and Vulcan (left side of Figure 3.2), and the apparent resistivity soundings from each station are shown in Figure 3.6 to Figure 3.8.
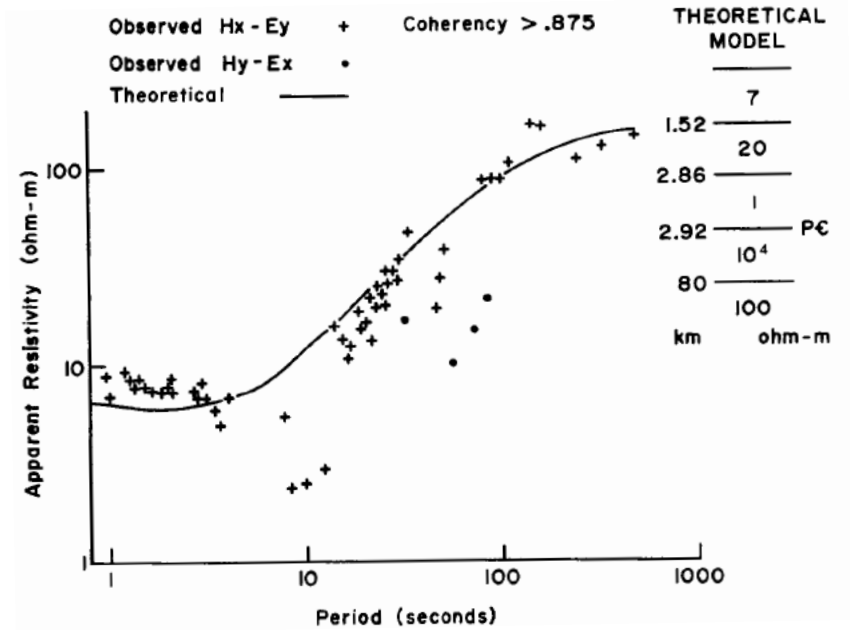
Figure 3.7: From Vozoff & Ellis (1966), sounding collected at Beiseker again showing very few points from *xy* mode due to low signal in E_x (where x points north). The PC label on the theoretical model represents the location of the Precambrian basement rocks.
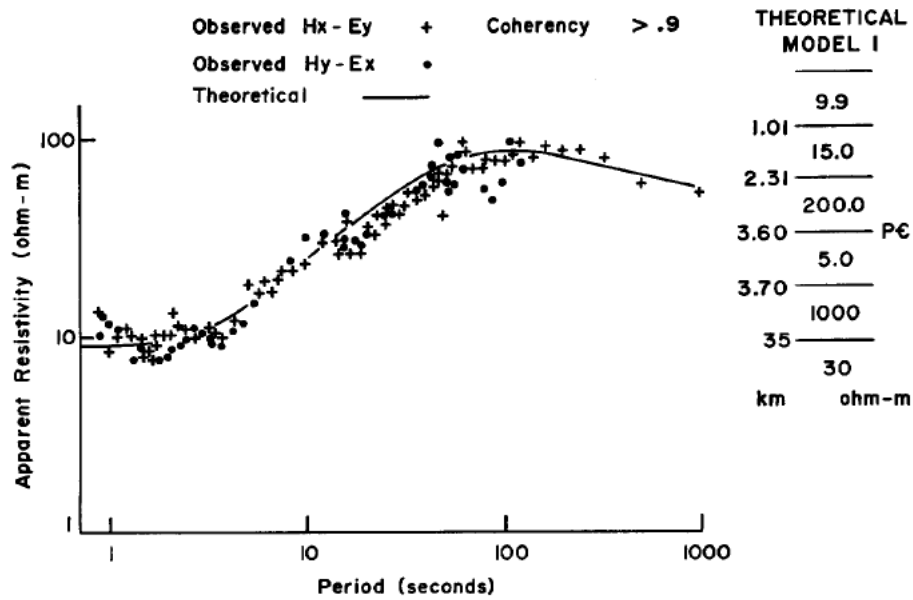
Figure 3.8: From Vozoff & Ellis (1966), MT sounding collected from near the town of Vulcan (in the measurement coordinate system – x points north). The PC label on the theoretical model represents the location of the Precambrian basement rocks.

Vozoff & Ellis (1966) generated 1-D resistivity models from the *yx* data (E_y-H_x), with constraints on the structure of the sedimentary basin from nearby well logs. The models for the Brooks and Beiseker stations showed a two order of magnitude drop in resistivity

27

at ~90km depth (see the theoretical models in Figure 3.6 and Figure 3.7), similar to the yx models collected in Meanook by Srivastava et al. (1963). The Vulcan station showed a similar discontinuity but at a depth of 35 km instead (Figure 3.8). Since 1-D models likely do not describe the data very well, we cannot be sure of the depth of these discontinuities, but it remains clear that the Vulcan station sensed something different than the Brooks or Beiseker stations. This is confirmed in the polarization angles which are N15°W near Vulcan and closer to N40°W in other places throughout Alberta (see the red and blue lines in the left of Figure 3.2).

3.2.2   2-D modelling (post 1960's)

Reddy & Rankin (1971) collected 16 MT sites in central Alberta, indicated by the purple and blue stations in Figure 3.2(b), and showed that much of the data in Central Alberta could be explained by 2-D resistivity models.

They determined a regional strike angle by rotating each station in 5° increments, and their strike angle was chosen as the angle that gave a maximum apparent resistivity. Note
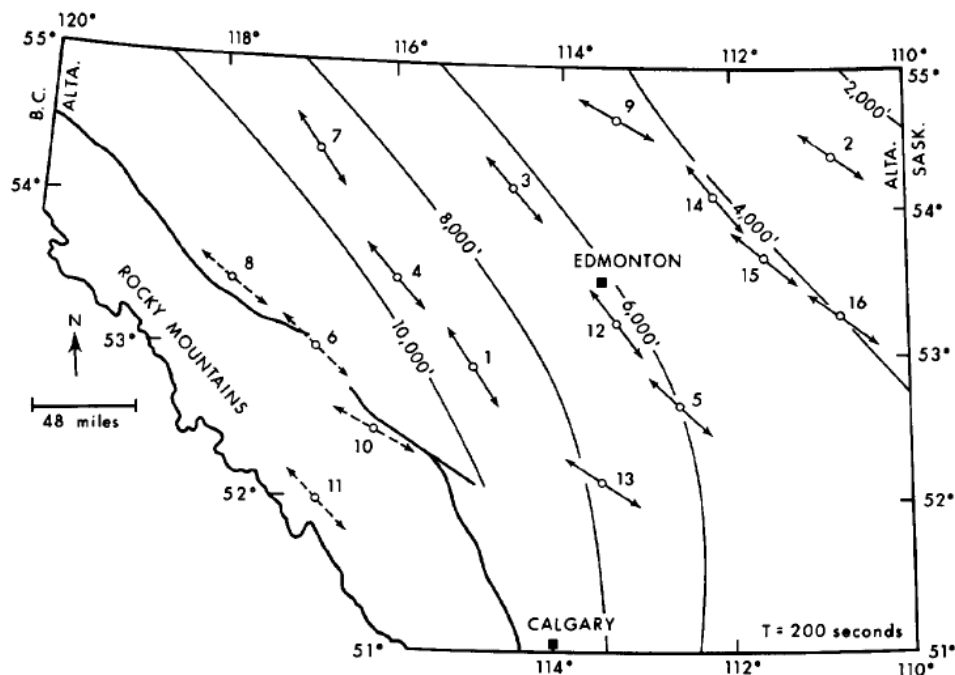
Figure 3.9: From Reddy & Rankin (1971); solid vector lines represent the maximum apparent resistivity angle at a period of 200 seconds, and the dotted vector lines represent the angle of electric field polarization at stations where apparent resistivity curves were impossible to determine. The contour lines represent the depth of the sedimentary basin.

that the angle of maximum apparent resistivity does not always correspond to the regional strike direction, since the strike angle can also correspond to the minimum apparent resistivity. This 90° ambiguity in strike angle determination is an important concept.

At periods less than 30 seconds the angles of maximum apparent resistivity were found to be erratic, consistent with a 1-D resistivity structure in the western Canada sedimentary basin. At longer periods the strike angles are consistently ~ N45°W, as shown by Figure 3.9 which shows the direction of maximum apparent resistivity at a period of 200
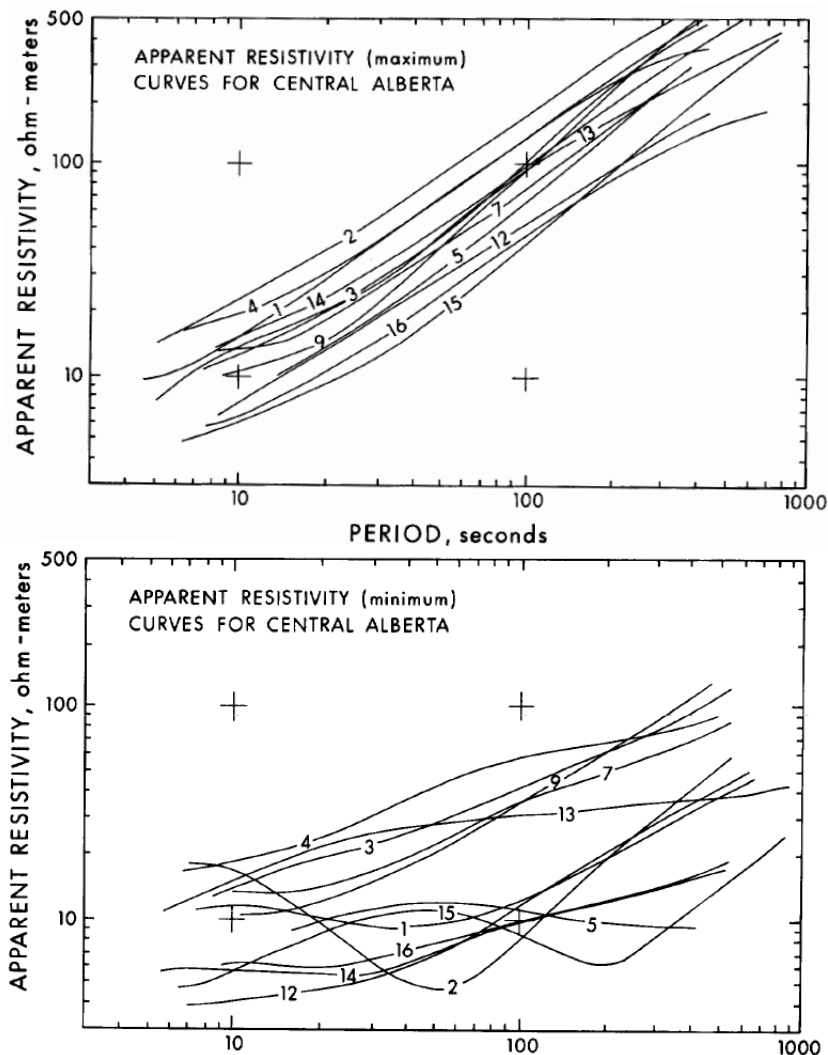
Figure 3.10: From Reddy & Rankin (1971); Apparent resistivity curves from 16 stations located in central Alberta (see Figure 3.2 or Figure 3.9 for locations). These show the apparent resistivity curves obtained from rotating each station to their maximum apparent axis. The top is the apparent resistivity in the direction of maximum apparent resistivity, while the bottom shows the apparent resistivity in the minimum direction.

seconds.

Figure 3.10 shows the apparent resistivity curves resulting from rotating each station to the maximum apparent resistivity angle. The upper panel shows the maximum apparent resistivity (which are now known to be the TM mode) and the lower panel shows the minimum apparent resistivity (the TE mode). The consistent split between the *xy* and *yx* data that was noted by previous authors (Rankin & Reddy, 1969; Srivastava et al., 1963) is even more obvious after rotating into the strike direction.

The consistency of the maximum apparent resistivity angle over Central Alberta, and small Swift skew values (which indicate that the MT data is likely not 3-D) led Reddy & Rankin (1972) to study whether 2-D models could explain the apparent resistivities measured in Central Alberta. They thought the split between the maximum and minimum apparent resistivities in Figure 3.10 might be explained by the 2-D structure of a sedimentary basin. Therefore they initiated the first 2-D study of MT data in Alberta.
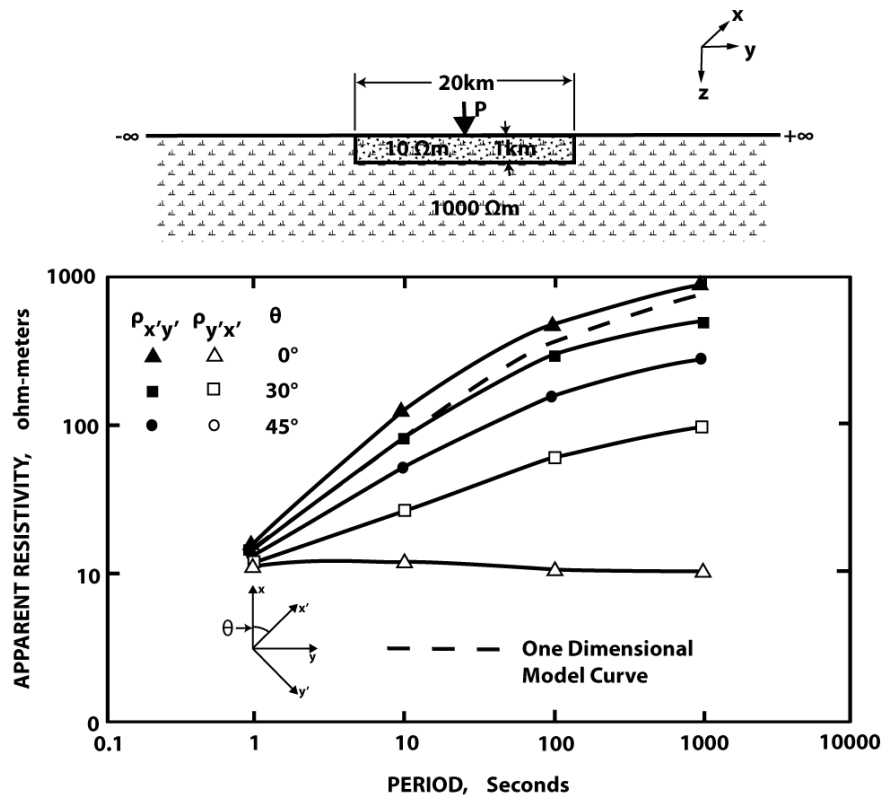
Figure 3.11: Reproduced from Reddy & Rankin (1972); The top shows a 2-D model used to generate the *xy* and *yx* curves in the bottom figure (at point 'P'). The result from 1-D modelling assuming no horizontal boundaries in the model is shown as a dotted line.
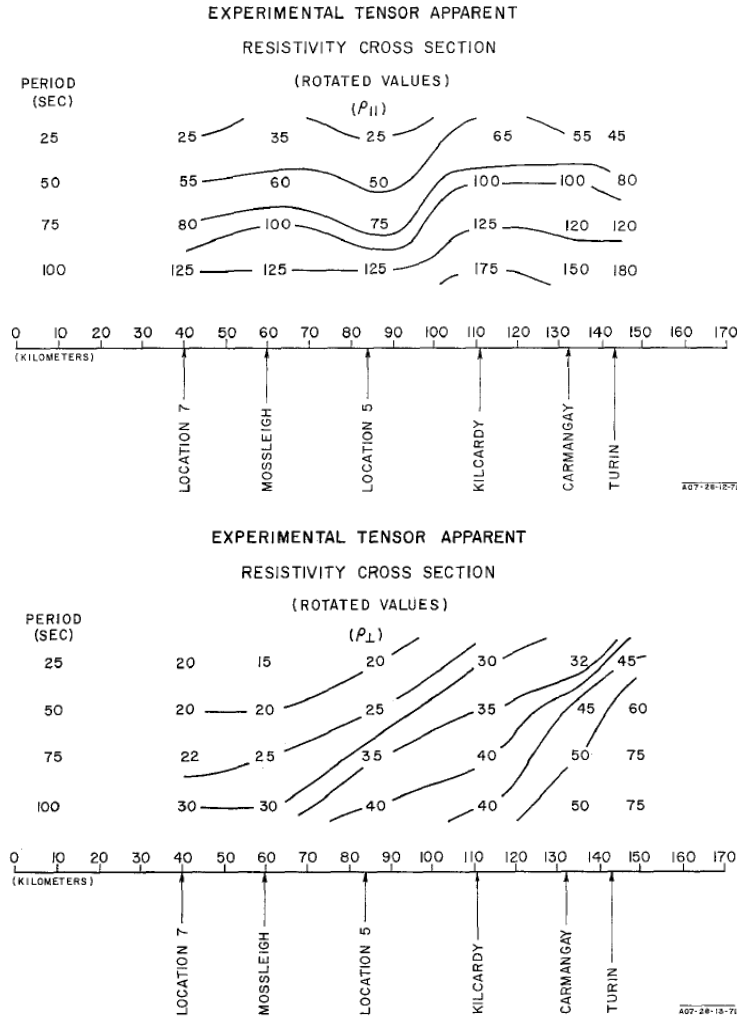
Figure 3.12: From Peeples & Rankin (1973); A profile oriented from north to south across the Vulcan Structure (see Figure 3.2). The top figure shows the TE mode pseudo section, and the bottom figure shows the TM mode pseudo- section. The Vulcan Structure occurs directly beneath Location 5, with Location 7 to the north, and Kilcardy to the south.

Figure 3.11 shows the 2-D model developed by Reddy & Rankin (1972) which can explain the difference between *xy* and *yx* data in a N45°E co-ordinate system, although they point out that this model does not represent the actual geometry of the WCSB in Alberta. The 2-D response was calculated using the method by Swift (1967), where they attempted to explain this split with a conductive sedimentary basin of limited horizontal extent. However we now know that this split is mainly due to conductors with a NE-SW strike direction.

Figure 3.11 shows the predicted maximum and minimum resistivity curves at a measurement point P in the model, set within a 20 km wide and 1 km deep sedimentary

basin in a resistive half space. At a rotation angle of 0° the xy and yx data show a large split which resembles the split between the maximum and minimum apparent resistivity curves shown in Figure 3.10. This suggests that a 2-D resistivity model is capable of explaining the MT data from Central Alberta, although the model they used is not a realistic example of the subsurface beneath Alberta.

A few of the minimum apparent resistivity curves in Figure 3.10 show very low values of apparent resistivity (stations 2, 5, and 15 with locations indicated in blue in Figure 3.2b). These data are the first data that showed the presence of a major crustal conductor in the crust beneath Alberta. Subsequent measurements have mapped this feature in detail (known as the Red Deer Conductor; Boerner et al., 2000).

Peeples & Rankin (1973) used MT to study the Vulcan Structure, which at the time was considered to be a Precambrian rift zone. They collected 6 MT soundings within the approximate period range of 10 to 1000 seconds along a north - south transect (see the purple line in Figure 3.2b).The Swift skew values for all of the data were less than 0.25, indicating that the data were likely not 3-D. The strike angle was determined using the method by Swift (1967), and was found to be N25°W. This is almost perpendicular to the geological strike of the Vulcan Structure, but is consistent when the 90° ambiguity of strike angle is considered.

The TE mode pseudo-section (at the top of Figure 3.12) shows some resistivity features which seem spatially coincident with the Vulcan Structure, but the TM mode pseudo-section (bottom of Figure 3.12) does not show any features associated with it. This result is consistent with the presence of a conductor which is oriented parallel to the strike direction. In this case, the along strike electric field (TE mode) is strongly affected by the conductor. In contrast, the electric field across the conductor (TM mode) is not significantly affected.

3.3   Magnetovariational Data

Grids of magnetovariational (MV) data were collected throughout western North America with the intention of mapping the lateral locations of conductive anomalies in the crust. MV data has the advantage of being sensitive to lateral changes in resistivity, but is relatively insensitive to resistivity changes with depth.

One main conductor discovered through the MV grids is the Southern Alberta British Columbia (SABC) conductor, which was located by Gough et al. (1982; Figure 3.13).

The SABC conductor has been modelled as both a sheet current model (Wang, 1988a), and a line current model (Wang, 1988b). Wang (1988b) found that the SABC conductor is most likely ~80 km wide, with a less well defined depth of ~55 km (MV data has very little depth sensitivity). To the west, the SABC appears to stretch at least as far as Kootenay Lake in southern BC. Gough (1986a) interpreted this as evidence that the Laurentian lower crust extends as far west as Kootenay Lake.
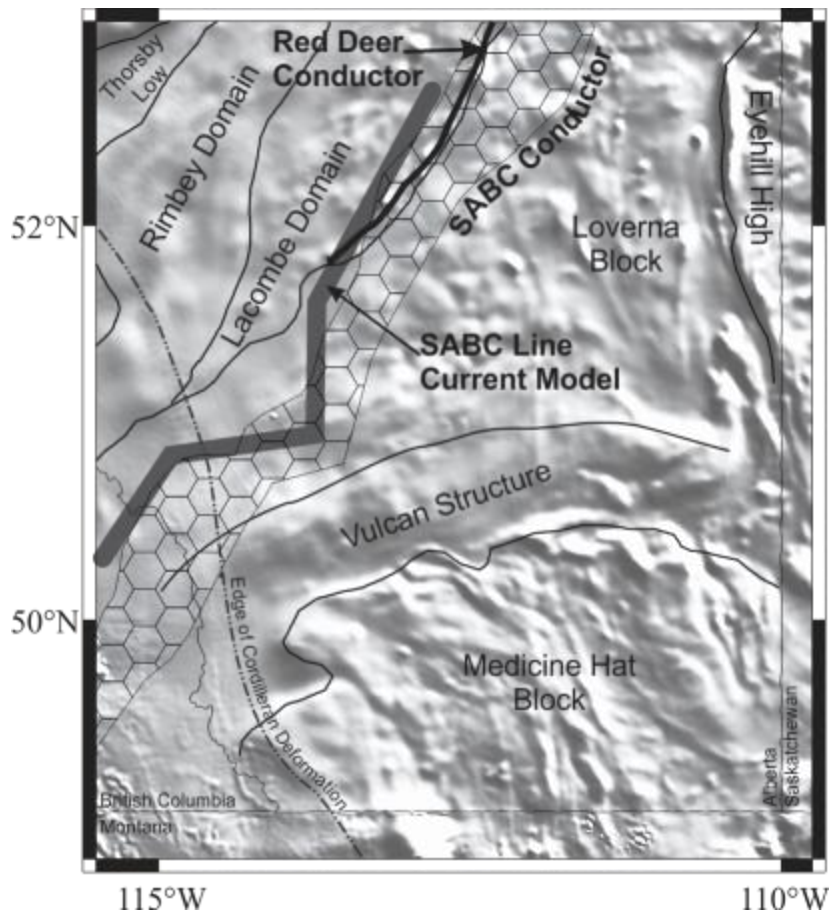
Figure 3.13: The gradient of the total residual magnetic field in the background, the southern Alberta British Columbia (SABC) conductor defined by Gough (1986a) is shown by the honeycombed area, the SABC line current model from (Wang, 1988b) is the large gray line, and the bold black line shows the Red Deer Conductor along the edge of the Lacombe Domain (Boerner et al., 2000).

3.4 Results of Lithoprobe MT studies in Alberta

By the early 1990's, 2-D inversions of MT data were becoming available and this allowed for 2-D analysis of MT profile data, such as the one which crossed the Vulcan structure. To study the structure and history of the lithosphere below the WCSB, the Lithoprobe ABT project collected 2-D profiles of long period MT data across Alberta.

The Lithoprobe ABT project collected 323 long-period MT stations with the goal of mapping crustal scale features hidden below the WCSB. This large database allowed for the inversion of MT data collected on a number of MT profiles in southern and central Alberta. The results of the survey are summarized by Boerner et al. (2000) and indicate a complicated lithosphere below Alberta.
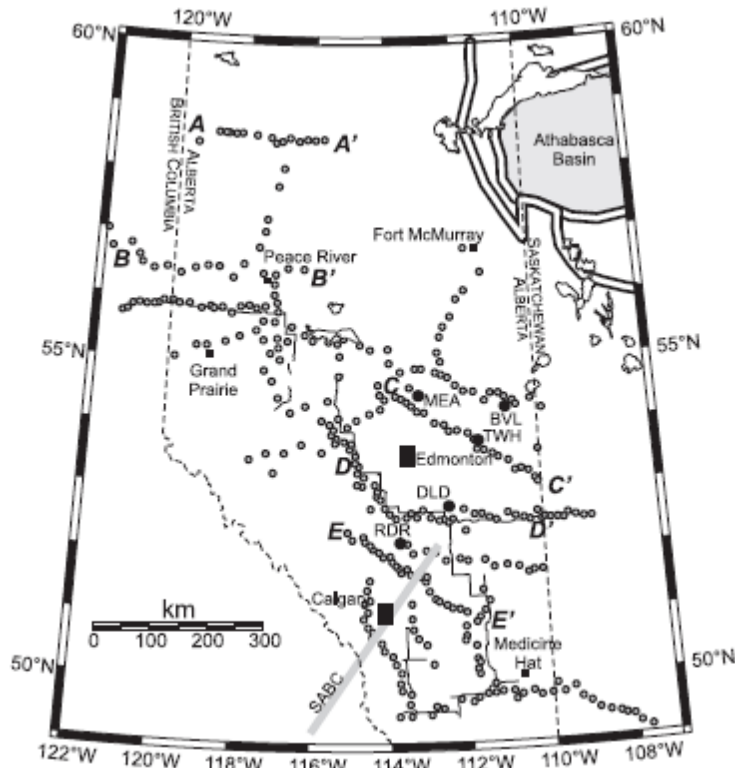
Figure 3.14: From Boerner et al. (2000). Map showing the locations of the Lithoprobe ABT data collected throughout Alberta. Several profiles are denoted, as is the general location of the Southern Alberta - British Columbia (SABC) conductor. The filled in circles indicate stations collected by Reddy & Rankin (1971) which are affected by the RDC.

3.4.1 Strike and Dimensionality

The overall geoelectric strike was determined by Boerner et al. (2000) using the tensor decomposition method of Groom & Bailey (1989). Induction vectors were used to resolve the inherent 90° ambiguity in the calculation of the geoelectric strike direction, since induction vectors will be oriented perpendicular to strike above a 2-D resistivity model. At short periods (< 4 s) that only sample the sedimentary rocks of the WCSB, the MT data shows no consistent strike direction and indicates a 1-D resistivity structure. The periods that sample the basement (>10 s) have strike directions that correspond closely to the aeromagnetic anomaly fabric (Figure 1.3), deviating little from N45°E (see section 4.4 for strike analysis of MT data in southern Alberta).

Dimensionality analysis by Jones et al. (2002) of the Lithoprobe ABT MT data was used to classify sites as 1-D, 2-D (with and without galvanic distortion), or 3-D. They used a classification based on the seven MT tensor invariants proposed by Weaver et al. (2000), and their results from southern Alberta are shown in Figure 3.15. As with previous analyses of the Lithoprobe data, the short period data (< 1000s) that samples only the WCSB and the basement shows that much of the MT data is 2-D (Figure 3.15a). This is

Figure 3.15: Redrawn from Jones et al. (2002), Geoelectric complexity of MT stations collected as part of the Lithoprobe Alberta Basement Transect, gray shaded area is the location of a strong conductor present in the TE mode data (with a strike direction of N45°E), and the location of the Red Deer Conductor (RDC) is based on the 2-D MT inversions by Boerner et al. (2000). At a relatively short period of 213.3 seconds (a), the data shows 3-D effects associated with the RDC and the Paleoproterozoic terranes to the north. The long period MT data of 1280 seconds (b) shows 3-D effects widespread throughout the Archean Loverna Block, which appear to be associated with the TE conductor indicated by the gray shading.

Figure 3.17: MT sounding which characterizes the conductor denoted by the gray area in Figure 3.15. Similar to the RDC sounding in Figure 3.20, the conductor only affects the TE mode, and the TM mode shows a very similar structure to many other places in Alberta. (The sounding has been rotated to a strike angle of N45°E).

not the case at stations close to the Red Deer Conductor (RDC) which shows galvanic distortion and local 3-D effects. Longer period MT data (> 1000s) show much more widespread 3-D effects in the MT data (Figure 3.15b). Figure 3.15(b) shows that at a period of 1280 seconds, nearly all of the data collected within the Loverna Block is
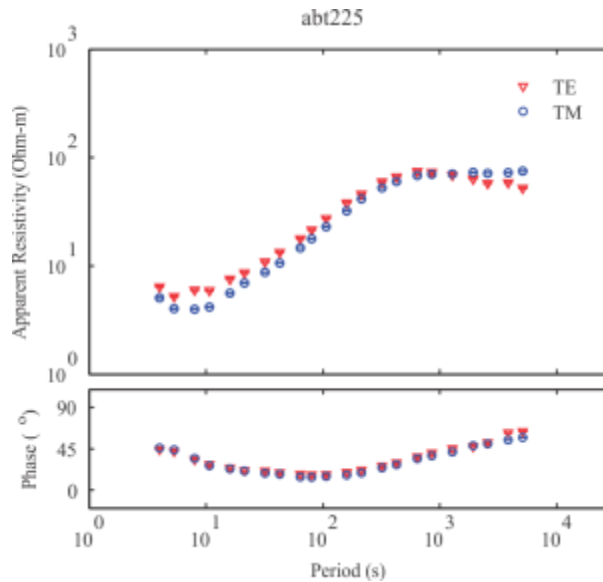
Figure 3.16: A 1-D MT sounding from southern Saskatchewan. Both TE and TM curves shows a very similar structure to the TM modes collected near the RDC and within the Loverna Block. This sounding has been rotated to N45°E.

classified as 3-D.

It is possible for 3-D effects near the surface to affect data from short periods to long periods, since the long period data samples the near surface, the deep structure, as well as a larger lateral volume than the short period data. For example, the shallow RDC in Alberta is expected to show 3-D effects in the short period data and will cause an increasingly expanding footprint laterally with increasing period. But Jones et al. (2002) point out that this is not an evenly increasing effect centered on the RDC; instead, it shows a much greater area than expected, particularly to the south and east of the RDC. This could be due to an (a) lithosphere structure that becomes more complex with depth, particularly in the Loverna Block, or (b) a fundamental problem with galvanic distortion analysis related to each mode having a different skin depth (Jones et al., 2002).
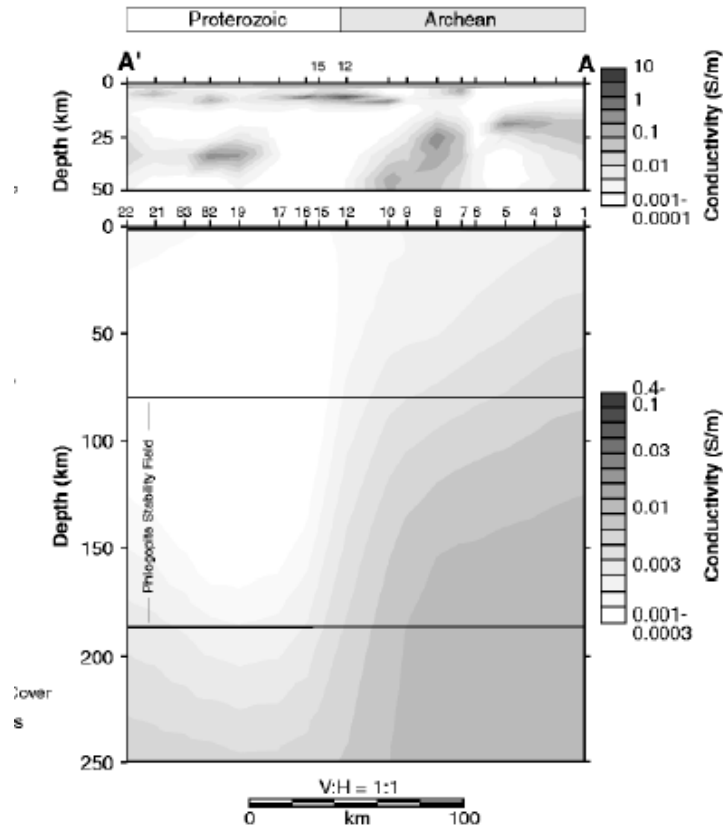
Figure 3.18: From Boerner et al. (1999). The results of a 2-D isotropic inversion of the TM mode data along profile D-D' in Figure 3.14. Note that gray represents low resistivity, and white is high resistivity. The upper mantle underlying the Archean Loverna Block is an order of magnitude less resistive than the upper mantle underlying the Proterozoic terranes to the northwest.
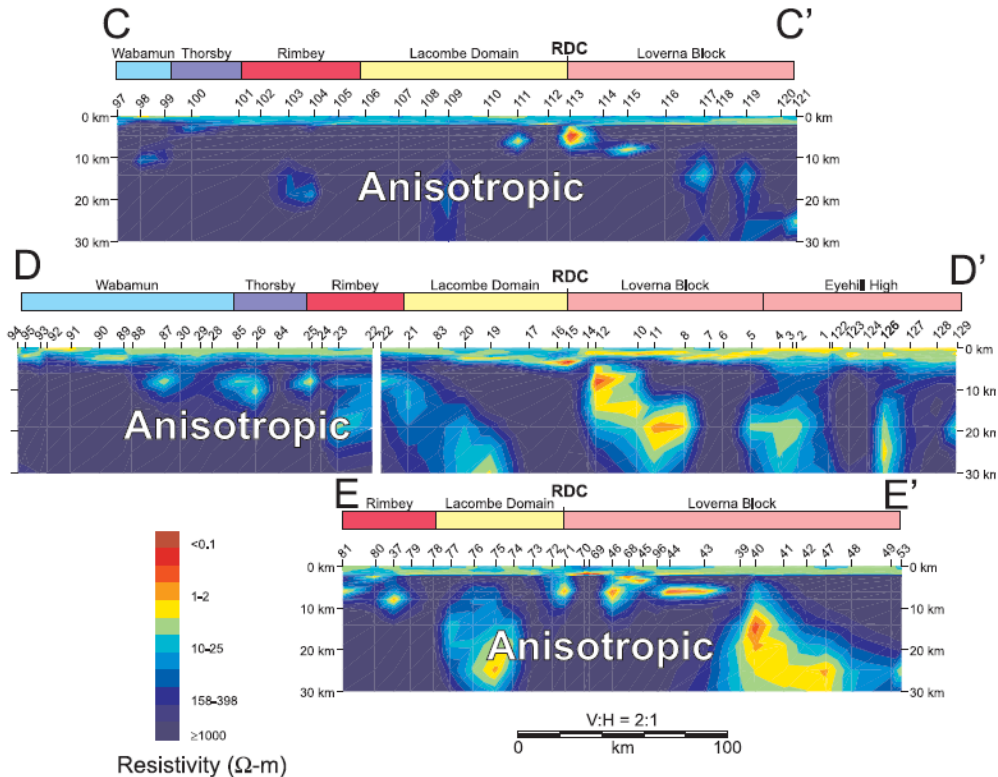
Figure 3.19: From Boerner et al. (2000); Inversion results from three profiles which cross the RDC in central Alberta (profile locations are in Figure 3.14). The profiles show unrealistic structure which does not fit either mode very well.

The gray area in Figure 3.15 denotes the general location of a conductor detected only by the TE mode, as depicted by Figure 3.17. There is a strong split between the two modes and a strong similarity in the character of the TM mode curve.

The TM mode in Figure 3.16 shows a great similarity to MT data collected in areas where the MT data is fairly 1-D. Figure 3.16 shows an MT sounding which has been shown to be approximately one dimensional, collected in southern Saskatchewan (southeast corner of Figure 3.15). This curve shows that the Precambrian lithosphere in southern Saskatchewan indicates a structure similar to what the TM mode measures in the Loverna Block.

3.4.2   2-D analysis of the Lithoprobe Alberta Basement data

Boerner et al. (1999) recognized that the TM model of much of the data in Alberta is very similar to the 1-D data from southern Saskatchewan. They disregarded the TE mode data, attributing it to distortion by linear conductors such as the RDC. The TM mode data was

interpreted as providing reliable constraints on the resistivity structure of the upper mantle, since it was shown to be accurate in other 1-D areas. On this basis, they implemented a 2-D isotropic inversion of only the TM mode data in central Alberta. Their resulting model is shown in Figure 3.18, and shows that the upper mantle under the Archean crust (the Loverna Block) is an order of magnitude less resistive than that which lies below the Paleoproterozoic crust (the Lacombe Domain and Rimbey Domain).

Other inversions which attempted to invert both the TE and TM modes had significant difficulty in fitting the data with realistic resistivity models. The large split between the TE and TM modes can cause unrealistic conductive zones within the crust in their 2-D models. For example, Figure 3.19 shows the results from 2-D inversions of TE and TM mode data over central Alberta (profile locations are in Figure 3.14).

The models show that a thin, conductive anomaly consistently occurs at the boundary between the Lacombe domain and the Loverna Block, and is attributed to the RDC. The RDC is explained in their models by a conductor which lies directly below the WCSB, but not in electrical contact with it. The 2-D models show discrete conductors which dip to the southeast, coincident with a dipping fabric seen in the Lithoprobe seismic reflection surveys (Ross et al., 1995).

The small conductive features in these models are a possible indicator of electrical anisotropy within the crust, since they represent strong but thin conductors oriented along strike. They allow the split between TE and TM mode to be fit well, but they do not necessarily represent a realistic geo-electric structure. For this reason Boerner et al. (2000) attribute the conductive zones to anisotropy within the crust in Alberta.

This is the same conclusion which was made by the early studies in Alberta which assumed that a split between the *xy* mode and the *yx* mode was due to anisotropy in their 1-D models. At that time, 2-D modelling showed that the split was not necessarily related to anisotropy, but may be caused by 2-D or 3-D structure. The presence of possible anisotropy in the 2-D profiles suggests the possibility of 3-D geo-electric structure in Alberta. With the present availability of 3-D inversion codes, and a new dataset collected for the purpose of 3-D inversions, we are now in a position to test whether 3-D models can explain the data without requiring anisotropy in the crust.

3.4.3   3-D modelling

The applicability of 3-D MT data analysis in Alberta has already been tested by Turkoglu et al. (2009), where a grid of MT data in northern Alberta was modelled using a 3-D inversion. They also used a combination of Lithoprobe MT data and new MT data collected between the Lithoprobe profiles. Their study found that the MT data was sensitive to the lithosphere asthenosphere boundary (LAB), finding that its most likely depth is around 200 km.

3.4.4   The Red Deer Conductor

At the time the Lithoprobe ABT data was collected, the presence of the SABC conductor was already known. The Red Deer Conductor was defined by the Lithoprobe MT data, named for a linear conductor appearing spatially coincident with the thin magnetic high in Figure 2.3 (Red Deer High; Boerner et al., 1995). Boerner et al. (2000) recognized the spatial coincidence of the RDC and the SABC, although the sparse MV grid used to define the SABC conductor makes it difficult to determine their exact relationship. The RDC was recognized by an obvious conductor seen in the MT data, both in the soundings (Figure 3.20), and in the large induction vector responses which was measured along a
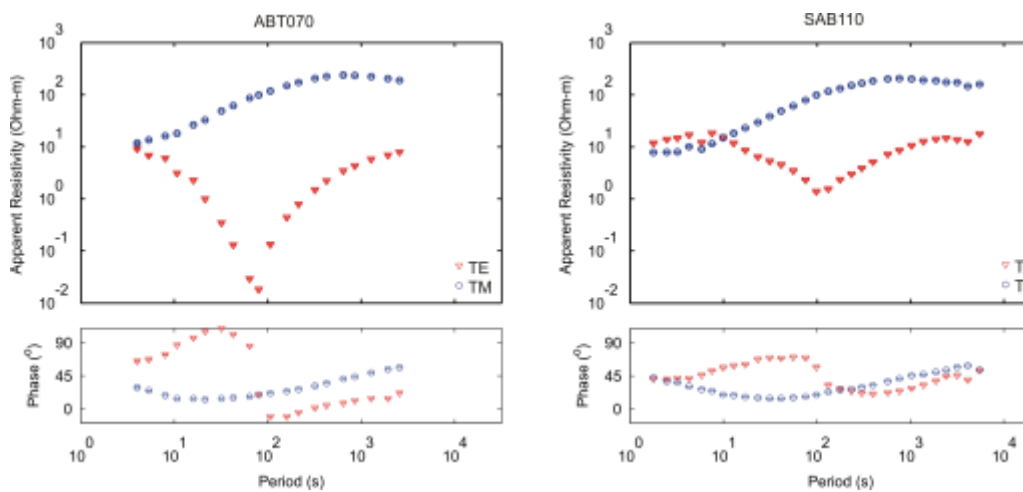
Figure 3.20: MT soundings collected near the RDC. On the left the sounding ABT070 collected as part of the Lithoprobe ABT project very close to the axis of the RDC. The right plot shows SAB110, an MT sounding collected further from the axis of the RDC than ABT070, but still indicating the effects from the RDC. Both soundings have been rotated following the strike of the RDC (coordinate system rotation of N45°E), and both show an obvious notch around 100 seconds in the TE mode.

Lithoprobe ABT profile of MT data (Boerner et al., 1995).

The apparent resistivity response that characterizes the RDC can be seen in its most extreme form in Figure 3.20. These soundings show a notch in the TE mode data around 100 seconds, indicating that this conductor must be thin (enough that it is not seen in the TM mode), and be conductive along strike such that it gives a large response in the TE mode. It is interesting to note that data collected very close to the RDC (e.g. ABT070) shows phase angles more than 90°, and less than 0°, which indicates an electrical structure which is more complicated than a 2-D isotropic model can reproduce. This could indicate the presence of electrical anisotropy related to the RDC, or a complicated 3-D effect.

The RDC lies near the boundary between the younger Paleoproterozoic crust to the east (STZ domains), and the older Archean crust (Hearne Domain) to the west (Figure 3.15). Magnetic source location estimates by Pilkington et al. (2000) put the depth of the Red Deer High just below the bottom of the WCSB, which coincides with the depth of the RDC based on MT modelling (Boerner et al., 2000). The aerial locations of both the Red Deer High and the RDC also coincide well, leading Boerner et al. (2000) to attribute the Red Deer High and the RDC to the same subsurface structure.

3.5 Resistivity within the Canadian Cordillera

An MT profile that crossed the Canadian Cordillera in British Columbia has shown that the electrical lithosphere - asthenosphere boundary below the accreted terranes is much shallower than beneath the craton in Alberta (Soyer & Unsworth, 2006). It is unclear where the transition from shallow asthenosphere to deep asthenosphere might be, and it is likely that long period MT data collected along the edge of the Cordilleran thrust belt in southern Alberta will be sensitive to a shallowing of the asthenosphere towards the west.

Broadband MT (collected at periods between 0.01s and 1000s) was also collected in the foothills along the western edge of Alberta by Xiao & Unsworth (2006). These data showed that some of the complex and relatively shallow structure caused by thrust faults related to the Rocky Mountains could be imaged using the MT technique.

3.6 Summary

The previous MT data collected in Alberta has shown that the WCSB can be described by a 1-D layer with resistivity values between 5 and 10 Ω-m. In contrast, the Precambrian basement is not 1-D and the general N45°E strike direction indicates the presence of major conductors. MT data collected in the vicinity of the Vulcan Structure has shown that the strike angle deviates from N45°E to angles closer to N15°E. The short to mid periods (<1000s) appear to be 2-D as a whole, and there are indications for widespread 3-D structure throughout the Loverna Block at long periods (this may also represent a fundamental issue with dimensionality analysis of MT data).

Two major resistivity anomalies have been mapped within the crust of southern Alberta: the RDC, and the SABC. The RDC seems to follow the Red Deer High in the magnetic anomaly map of Alberta, separating the Archean Loverna block from the Proterozoic Lacombe Domain. A discontinuous conductor in the crust (possibly anisotropic) appears to dip to the southeast from the RDC, following reflection fabrics noted in crustal scale seismic reflection surveys.

The SABC conductor appears to be lined up with the RDC in southern Alberta, also located within the crust. Little is known of their relationship since it was discovered using MV arrays which have little depth resolution.

The apparent resistivity in the TE and TM modes show a major split, which may indicate intrinsic anisotropy, or it may indicate complex geo-electric structure. Problems trying to fit the data with 2-D models have indicated that the structure is likely more complex than an isotropic 2-D model, meaning it is either:

a) anisotropic and 2-D,
b) 3-D,
c) anisotropic and 3-D

An MT Study in northern Alberta has indicated that isotropic 3-D modelling can fit MT data collected in Alberta, and is sensitive to the depth of the LAB (Turkoglu et al., 2009).

Therefore in order to properly model the features in the crust and upper mantle below southern Alberta a fully 3-D grid of data is required.

This grid of data will allow for a systematic mapping of the LAB as well as defining the electrical structure within the crust and upper mantle. The LAB is an important target, and knowledge of its location is important to understanding the evolution of the lithosphere, as well as giving indications of factors that control the distribution of diamondiferous kimberlites (see Jones & Craven, 2004).

Long period MT data collection in southern Alberta

Despite the previous MT studies, there is still much which is not known about the resistivity structure of the crust and upper mantle beneath southern Alberta. The previous studies showed that the 3-D nature of the lithosphere requires a grid of data to image the structure properly with MT.

To extend the existing MT data coverage into a fully 3-D grid, 73 long period MT
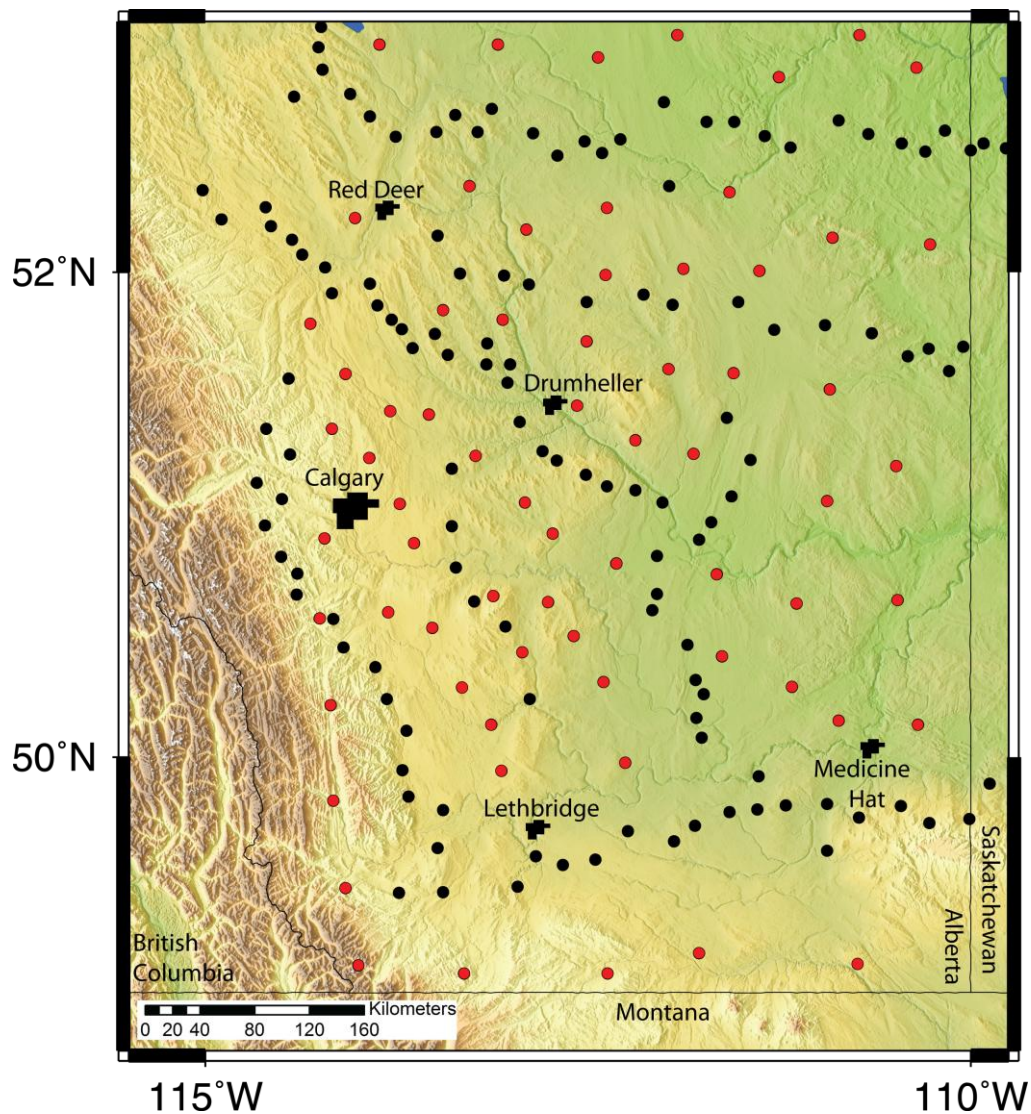
Figure 4.1: Map of the long period MT stations in southern Alberta. Black dots represent the Lithoprobe ABT data, red dots are the SAB stations collected by the University of Alberta as part of this thesis.

stations were collected during the 2008, 2009 and 2010 field seasons. Figure 4.1 shows 67 of these sites which were located in southern Alberta. The locations of the sites were chosen in order to fill in gaps between the previous Lithoprobe site locations so that a regular grid of data could be obtained.

4.1 MT data collection

MT data collection involves the recording of time variations in the magnetic and electric field in two orthogonal directions (x and y). In order to calculate the tipper data the vertical magnetic field is also recorded. Figure 4.2(a) shows a typical arrangement used for an MT station deployment. The magnetometer measures all three components of the magnetic field (x, y, and z), and the electric field is measured over dipoles, each 100 m in length giving x and y measurements.

Figure 4.2(b) shows the equipment used by the University of Alberta for long-period MT recording. The grey box contains the data logger and associated hardware (NIMS- Narod Intelligent Magnetotelluric System), the white cylindrical tube contains a three component flux-gate magnetometer, and the small black cylinders are the electrodes. The system is powered by a 12V battery, which is supplemented by a solar panel in order to allow for longer recording times. The electrode separation distances are ideally 100m, although this distance is dictated by the terrain at each site. Each station recorded data for up to one month, allowing for a statistically significant estimate of the long period response, which under good conditions gives acceptable results for periods up to 10,000 seconds. The signals were sampled at 8 Hz, allowing the shortest estimated period to be 4
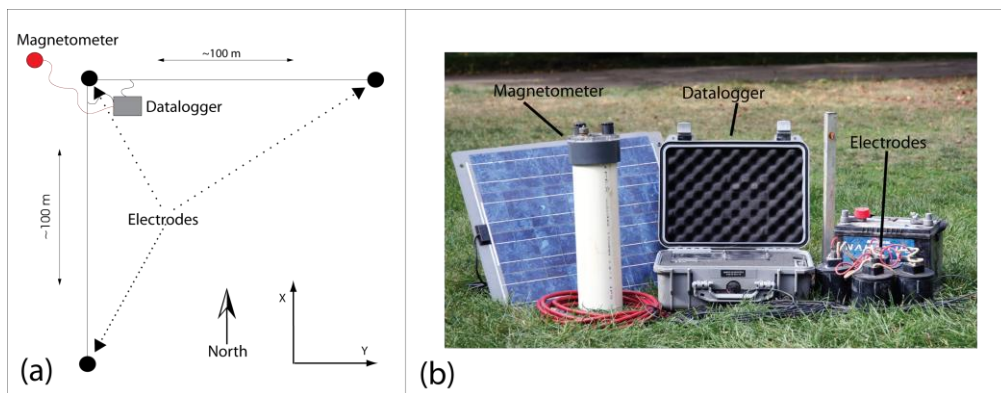
Figure 4.2: (a) - map view of an typical MT setup, (b) – MT equipment used by the University of Alberta. Photo courtesy of Ted Bertrand.

Hz under ideal conditions. Recording times varied from 2 weeks to 4 weeks, as dictated by the quality of the sounding available during regular maintenance checks.

The Lithoprobe MT data which were also used in this study were collected with the LIMS instrument (Long period Intelligent Magnetotelluric System). This instrument had a 5s sample rate, giving a bandwidth of 20 - 10,000s.

4.2   Field Conditions

Because the prairies of southern Alberta are mostly covered in farmland, many of the MT sites collected for this study were deployed in fields. Stations were commonly placed in the corners of fields where they would not interfere with agricultural activity. Stations were not placed next to pipelines or power lines to avoid electrical noise. This often meant that the east-west and north-south electrode placement was dictated by the orientation of the fence-lines, which are nearly always based on grid north (not magnetic north). In these cases, the electric field data were rotated into the same coordinate frame as the magnetic field data which were always measured in the geomagnetic coordinate frame.

The start of the 2009 field season was delayed because of funding issues, which resulted
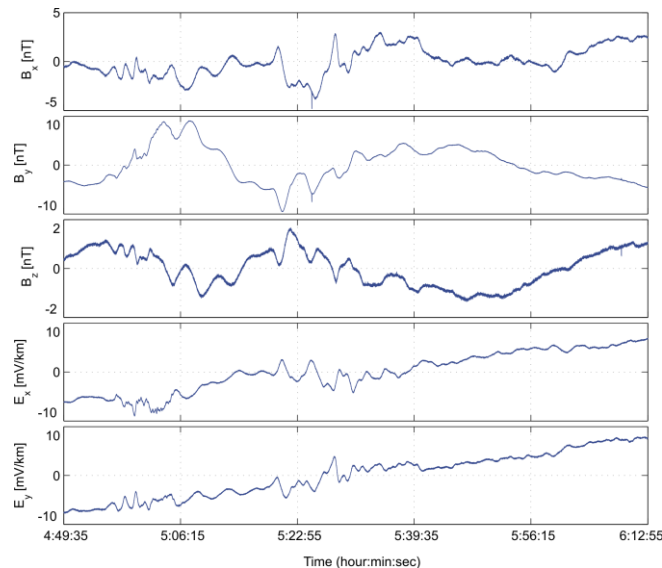
Figure 4.3: An example of the time series collected at a long period MT station (sab140). This section of time series was collected on October 8, 2010 between about 5 and 6 am (this section of time series is 5,000 seconds long). The top three channels are the magnetic field in the x, y, and z directions, the bottom two channels are the electric field in the x and y directions.

46

in data collection finishing in late fall. All of these NIMS stations were installed in unfrozen ground, but several of the stations were picked up in November when the ground had begun to freeze. A comparison of the stations collected in unfrozen ground versus the data collected in frozen ground showed that the time the electrodes were buried in frozen ground resulted in no discernible negative effects on the data quality.

One of the major hurdles to collecting high quality long-period MT data in southern Alberta was the large number of natural gas pipelines, particularly in south-eastern Alberta near Medicine Hat. Corrosion of gas pipelines is reduced by cathodic protection, which requires that electric currents are forced to flow in the pipeline. This current can interfere with the naturally occurring electric field and bias MT results. Often pipelines are marked at road crossings, and their locations can be inferred from wellheads, but in some situations it was difficult to determine where pipelines might exist. This resulted in a few MT stations whose data appeared very noisy and could not be used in the data inversions.

4.3   Southern Alberta long period MT data

A sample of the MT time series collected on October 8, 2009 at station SAB140 is shown
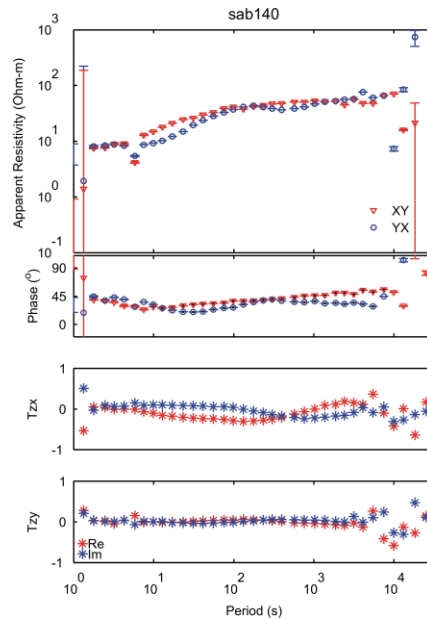
Figure 4.4: MT sounding curve obtained from station SAB140. The top panel shows apparent resistivity, the second panel shows the phase, and the two bottom panels show the tipper (T_{zx} and T_{zy} respectively).

in Figure 4.3. The magnetic field components in the x, y, and z directions are shown in the upper three panels, and the electric field in the x and y directions are shown in the lower two panels. Note that the x direction points north, and the z direction points vertically downwards.

The time series are converted into the frequency domain using Fourier transforms, as discussed in the Appendix, which then allows the apparent resistivity, phase, and tipper values to be calculated. Figure 4.4 shows the MT sounding curves obtained at station SAB140, with the apparent resistivity and phase at the top and the tipper in the *zx* and *zy* directions at the bottom. The xy apparent resistivity and xy phase were computed from the electric field in the x direction (north) and the magnetic field in the y direction (east) respectively. The tipper in the *zx* (T_{zx}) direction is related to conductors located north or south of the site, and T_{zy} is related to conductors located to the east or west of the station.

Values of apparent resistivity and phase at short periods (~1s) and values at long periods (>9,000s) at this site are much more irregular than values between these two periods. This indicates that noise or a lack of data causing inadequate statistical averaging is distorting the data. Before modelling the MT data, these points were removed.

The grid of MT data over southern Alberta can be subdivided into 4 very broad categories based on features observed in the data. Figure 4.5 shows a typical MT sounding from each category and where the categories are generally located. These soundings have all been rotated to a co-ordinate system of N45°E, following the strike direction determined in the following section.

Nearly all of the soundings show a definite split between the xy and yx data except for the soundings collected within the Medicine Hat Block (bottom right in Figure 4.5). The grey area which correlates with the western portion of the Loverna Block is characterized by a downward inflection of the xy curve, culminating in the notch observed in the MT data along the edge of the Lacombe Domain associated with the RDC. The white portions of the map are very similar, except that both modes show a downward inflection at long periods in the Proterozoic terranes to the west, while the soundings in the eastern white portion tend to show quite flat curves to long periods.

4.4 Dimensionality of the southern Alberta long period MT Data

As discussed earlier, the Lithoprobe Alberta Basement data were analyzed by Jones et al. (2002) using the tensor invariant methodology of Weaver et al. (2000). This showed that the long period data (> 1000s periods) showed effects related to three dimensional resistivity structure. Strike determination by Boerner et al. (2000) showed that a strike angle of N45°E was required by MT data at many of the MT stations in period band 4-1000 s. At periods less than 4s the MT data showed a predominately 1-D nature, with no consistent strike direction, which is expected in a sedimentary basin (Jones et al. 2002).

In this thesis, the tensor decomposition approach of McNeice & Jones (2001) is used to investigate the dimensionality. This method has the advantage that it finds statistically robust distortion parameters by fitting multiple frequencies with a single distortion model. The goal of this dimensionality analysis is to find if there is one regional strike direction which describes the entire period band (1 to 10,000 s), or if the data are more complicated and cannot be fit with a 2D model.
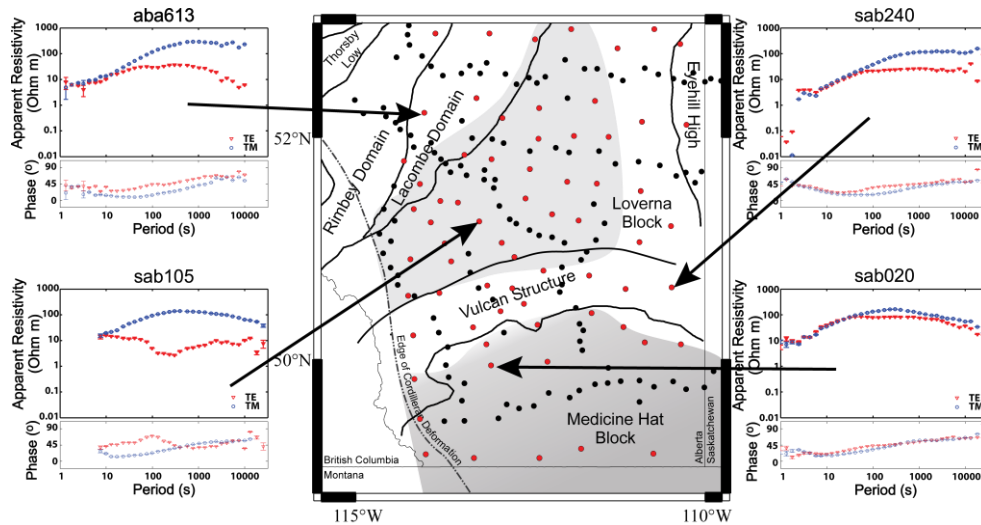
Figure 4.5: Southern Alberta can be generally characterized by three different types of MT soundings. In the south (dark gray), the Medicine Hat Block is characterized by relatively 1-D MT data, The Vulcan Structure and eastern Loverna Block show a split in the TE and TM modes which is relatively consistent to long periods, the western Loverna Block shows affects from a conductor in the TE mode, but none in the TM mode, and north of the Loverna Block there is a split between the modes, but they both show effects from the conductive asthenosphere at long periods.

49

Results of the tensor decomposition are shown in Figure 4.6. The most striking feature when determining a regional strike angle for southern Alberta is a change which consistently occurs at about 1000 seconds. Figure 4.6(a) shows strike angles determined by fitting the period band from 1 to 1000 seconds with a single strike, shear, and twist angle for each station. Figure 4.6(b) shows the same, but for the period band 1000 to 10,000 seconds. The rose diagrams in Figure 4.6(c) and (d) show a stacked image of all the strike angles from their corresponding period band. The red and blue angles highlight the 90° ambiguity inherent to strike angle determinations (based on this data alone it is impossible to know whether the red or blue line correspond to the real geoelectric strike). The misfit map in Figure 4.6(e) shows that the data in the period band 1000s to 10,000s is fit well by this tensor decomposition.

The shorter periods (below 1000 seconds) show a very consistent strike direction in Figure 4.6(a) and (c), and longer periods (b and d) show much more scatter in the determined strike directions at each station. The strike map for the longer period band (Figure 4.6(b)) shows a relatively smooth change in strike angles from ~N45°E at 53°N to ~0° at 50°N.

This can be seen more clearly in Figure 4.7, which shows rose diagrams for the strike angle within each 1° X 1° box. There are a number of regions which still show a dominant N45°E strike angle (i.e. northwest corner of Figure 4.7), but there are also a number of blocks which show the strike changing to closer to 0° (or 90°, seen most clearly north of 50°N and east of 113°W).

Therefore, it appears that the MT data in southern Alberta are characterized by a dominant regional strike angle of N45°E at periods shorter than 1000 seconds, and a much less consistent strike angle for periods greater than 1000 seconds. If this is true, then by holding the strike angle at N45°E for each station, the tensor decomposition should fit the short periods (< 1000s), but not the long periods (1000s to 10,000s).

 The validity of this assumption can be investigated by undertaking a second decomposition with the strike angle fixed at N45°E. In this decomposition, the twist and shear angles are estimated and the misfit between the measured and predicted impedances can be computed (Figure 4.8).   These maps show how well a 2-D model oriented at N45°E can be used to describe the data.
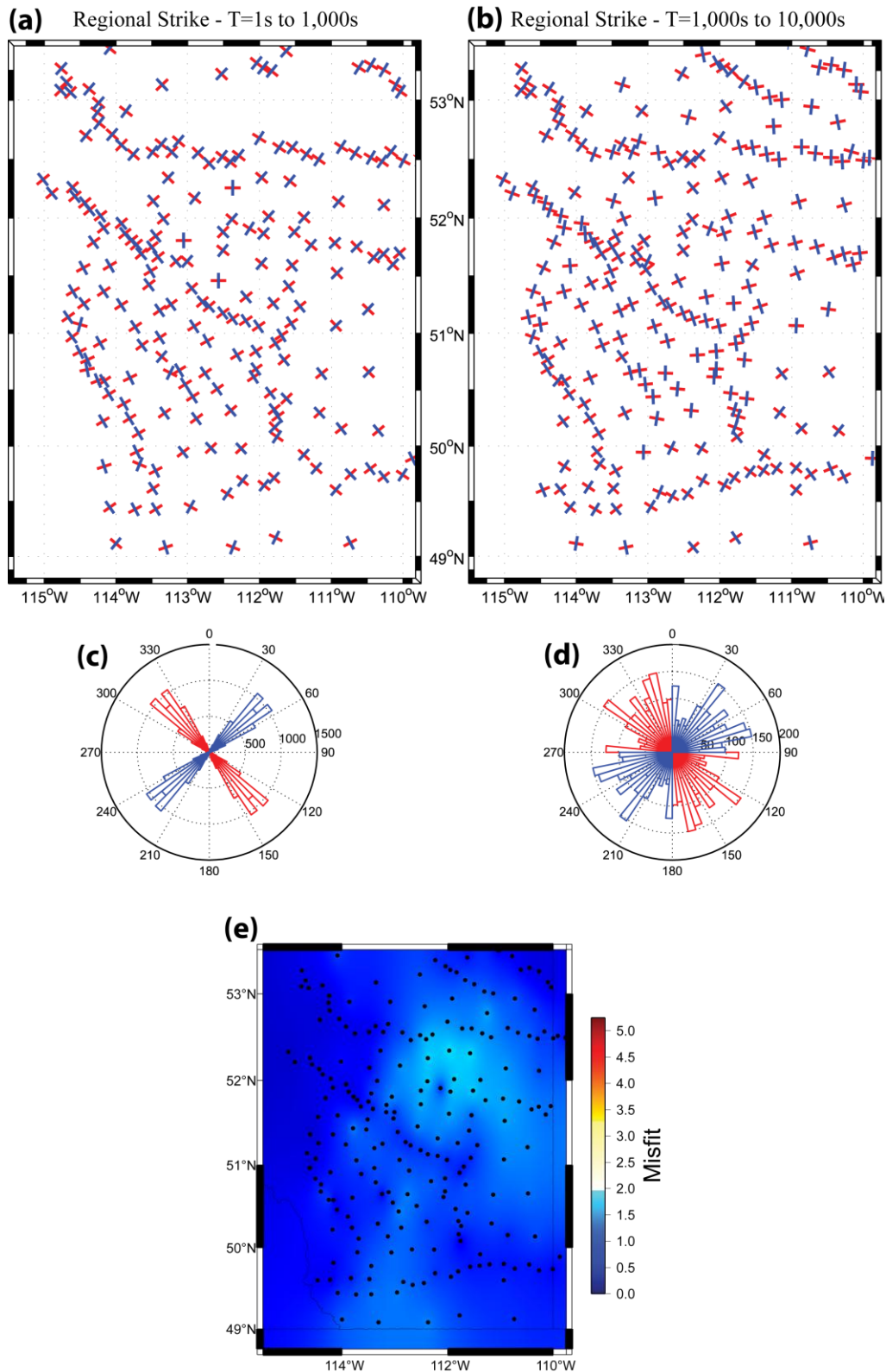
Figure 4.6: Regional strike determination for data in southern Alberta. (a) shows strike directions for the period range of 1 to 1000 seconds, (b) shows strike directions determined for the period band 1000 to 10,000 seconds. The rose diagrams in (c) and (d) are stacked images of all the strike directions in southern Alberta, and the misfit map in (e) shows the small misfit values which result from trying to fit the data in the period band 1000s to 10,000s.

51

The misfit shows that at short periods (< 100 seconds), the data near the Rocky Mountain Foothills (the western edge of southern Alberta) shows high misfit values. Between 10 and 100 seconds distortion caused by the RDC becomes apparent in the north, and above 100 seconds the foothills are no longer distorting the data, but poor misfit near the RDC begins to become widespread. At long periods (> 1000 seconds), the misfit over much of southern Alberta is relatively large, indicating the difficulty for a N45°E oriented 2-D model to fit the data. This long period map can be contrasted with the misfit map in Figure 4.6(e) which shows the misfit that is possible by allowing the strike to be free in the tensor decomposition for the period band 1000 to 10,000 seconds.

The map in Figure 4.6(e) shows that the data at long periods can be described by a 2-D tensor decomposition model, but as indicated by Figure 4.6 to Figure 4.8, there is no
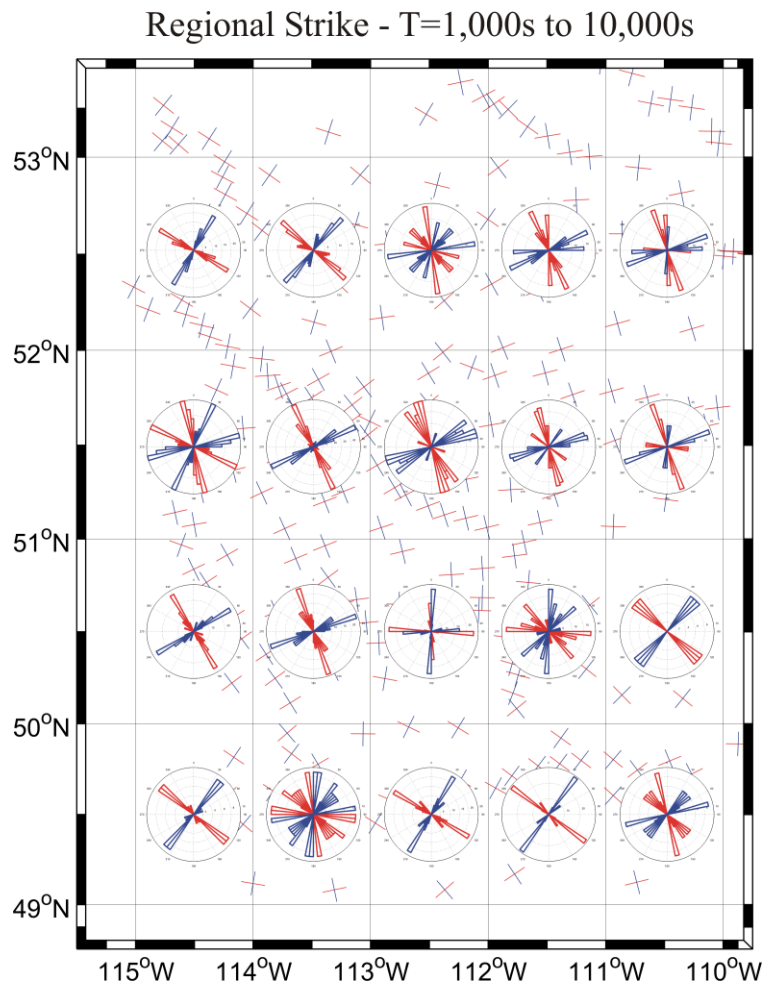
Figure 4.7: Rose diagrams of strike angles within the period range 1000s to 10,000s for each 1° by 1° block in southern Alberta. The strike angles show a large change between different regions, indicating the difficulty for 2-D data analysis to accurately describe this data.

consistent 2-D orientation which can describe the long period data.

This conclusion appears to stand in opposition with the tensor invariant analysis by Jones et al. (2002), although they explain that the apparent long period 3-D structure could be related to true 3-D structure, or it could represent a fundamental limitation of dimensionality analysis related to different impedance tensor elements being sensitive to
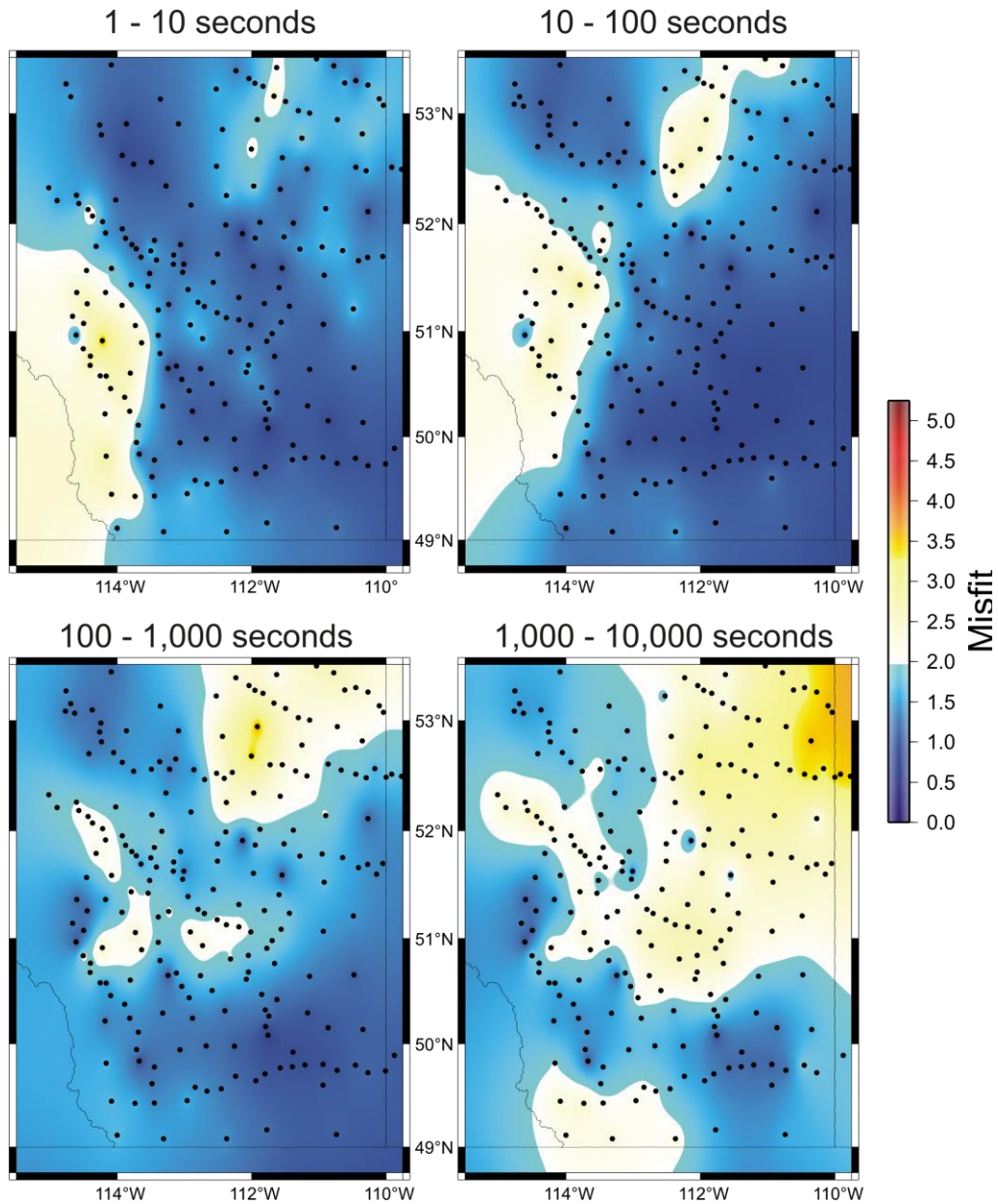
Figure 4.8: Maps of the misfit between the measured data, and the distortion model at 4 different period bands. The strike angle has been fixed to N45°E, while the shear and twist angles are left free to change from station to station.

different skin depths. Regardless of whether the long period MT data is 3-D or 2-D without a consistent regional strike direction, it would be irresponsible to model the long period data with a 2-D model.

Therefore, in order to find which subset of the MT data is not affected by galvanic distortions, and is acceptable to use for 2-D analysis, tensor decomposition of the period range 1 to 1000 seconds was undertaken using the method of McNeice & Jones (2001). Since the strike angle for this period band has been shown as N45°E, (Figure 4.6(c)), the MT profiles chosen are oriented the same.

One method for determining the affects of galvanic distortion on the data is by looking at the shear and twist angles shown in Figure 4.9. Values greater than 10° and less than -10° correspond to stations which most likely contain galvanic distortion affects. The shear angle shows negative values which generally follow the trend of the RDC, with local high values at a few stations spread out across southern Alberta. The twist angle is generally small throughout southern Alberta, with a few large values along the Foothills in the west. In general, the values of shear and twist are fairly small (< 45°), although the distortion caused by the foothills stations and the RDC stations means that their data is avoided in 2-D modelling where possible.
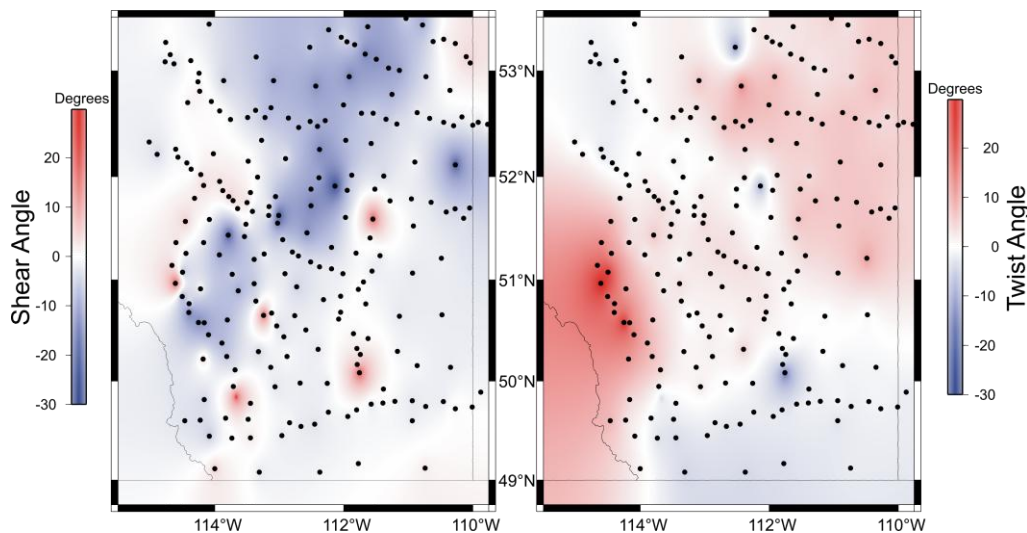
Figure 4.9: The shear angle (left), and the twist angle (right) resulting from tensor decomposition of the 1 to 1000 second period band.

4.5   Induction Vectors (Tipper)
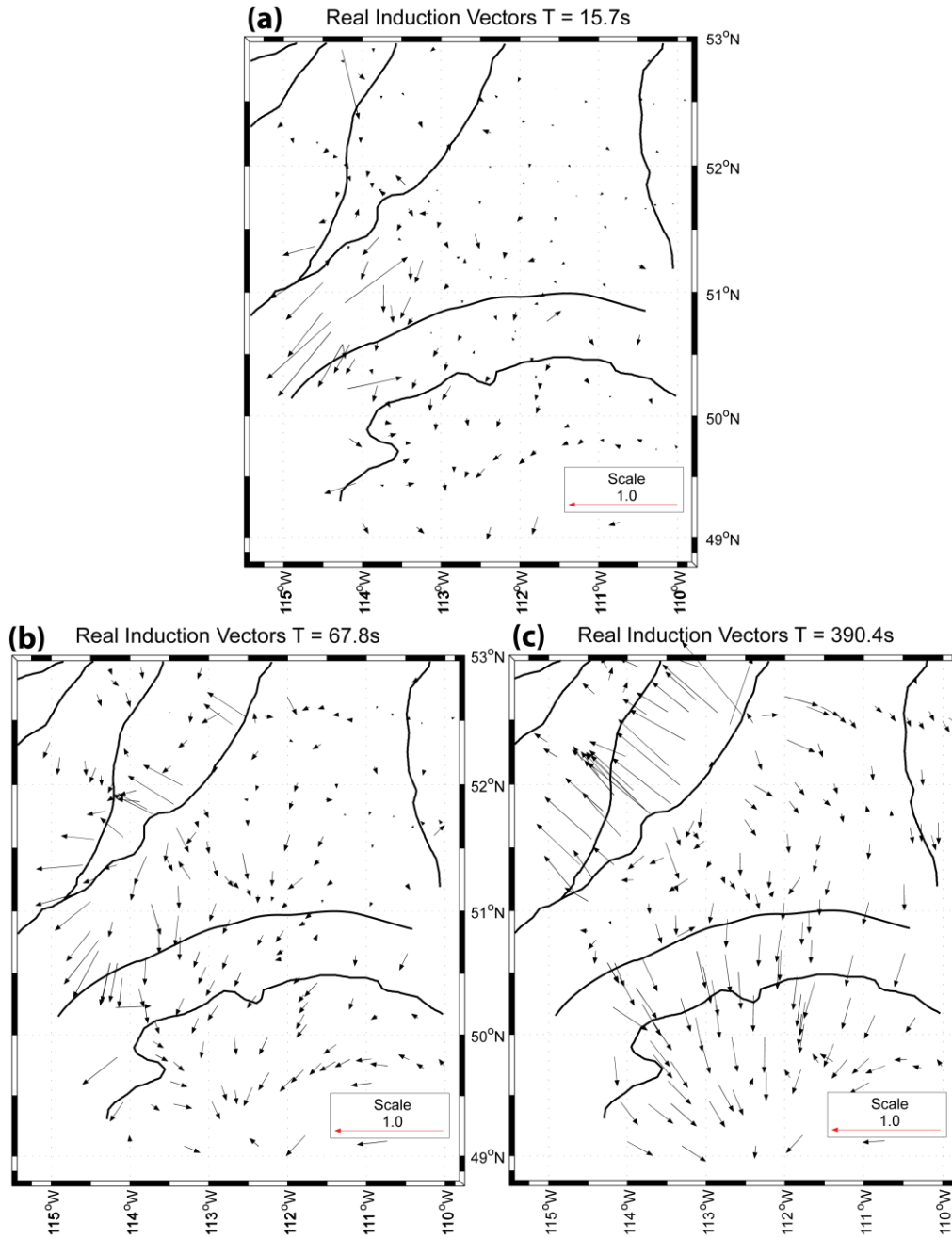
Figure 4.10: Real induction vectors at four different periods plotted in the Weise convention (pointing away from conductors). The black lines represent the Precambrian terrane boundaries.

Maps of induction vectors calculated from the tipper data indicate where conductors exist (see Appendix A). Because of this, they can be used to resolve the inherent 90° ambiguity in strike angle determination. Note that some authors suggest this approach should be used with caution (Jones & Groom 1993). This is because if a region is 2-D, conductors will be parallel to the strike direction, and induction vectors should point at
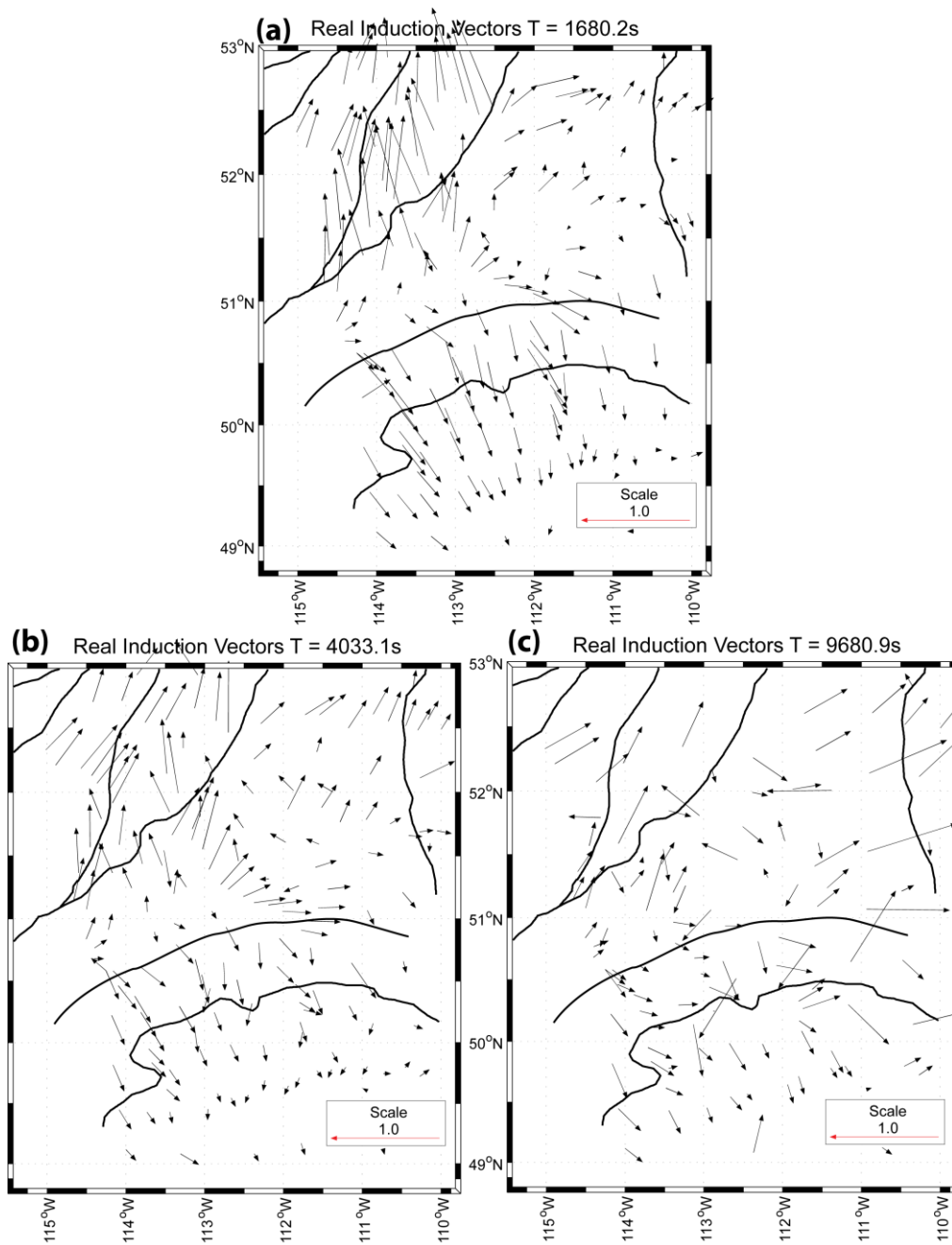
Figure 4.11: Maps of induction vectors continued from Figure 4.10 (plotted in the Weise convention, pointing away from conductors.

right angles to strike direction. Boerner et al. (2000) noted that the induction vectors from the Lithoprobe data point anti-parallel to N45°E as a whole, and conclude that this is the regional strike direction over southern Alberta. This direction agrees with the strike of the RDC and the SABC conductor (see chapter 3), and agrees with the geological strike direction of the Precambrian terranes below the WCSB. Because no evidence suggests that the geo-electrical strike is not N45°E, and the evidence above suggests that it is, we will follow Boerner et al. (2000) and consider the geo-electrical strike direction to be N45°E.

Figure 4.10 and Figure 4.11 show maps of the induction vectors following the convention of Wiese (1962) where vectors point away from regions of lower resistivity.

The short period vectors (15.7s – Figure 4.10(a)) correspond to signal penetration within the WCSB, and shows small induction vectors throughout most of southern Alberta, except for along the foothills. The large vectors in the foothills seem to show an approximately N-S striking conductor within the southern-most portion of the Loverna block, and the small induction vectors represent the 1-D nature of the sedimentary basin.

Induction vectors at 67.8 seconds (Figure 4.10(b)) show that the horizontal resistivity gradients are becoming larger, as indicated by the larger induction vectors. This period corresponds to a depth penetration within lower to middle crust level, and begins to show affects from the RDC (these are the large induction vectors pointing northwest). An interesting phenomenon appears in the south, where all the induction vectors curve around to point at a resistor near the USA border.

At a period of 390.4 seconds (Figure 4.10(c)) the RDC becomes quite apparent in the northwest. It is interesting to note that induction vectors to the north of the Red Deer High point away from it, and induction vectors to the south of the Red Deer High are quite small and less consistent. The opposite effect occurs at the Vulcan Structure, where vectors point away from the apparently low resistivities in the Loverna Block to the south.

This effect remains at a period of 1680.2 seconds (Figure 4.11 (a)), except that the large induction vectors in the north appear to also sense a conductor to the west. This period shows an obvious reversal of the induction vectors below the south end of the Loverna block, indicating the presence of a conductor. The induction vectors in the far south and

east are all quite small, indicating that they no longer sense any large horizontal resistivity gradients.

Figure 4.11 also shows induction vectors at 4033.1s (b), and 9680.9s (c). The induction vectors at 4033.1s show a similar situation to those at 1680.2s, except that affects from the RDC are no longer obvious. The induction vectors to the south remain quite small, but in the north many point away from a conductor to the southwest. This may be related to the crossover of vectors in the south end of the Loverna block, although vectors in the northwest are pointing away from a different area further west (possibly related to the shallow and conductive asthenosphere which underlies the Canadian Cordillera to the west.

The induction vectors at a period of 9680.1s (Figure 4.11(c)) are much less consistent, likely owing to the noisy magnetic data at that period in many of the stations. The stations with good data have vectors pointing to the southeast in the south, and may be pointing to the northeast in the north. This is likely related to the conductor beneath the Loverna block, and/or the low resistivity in the asthenosphere below the Canadian Cordillera.

In summary, the induction vectors appear to show a complex resistivity structure, particularly beneath the Loverna Block. The induction vectors at the edges of the block all point away at periods which correspond approximately to signal penetration to crustal depths, while the induction vectors within the block at these periods are relatively small. This is consistent with the hypothesis that a widespread conductor exists throughout much of the Loverna block. At longer periods the conductor appears to converge at one point in the southern most portion of the Loverna block, causing an obvious crossover of vectors which all point away from a relatively small area.

This chapter has described the main features of the southern Alberta MT dataset. The next step is to generate a resistivity model that can account for the measured data.

Chapter 5
2-D and 3-D modelling and inversion

The strike analysis in Chapter 4 showed that the MT data collected in southern Alberta can be considered two-dimensional in the period band from 1 to 1000 seconds, with a strike direction of N45°E. At longer periods the data are more complicated and exhibit 3-D aspects. Impedance tensor invariant studies of the long period Lithoprobe MT data in Alberta have also shown that the data at periods between 1000s and 10,000s is not easily explained with a 2-D resistivity model (Jones et al. 2002).

These observations suggested that the MT data in the 1 to 1000 s band could be analysed with a 2-D inversion. This was to be compared to a 3-D inversion of the entire period range of 1 to 10,000 seconds over southern Alberta.
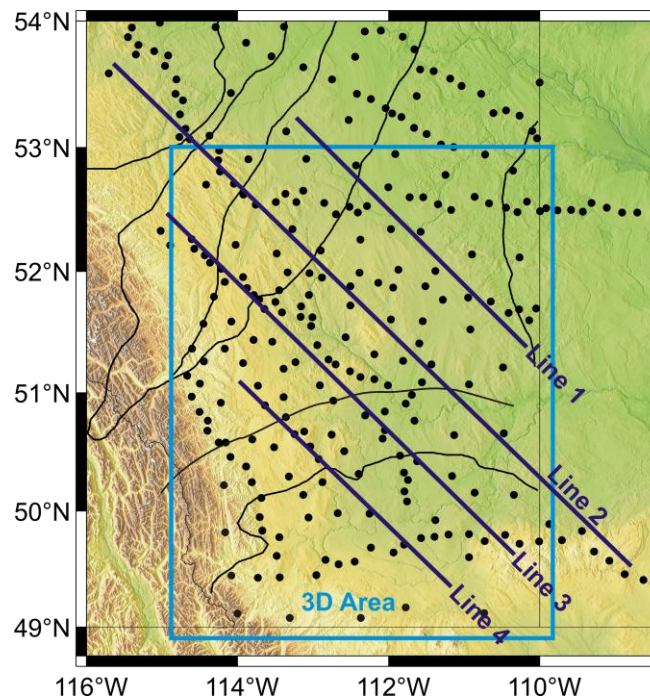
Figure 5.1: Location of the four 2-D MT profiles inverted in this study, and the area covered by the 3-D inversion model. The black dots show the location of the all of the long period MT data available in southern Alberta, the blue line outline of the area covered by the 3-D inversion, and the black lines indicate the precambrian basement terranes (see Figure 4.5 for terrane names).
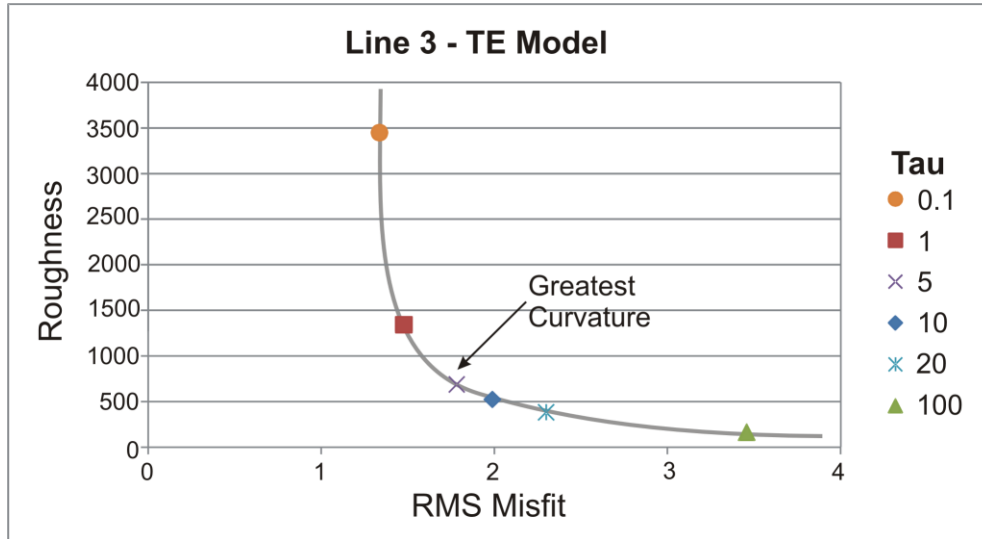
Figure 5.2: An example of an L-curve, showing that large values of tau result in a large misfit (and also a very smooth model), and small values of tau result in a very rough model with a small misfit. A trade off between roughness and misfit is chosen based on the point of largest curvature in the L-curve. For this model a tau value of 5 was used.

This was implemented by:

(a)   selecting 4 profiles of MT data (Figure 5.1) for 2-D inversion, and

(b)   selecting a grid of stations for 3-D inversion.

This chapter presents the resistivity models obtained from both the 2-D and 3-D inversions.

5.1   2-D inversion of SAB data

2-D inversions used the NLCG algorithm of Rodi & Mackie (2001). This algorithm searches for a smooth resistivity (conductivity) model that fits the data to a specified level, and is based on the Occam approach to MT data inversion (Constable et al., 1987).

2-D MT data consists of two independent modes (TE and TM) defined by current flow parallel and perpendicular to the strike direction respectively. They can be inverted separately to give two independent resistivity models, or jointly to give a single resistivity model. The tipper data is part of the TE mode and can be inverted separately, or in combination with the TE and TM data. The tipper data has less depth sensitivity, and is

usually inverted in conjunction with the other modes. The TE and TM modes are both sensitive to different features of a 2-D resistivity model.

To find a smooth model which gives a statistically acceptable fit to the measured MT data, the 2-D inversion algorithm needs to make a trade off between smoothness and data fit, since rough models can always fit the data. This is done with a trade off parameter known as tau (τ). Figure 5.2 shows the roughness vs. root mean square (r.m.s). misfit for a set of inversions using different τ values, known as an L-curve. The r.m.s misfit is large for large values of τ, and the roughness is large for small values of τ. The best trade off between roughness and misfit is chosen based on the point of largest curvature on the L-curve. For the example in Figure 5.2, a τ value of 5 was chosen.

Error floors were defined for each component of the data so that each mode and period band was given appropriate weighting in the inversion. Error floors of 5% for the apparent resistivity, 10% for the phase angle, and 0.02 for the tipper were used in the 2-D inversions.

The data used in the inversion of each profile were chosen based on the degree of distortion indicated by the tensor decomposition analysis, and how well a 2-D tensor decomposition model could fit the data when forced to a regional strike direction of N45°E. Some MT stations had a relatively high r.m.s. misfit value, indicating that the measured MT data could not be fit by a 2-D decomposition model. These stations were not used in the 2-D inversion, unless removal of the station left a major gap on the profile. Also, stations with high shear or twist angles were removed, since they correspond to stations with significant galvanic distortion.

As discussed in the previous chapter, the dimensionality analysis of the Lithoprobe data by Jones et al. (2002) and the tensor decomposition analysis using the algorithm of McNeice & Jones (2001) have indicated that the MT data at periods greater than 1000 seconds is either not 2D, or the strike angle changes at a period of 1000 seconds, invalidating a 2D model with a strike direction of N45°E. Inversions were thus restricted to the period band 1- 1000 s, so that possible distortion affects were not introduced into the 2-D inversion models.

Each of the four profiles are presented below, showing the MT data used in the inversions, and the resistivity models obtained from the inversion.

5.1.1 Line 1

Line 1 is about 300 km long, and crosses the RDC near the west end of the profile, with the majority of the profile located in the Loverna Block (see Figure 5.1). The locations of each station used in the inversion of this profile, along with induction vectors are shown in Figure 5.3. The available MT data located along this profile is not as dense as along other profiles, therefore these stations which are used are spaced relatively far apart. Because of this, the resulting inversion models should be viewed with caution.
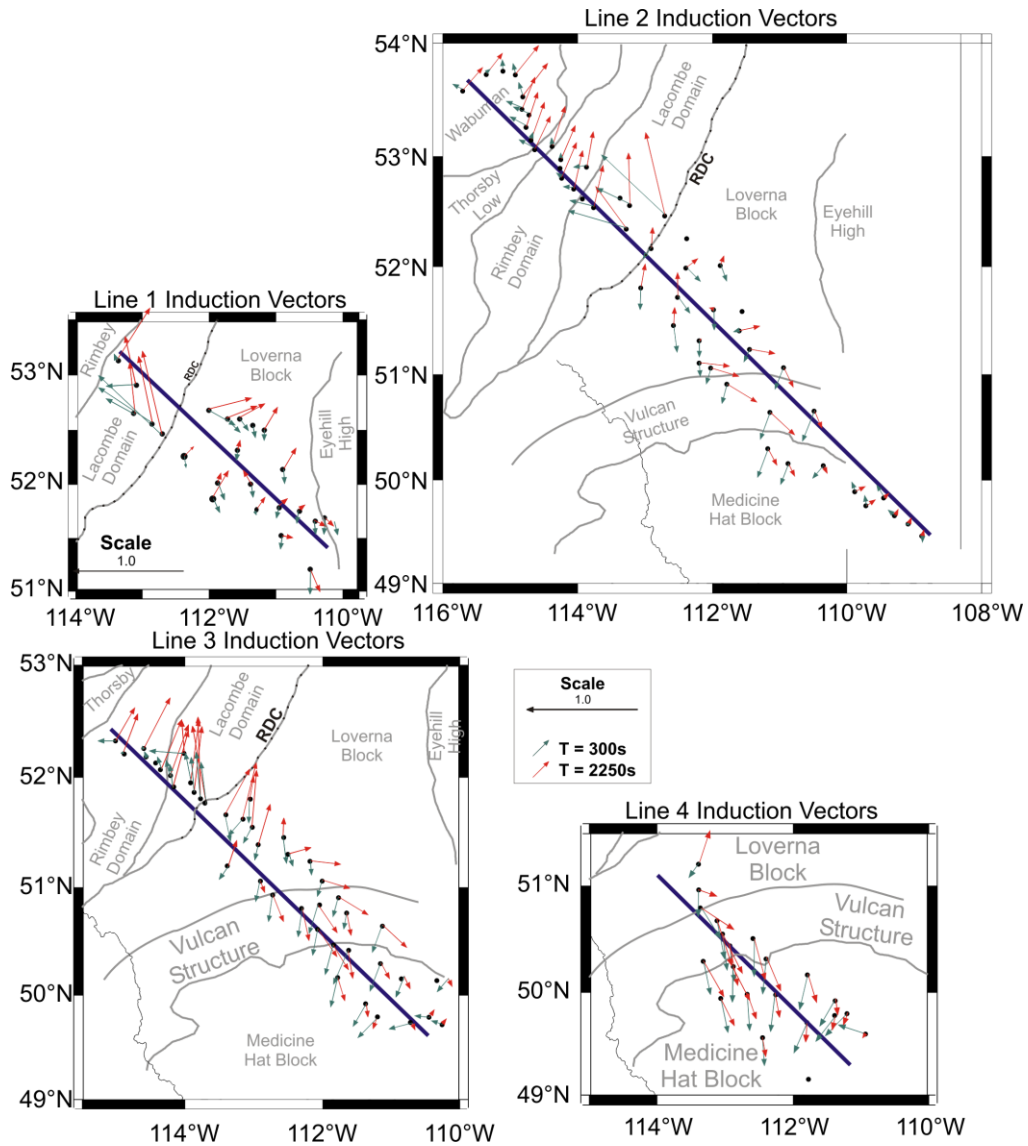
Figure 5.3: Maps of the data used in the inversion along all four lines. Black dots represent station locations, and the purple line shows the location of the profiles. Real induction vectors are plotted in the Weise convention (pointing away from conductors; Wiese, 1962).

The induction vectors in the southeast are all relatively small (with values ~0.25, Figure 5.3), indicating that the nearby horizontal resistivity gradients are also relatively small. Closer to the RDC the induction vectors become significantly larger at periods of 300 - 2,250s, confirming the presence of a large conductor at the RDC.

In a region where the resistivity structure is perfectly 2D, all the induction vectors would be aligned perpendicular to the strike direction (parallel to the profile). However, Figure 5.3 shows that many of the induction vectors do not point parallel to the profile. The small vectors in the southeast are not as important, since their small size may be due to noise rather than nearby conductors. However the large vectors in the Lacombe Domain indicate 3-D resistivity structure.

Most of the large induction vectors which point off-profile are at periods greater than 1000 seconds, possibly indicating the same resistivity structure which causes a change in strike angle beyond a period of 1000s in the tensor decomposition analysis. To be sure, the results of the strike angle determination of periods less than 1000 s have been determined.

Figure 5.4 shows the rose diagram compiled from the strike angles on Line 1, showing that the tensor decomposition requires a well-defined strike angle of N45°E based on the impedance data. The pseudo-section on the right side of Figure 5.4 shows the r.m.s. misfit of the tensor decomposition model with the strike forced to be N45°E .This provides a measure of which data are consistent with a strike angle of N45°E . The majority of the misfit values along the profile are less than 2.0, indicating that the apparent resistivity and phase are explained well by a 2D resistivity model with a strike of N45°E. This means that the induction vectors which point off profile in Figure 5.3 must be related to structure far enough away that only they are affected.

Strike Angle   Tensor Decomposition Misfit
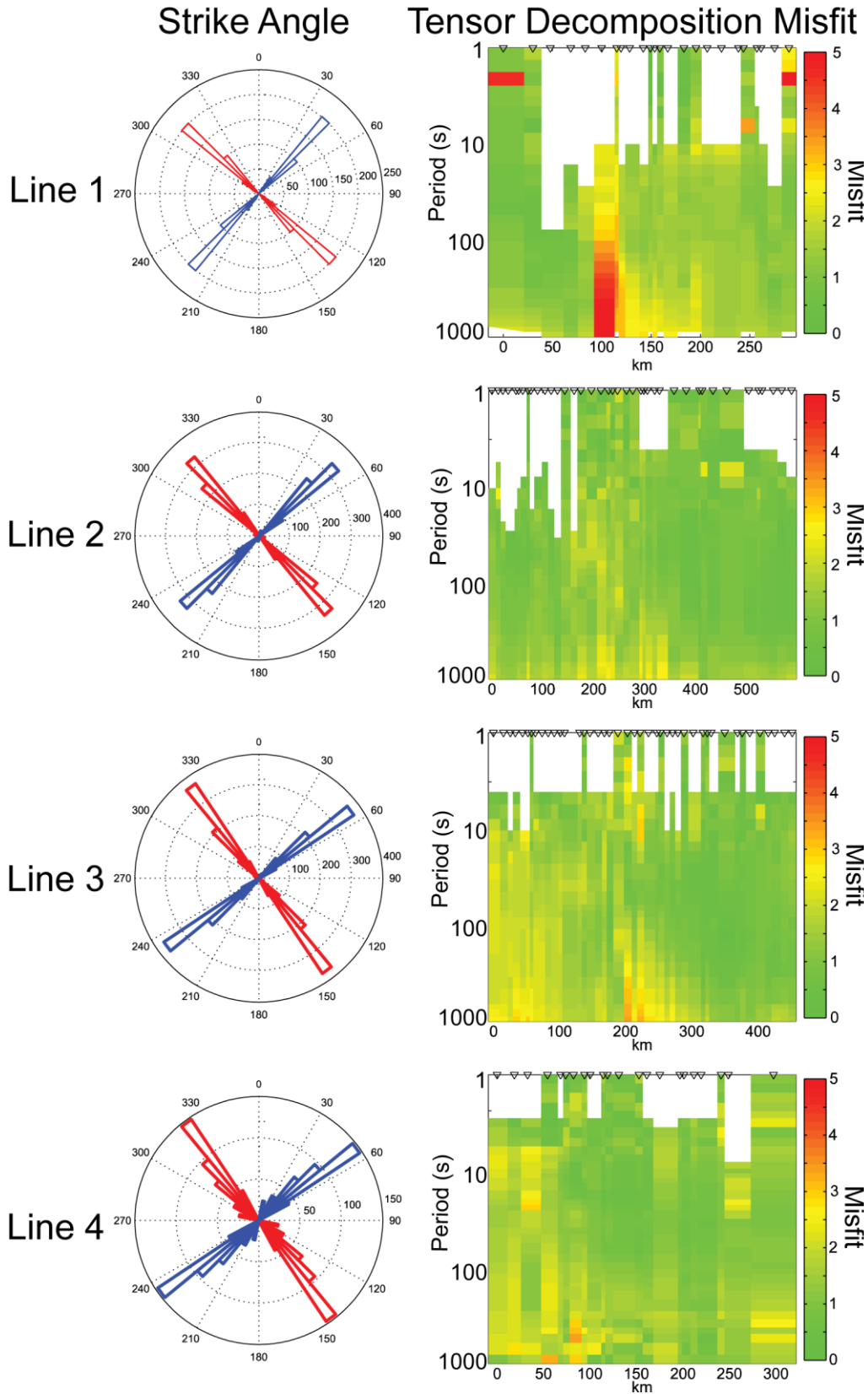
Figure 5.4: The rose diagrams on the left show strike angles obtained at each station along its respective profile in the period band 1 to 1000 s. The right image shows the misfit resulting from forcing the strike angle to N45°E in the tensor decomposition inversion. The triangles show the station locations along the profile, and the period is increasing downwards (corresponding to increasing depth in the Earth.

As mentioned earlier, strike angles determined from tensor decomposition contain an inherent 90° ambiguity. Previous analyses of the Lithoprobe MT data used a strike angle of N45°E based on the induction vectors and geological boundaries (Boerner et al. 2000; Jones et al. 2002). This is confirmed in the induction vector maps presented in the previous chapter, which show many of the induction vectors at periods shorter than 4,000 seconds pointing perpendicular to the RDC and the Vulcan structure, whose strike is closest to N45°E

The apparent resistivity and phase data along Line 1 is shown in Figure 5.5 as pseudo sections where period is increasing downward. It is important to look at the data, because features which appear in the inversion models but do not appear in the data are likely artefacts caused by errors in modelling.

The data show that the response from the RDC is the dominant feature along Line 1. The TE mode shows low apparent resistivities in the periods range   100 - 1000 s in the vicinity of the RDC, and phases which flip from ~90° to ~0° with increasing period. The imaginary and real tipper data changes from high to low across the RDC, but the TM mode shows no obvious affect from the RDC. This is indicative of a thin conductor oriented parallel along strike, where the electric field along strike is highly sensitive to the conductor in the TE mode, but the electric field across the conductor (TM mode) is hardly affected.

Figure 5.6 shows the models obtained from an inversion of the data along Line 1, labelled with the r.m.s. misfit. The r.m.s misfit gives an overall measure of how well the model responses fit the measured data, where a value of 1.5 generally indicates an acceptable fit. The first model is the result of an inversion using only the TE mode, and shows a discontinuous conductor which dips to the southeast. The conductor appears to smear below 50 km at the southeast end, but it is likely that this is an artefact of the inversion, resulting from the fact that MT data has little sensitivity below conductors.

The model obtained from the TM inversion shows the sedimentary basin with low resistivities above a resistive half-space, but no indication of the conductor observed in the TE inversion model.
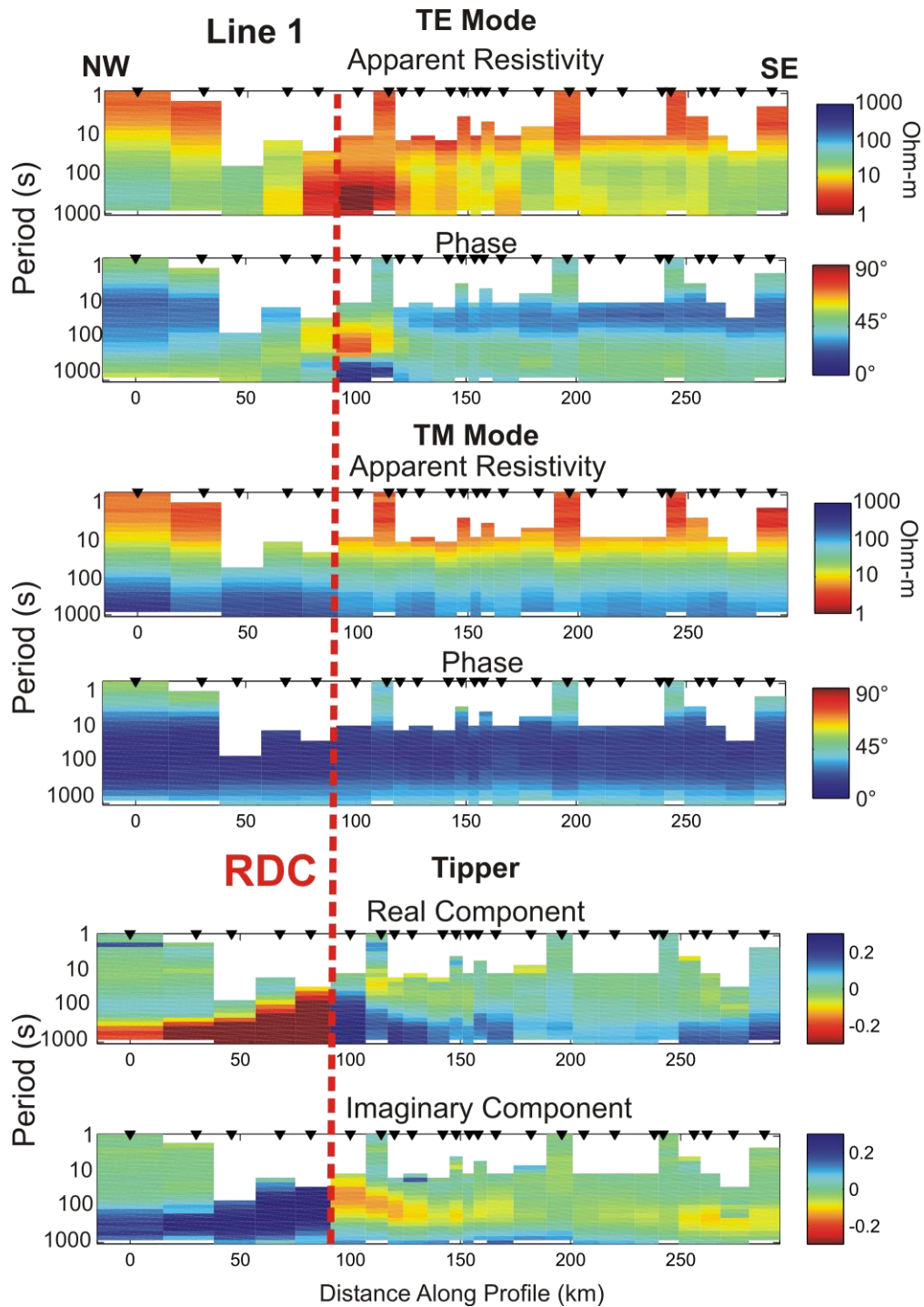
Figure 5.5: The apparent resistivity, phase, and tipper data from Line 1. Period is increasing downwards in each section as a pseudo depth section, where the black triangles show the locations of the MT stations along the profile. The TE mode and tipper show obvious affects from the RDC, but the TM mode is relatively unaffected. The white areas represent lack of data, usually corresponding to the smaller bandwidth of the Lithoprobe LIMS data relative to the NIMS data which usually covers the entire band width.

66
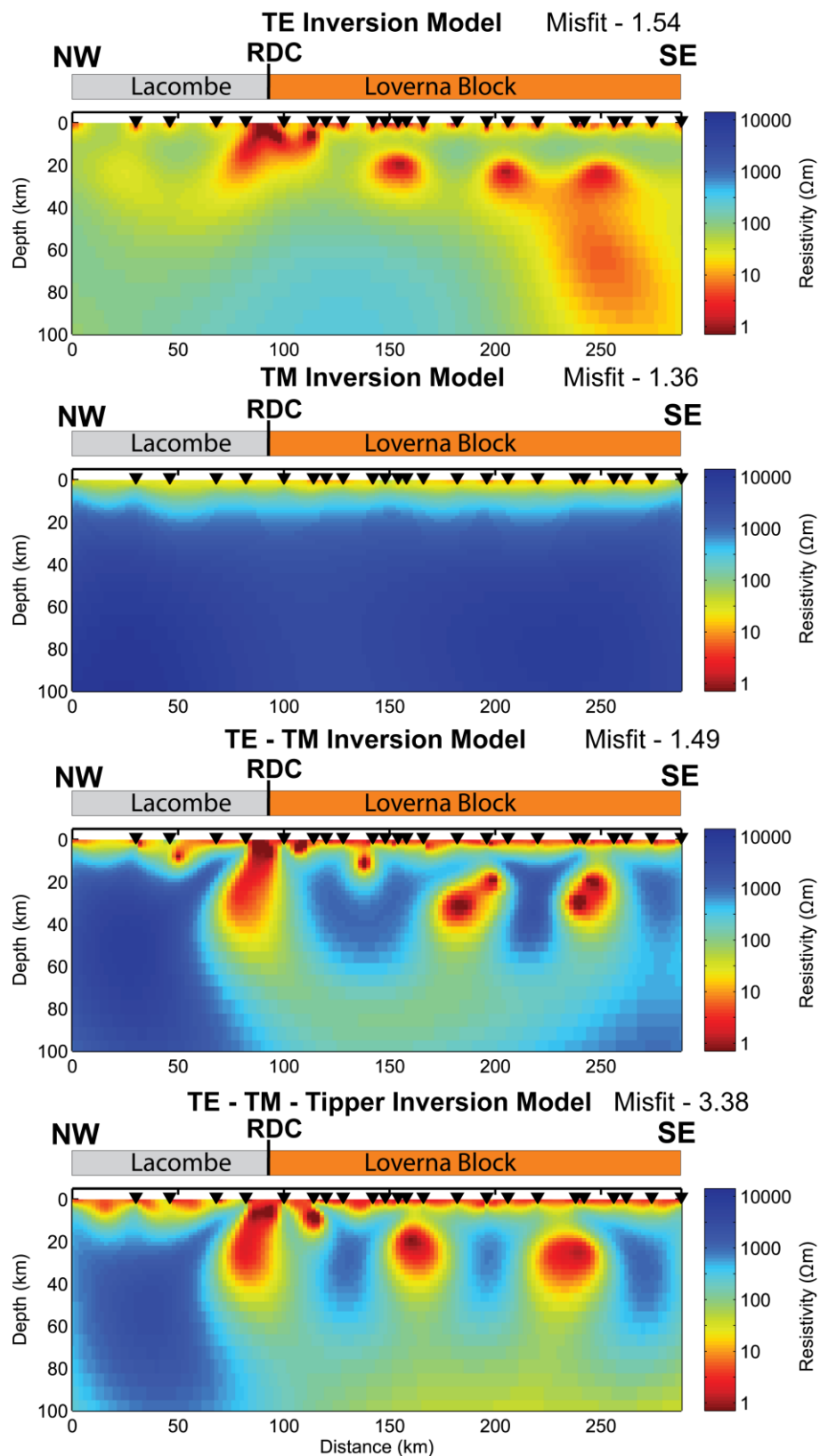
Figure 5.6: Inversion models obtained from an inversion of the data on Line 1. Models fit the TE, TM, and TE-TM data well, with an r.m.s misfit value around 1.5 or less, but the addition of the tipper data made it difficult to fit the data (bottom). RDC – Red Deer Conductor. Lacombe – Lacombe Domain.

A simultaneous TE – TM inversion was then undertaken to fit both modes. This produced a resistivity model that contained a number of small features with low resistivities. The locations of these conductors were somewhat similar to those observed in the TE model, but not exactly the same. This indicates that while the data requires discrete conductors, their locations are not uniquely defined.

The final inversion model shown in Figure 5.6 indicates that the addition of the tipper data caused the r.m.s. misfit to increase significantly. This model resembles the TE-TM model, but the location of the discrete conductors has changed.

5.1.2   Line 2

Line 2 is over 650 km long, with 47 stations stretching from southern Saskatchewan to central Alberta, and crossing both the RDC and the Vulcan Structure. Figure 5.3 shows the location of the profile with respect to the Precambrian basement terranes.

The induction vectors in Figure 5.3 show small magnitudes in the southeast, corresponding to a region with 1-D lithosphere structure (Boerner et al., 1999). At the short period of 300 seconds the vectors are relatively small except for ones north of the RDC and south of the Vulcan Structure. The Vulcan Structure vectors are at right angles to the Vulcan Structure, away from the Loverna Block, and change direction at longer periods. As discussed in the previous chapter, this could indicate a conductor within the Loverna Block, causing large induction vectors at its boundaries.

The strike angle resulting from tensor decomposition is shown in Figure 5.4. All of the strike angles over the profile show a consistent direction of ~N45°E, and the misfit resulting from forcing the strike angle to N45°E shows that all of the stations can be acceptably fit with the strike direction fixed at N45°E.

The pseudo sections for Profile 2 are shown in Figure 5.7. As with Line 1, the most obvious feature in these data is the RDC. The Vulcan Structure is marked by the gray shaded region under the sections, and marks the edge of a conductor which is seen at long periods in the TE mode, and also marks the edge of large magnitude tipper data in the real component. This conductor begins at the RDC, and appears to dip slightly to the southeast, as defined by the TE phase data.
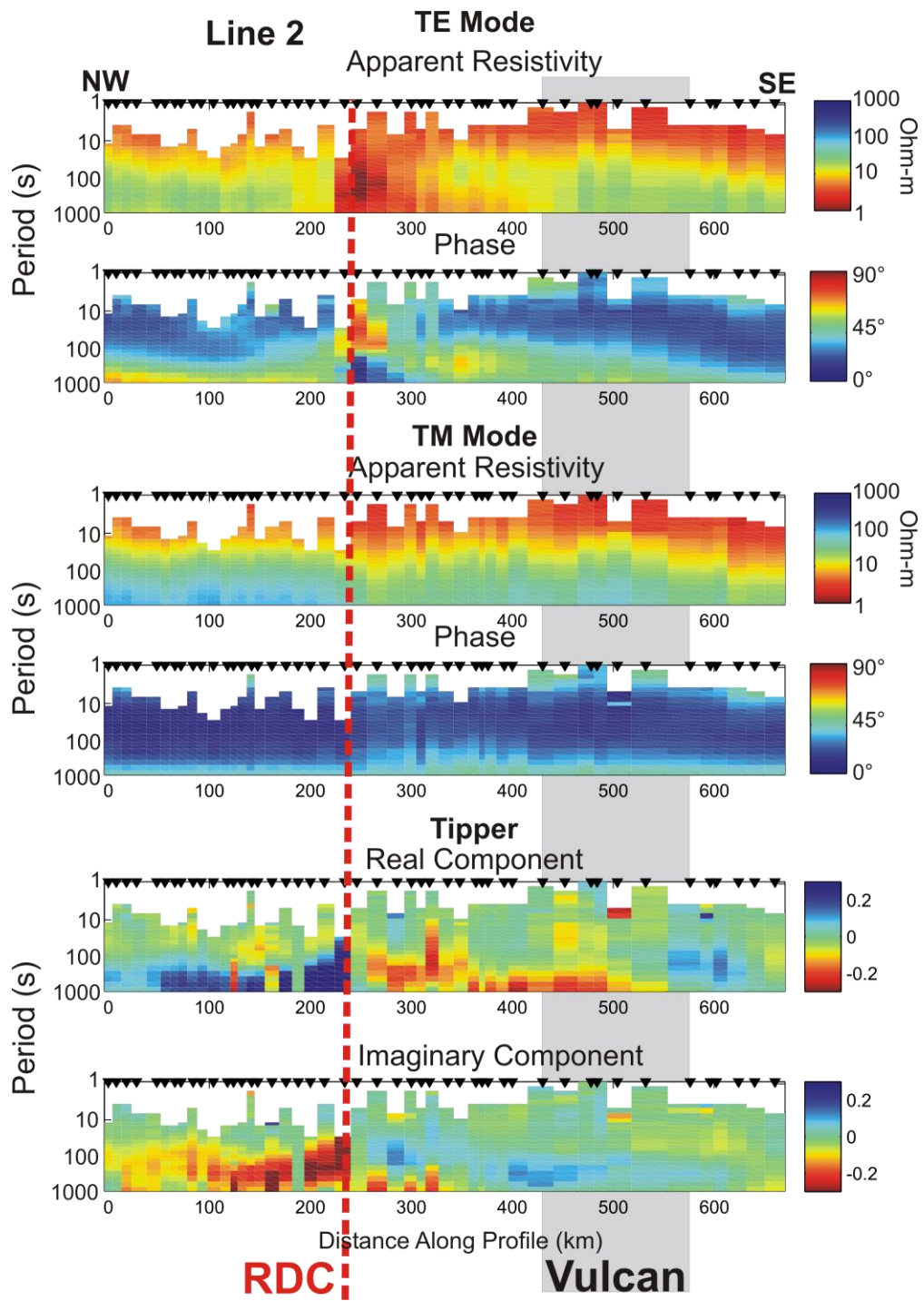
Figure 5.7: Pseudo sections where period is increasing downwards as a pseudo depth. The sections show the data collected at each station along Line 2.
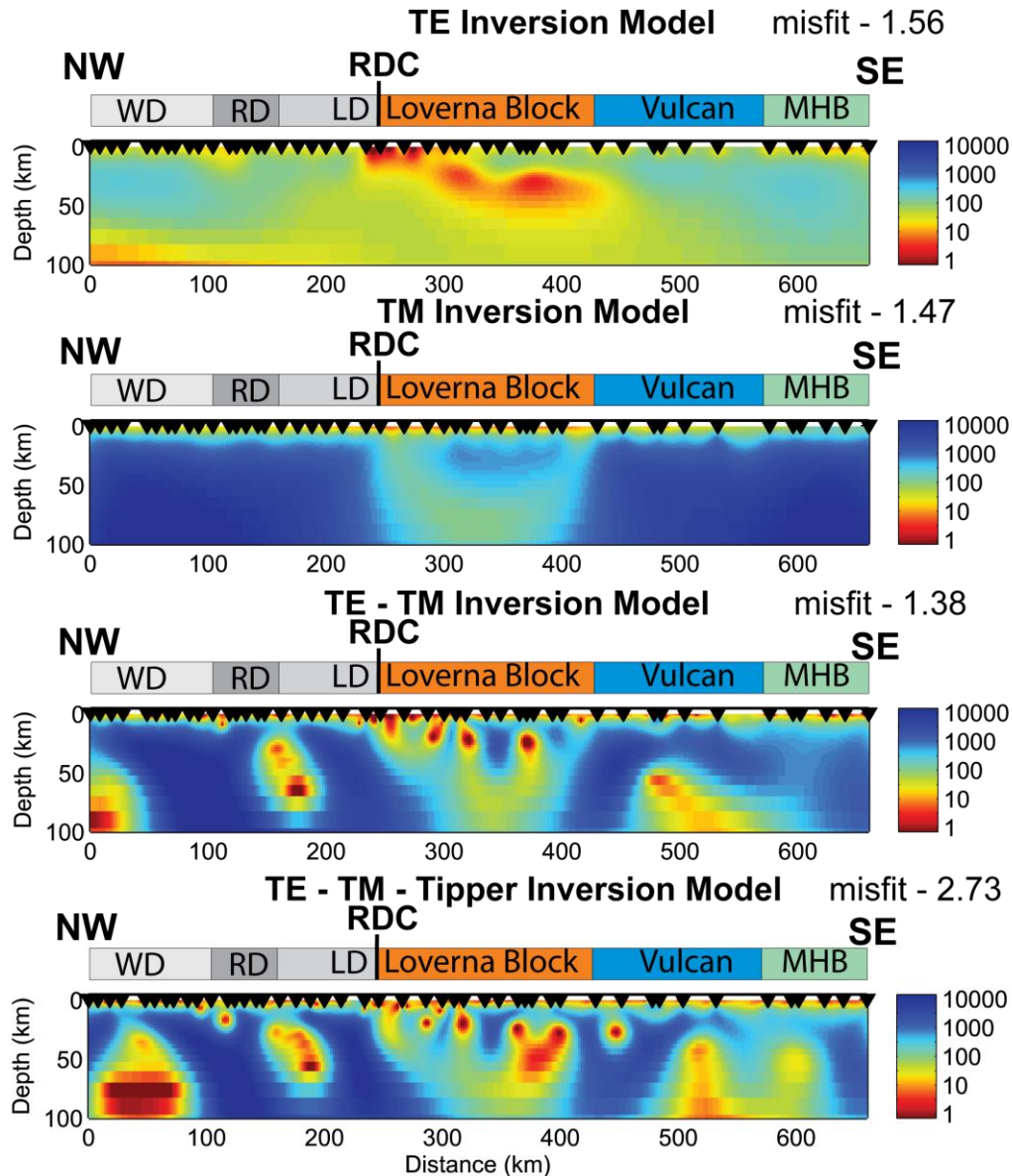
Figure 5.8: Resistivity models generated from the data collected along Line 2. Note that this profile is significantly larger than Line 1, and the scale is therefore much different. WD – Wabuman Domain, RD – Rimbey Domain, LD – Lacombe Domain, MHB – Medicine Hat Block. The Thorsby Low is located between the Rimbey and Wabuman Domain, but is only a few km wide along Line 2.

Compared to Line 1, the TM mode shows more features along Line 2, indicating changes along the profile that coincide spatially with the RDC. The apparent resistivity indicates that the response of the conductive sedimentary basin extends into longer periods to the southeast, and the phase data shows that the TM mode returns to N45°E at 1000 seconds along most of the profile, except for southeast of the RDC where it returns to N45°E near 100 seconds.

The real tipper data in Figure 5.7 shows high values with opposite polarity on both sides of the RDC, again indicative of a large crustal conductor. What is not obviously related to a conductor is that the real tipper data do not appear to change with distance from the RDC. High magnitudes exist at long periods far from the RDC on both sides, terminating at the Vulcan Structure to the southeast, and the end of the profile in the northwest.

The models generated by inversion of these data are shown in Figure 5.8. The TE mode inversion shows a much more continuous dipping conductor than Line 1, coincident with the Loverna Block. A horizontal and conductive region is also present below the terranes northwest of the RDC, at a depth of about 100 km.

The TM mode differs from Line 1 significantly, showing a feature coincident with the
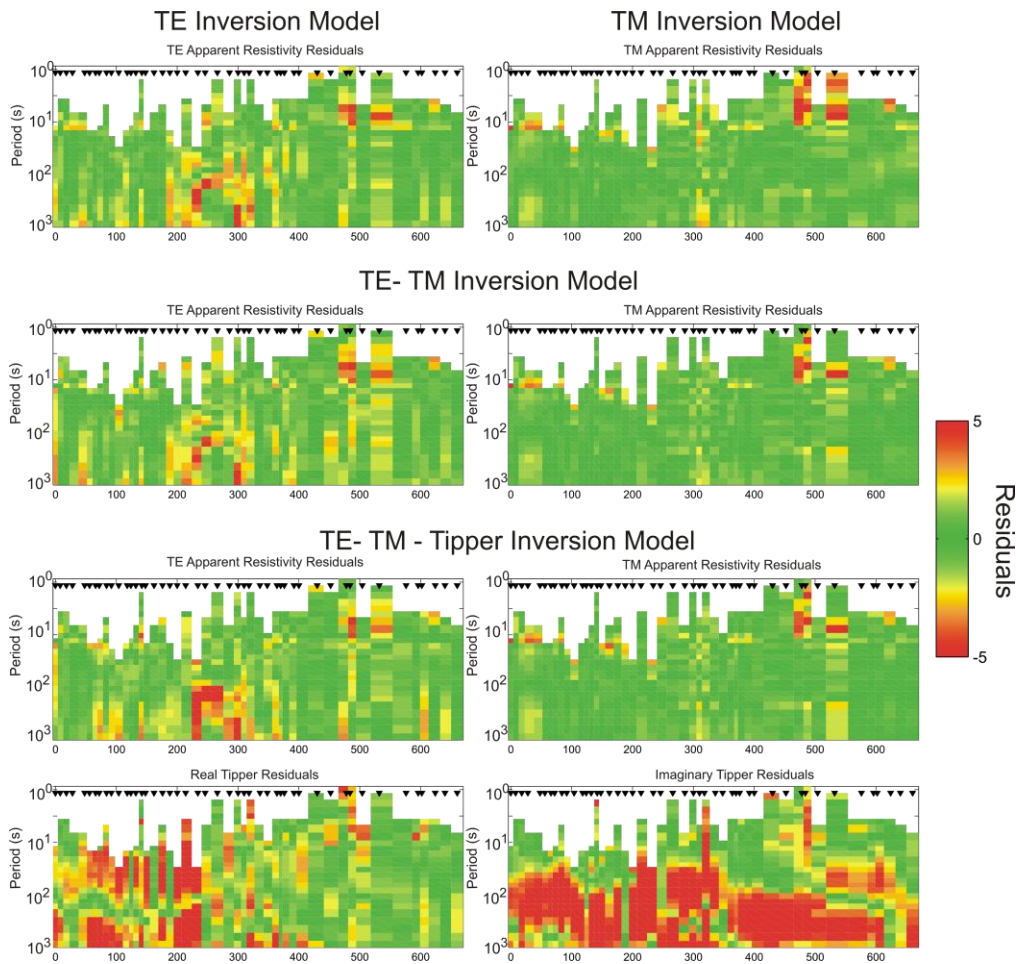
Figure 5.9: Pseudo-sections showing the residuals calculated between the measured data along Line 2, and the data from the inversion models. The top shows the results from the TE and TM models, the middle shows the TE-TM model, and the bottom four sections show the results from the TE-TM-Tipper model. Notice that the TE and TM modes are similarly fit in all of the models.

Loverna Block and the dipping conductor from the TE mode. This feature is much more resistive than the conductor in the TE mode, and its depth is different as well, possibly indicating a separate feature in the upper mantle.

The TE-TM model in Figure 5.8 shows a very complicated and rough model, which fits the measured data with an acceptable r.m.s. misfit, but the discrete conductors located throughout the model do not appear realistic. This is the same situation as Line 1, except that this profile contains more conductors in the TE model that again do not appear in the TM model. The inversion has fit this difference using thin zones of low resistivity throughout the model. These areas are artefacts of an isotropic 2-D inversion of data which is not isotropic and 2-D.

The addition of the tipper data to the inversion did not change the model significantly, but did cause a much larger misfit, similar to Line 1.

5.1.3   Line 3

Line 3 covers much of the same Precambrian terranes as Line 2, stretching 450 km from south-eastern Alberta to central Alberta, with 43 stations spread along the profile.

At a period of 300 s induction vectors in Figure 5.3 show the RDC clearly, where vectors nearby tend to point away from it in the Weise convention, most clearly in the northern stations. In the south these vectors tend to point away from the Vulcan Structure. At a longer period of 2,250 seconds the RDC is less obvious in the data, where induction vectors at the northern stations all tend to point to the northeast. Like the northern induction vectors in Line 2, the northern long period vectors all appear to point away from the Cordillera, possibly sensing the shallow asthenosphere with lower resistivity. The long period induction vectors in the south all point away from the center of the Loverna Block.

Figure 5.4 shows the results from the strike determination using tensor decomposition. The rose diagram shows that nearly all of the stations were best fit by a strike angle near N45°E. The misfit profile in the right side of Figure 5.4 confirms this by showing that a
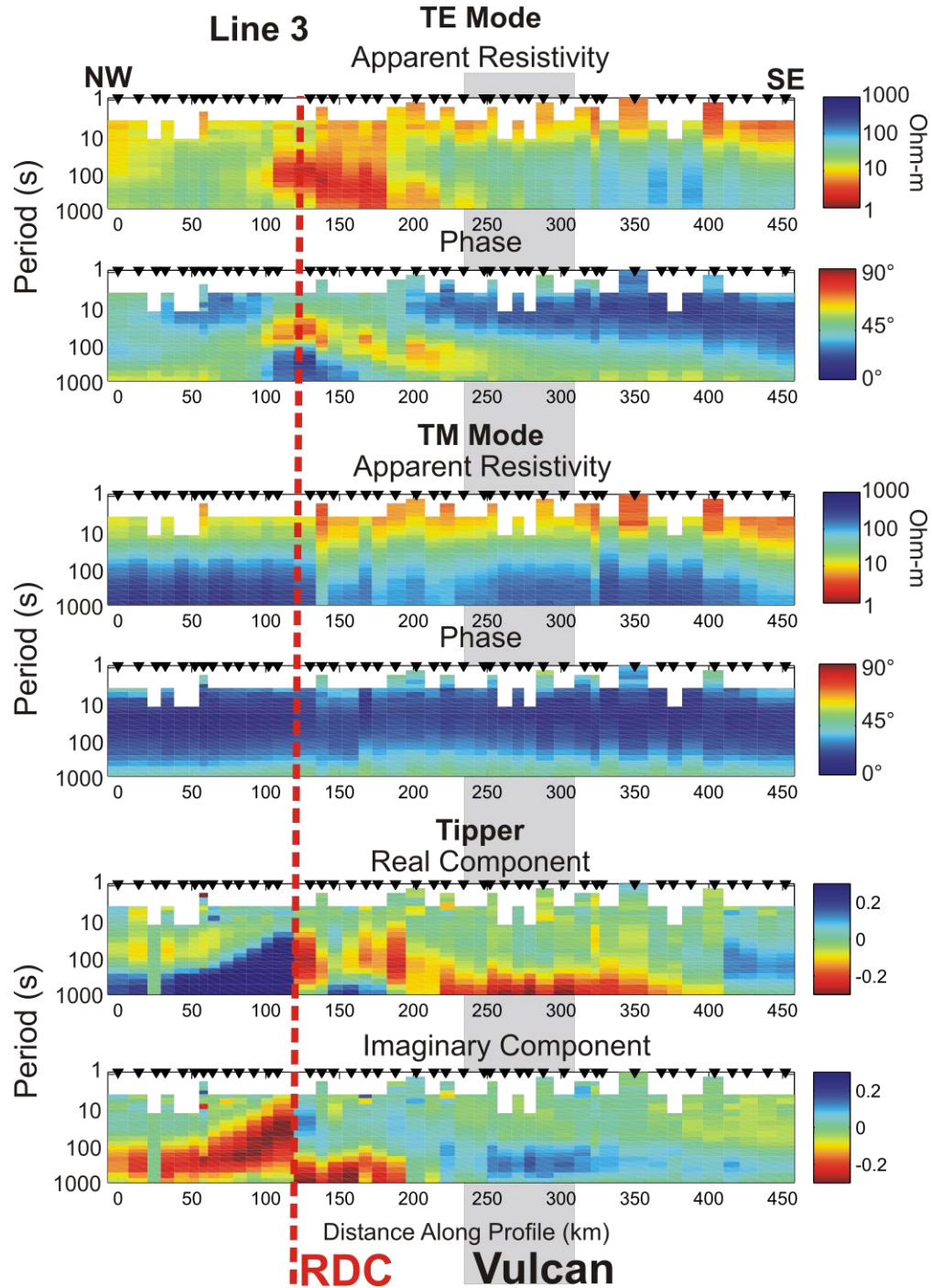
Figure 5.10: The pseudo sections of data collected along Line 3. This profile crosses the same features as Line 2, and shows very similar data to Line 2.
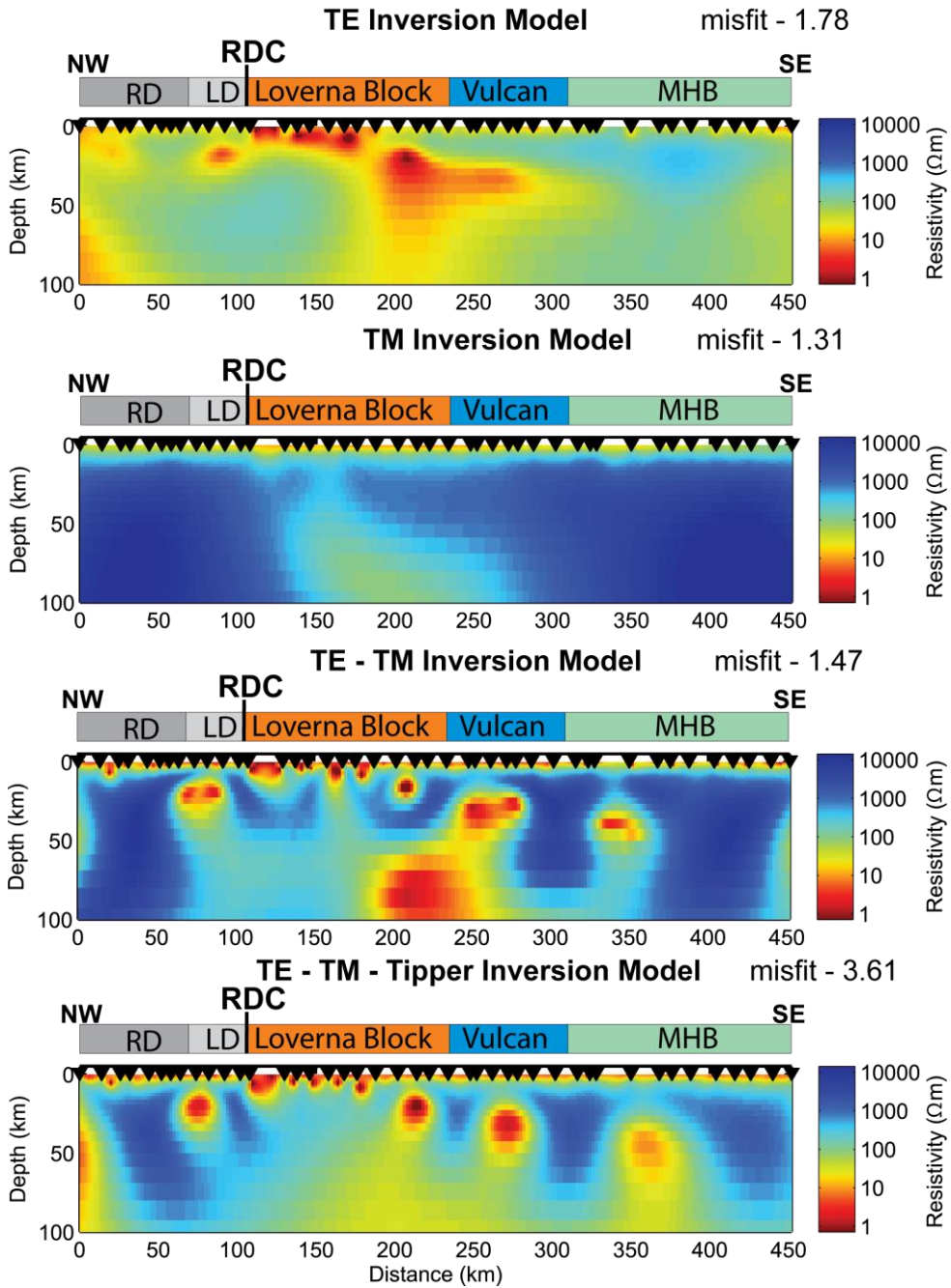
Figure 5.11: Models generated from the inversion of the data along Line 3. Line 3 resulted in very similar models to Line 2. RD – Rimbey Domain, LD – Lacombe Domain, MHB – Medicine Hat Block.

2-D model oriented at N45°E fits the data along the profile with a low misfit.

The data collected along Line 3 is shown in Figure 5.10 as pseudo sections of apparent resistivity, phase, and tipper data. The data show nearly the same features as Line 2, indicating the same dipping conductor in the TE mode (most obvious in the phase angle),

and the TM mode again shows a relatively smooth transition from low apparent resistivity at short periods to high apparent resistivity at long periods.

The inversion models are shown in Figure 5.11, also very similar to the models along Line 2. The dipping and possibly discontinuous conductor in the TE mode terminates at the southern boundary of the Vulcan Structure. The smearing of the conductor into depth is likely an artefact, since the data are probably not sensitive to a conductor located below the dipping conductor. The interesting difference in the TE modes between Lines 1 and 2 is the presence of a conductor which appears to dip northwest from the RDC. Conductors located below the Rimbey Domain in the northwest of the TE model may not be a robust feature of this model, since there are fewer constraints on the model near its edges.

The TM mode shows the same conductive upper mantle region below the Loverna Block as pointed out in Line 2, and the same high resistivities throughout the rest of the profile.

The TE-TM model is less confusing as Line 2, showing a clear discontinuous conductor dipping to the southeast as far as the Medicine Hat Block (MHB). The north-westerly dipping conductor seen in the TE mode occurs in the TE-TM model as a discrete conductor north of the RDC. Below the Vulcan Structure another conductor appears below the southeast dipping conductor. Like the conductors in the TE mode, it is likely that this is not a robust feature of the data.

The addition of the tipper data again caused a worse fit to the data (misfit of 3.61), but the dipping conductor appears clearly as a discontinuous feature reaching as far south as the MHB. The conductor to the north of the RDC is still present, but since the misfit is rather high for this model, it is unclear if this feature or any others are required by the data.

5.1.4   Line 4

Line 4 is only 250 km long, much shorter than Lines 2 or 3, and situated closest to the edge of the Rocky Mountains and Cordilleran deformation. This profile could not be extended further to the northwest because the distortion analysis indicated that the MT data collected near the Rocky Mountains was distorted by structure which cannot be explained by 2-D models (either galvanic distortion or 3-D structure).
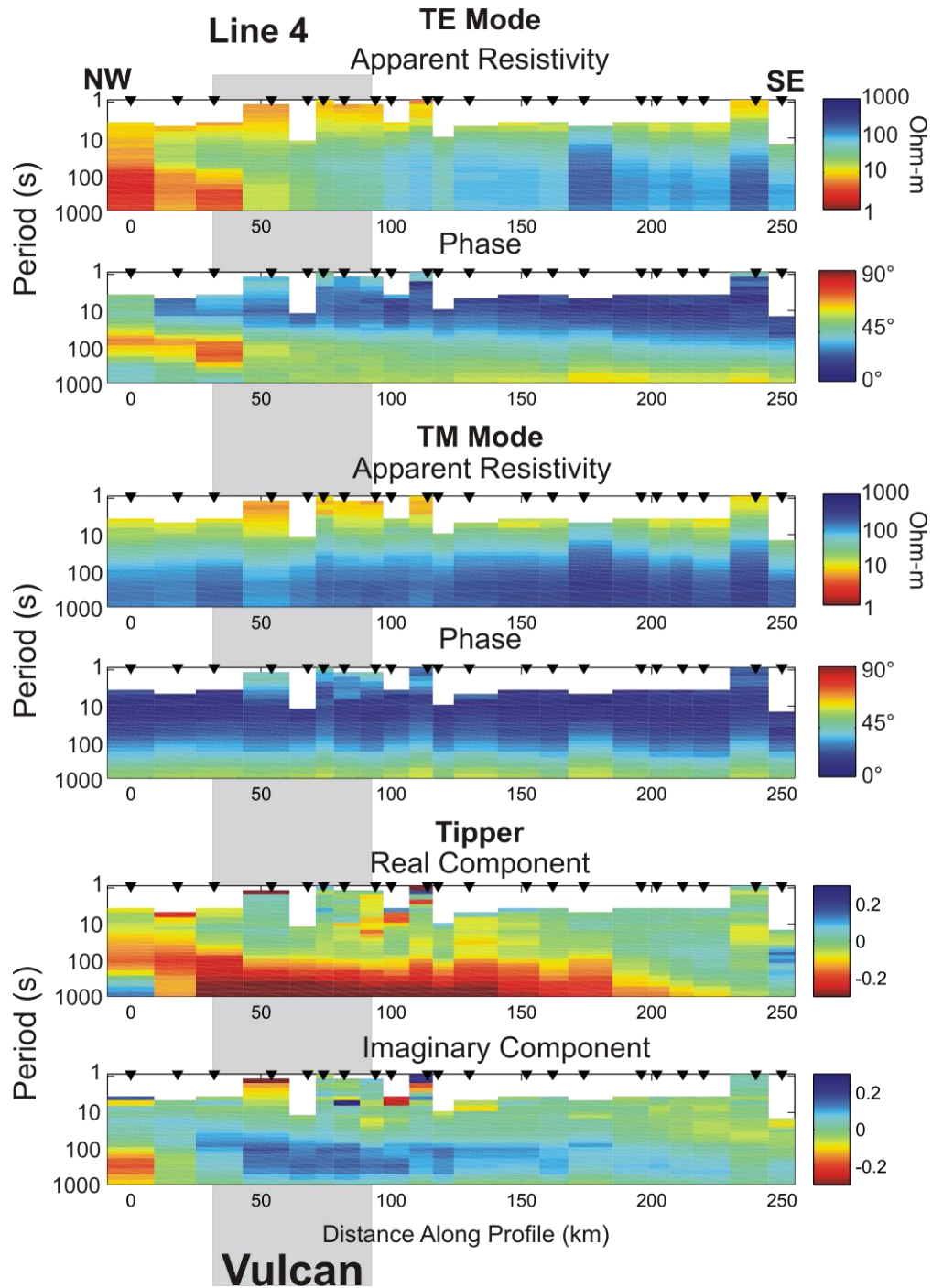
Figure 5.12: Pseudo-sections of the data along Line 4. This profile begins at the edge of the Loverna Block, and ends in the Medicine Hat Block.
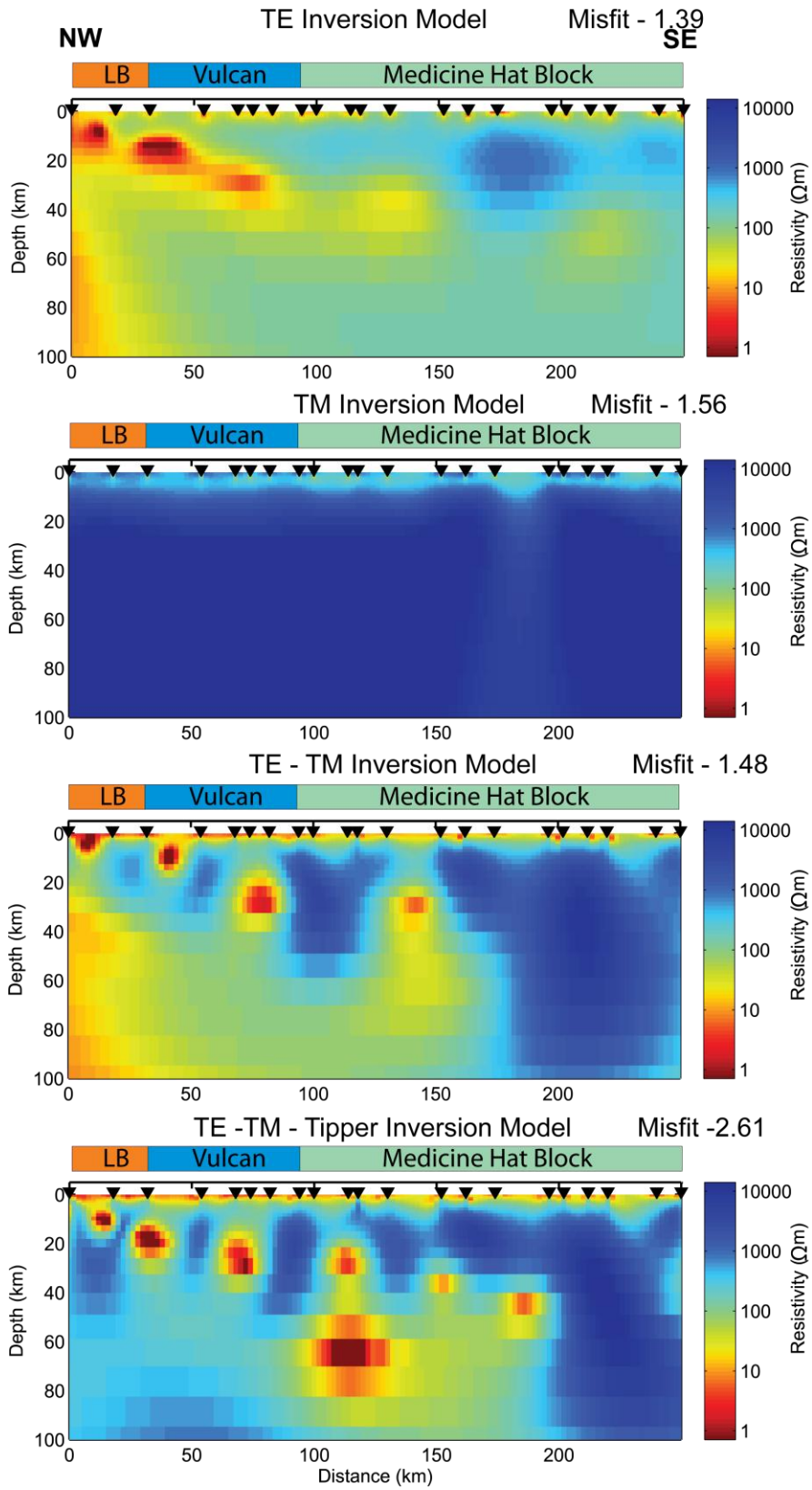
Figure 5.13: Models generated from an inversion of the data along Line 4. Here the discontinuous conductor is present below the Medicine Hat Block.

The strike angles of the stations selected for Line 4 are shown in Figure 5.4, indicating a little more scatter than other profiles, but still showing an average near N45°E. The misfit profile in Figure 5.4 indicates that a strike angle of N45°E is consistent with nearly all of the data and justifying a 2-D analysis in this co-ordinate frame.

Figure 5.3 shows the location of the 21 MT sites along Line 4, with respect to the profile. The induction vectors are all of moderate size, and nearly all of them point perpendicular to the Vulcan Structure. Their size decreases with distance from the Vulcan Structure.

Pseudo-sections of the data along this profile are displayed in Figure 5.12. Because this profile only covers a small portion of the Loverna Block, the region of low resistivity apparent in the TE mode along Lines 2 and 3 is only apparent at the edge of Line 4. This profile again shows that this conductive region ends within the Vulcan Structure, and the TM mode does not sense it.

The real component of the tipper shows the same situation as indicated in Figure 5.3 where the tipper data (also called induction vectors) shows a region of large magnitudes near the Vulcan Structure, and they get smaller with distance from the Vulcan Structure.

The models generated from an inversion of the data are shown in Figure 5.13. Here the TE mode conductor below the Loverna Block shows indication of being discontinuous, and is also present below the crust in the Medicine Hat Block. A conductor is put by the inversion along the northwest side of the model, but it is unlikely that this feature is robust.

Again the TM inversion mode model shows no affects from the TE mode conductor, and is fairly homogenous.

The TE-TM model in Figure 5.13 again shows the dipping conductor as very discrete conductors dipping quite far below the MHB. The addition of the tipper in the last model of Figure 5.13 has made the distinct and conductive blocks smaller, and made more of them, as well as adding a conductor below the dipping ones. The r.m.s misfit has gone up just as in the other three profiles with the addition of the tipper.

5.1.5   Data Misfit

In all four profiles the r.m.s misfit increases significantly with the addition of the tipper data to the inversion. The TE, TM, and TE-TM models all show misfits around 1.5, but

with the tipper this misfit is never lower than 2.6. The models themselves tend to show little structural change between the TE-TM models and the TE-TM-Tipper models, indicating that the tipper is not changing the model significantly; the data are simply not being fit.

This can be illustrated by looking at the residuals calculated from the difference between the measured data and the model data. Figure 5.9 shows the residuals along Line 2, where the residuals are normalized to the data error, therefore a residual of 5 means that the difference between the measured data and the model data is 5 times the data error.

Figure 5.9 shows that the TE and TM modes are both fit equally well in all of the inversion models, but the tipper data are not fit well at all, particularly the imaginary tipper data. Only the apparent resistivity residuals are shown, but the phase residuals indicate the same, as do the residuals at the other three profiles. This means that the high misfit in the TE-TM-Tipper models is mostly due to the inability of the inversion to fit the Tipper data alone.

The inability of a 2-D model to fit the induction vector data is likely due to the directions of the induction vectors, which rarely point along the profile as expected in the 2-D case. This could indicate that a 3-D model is required to explain the data, but this could also indicate electrical anisotropy in the crust, similar to the findings by Brasse et al., (2009) along the west coast of South America.

Regardless of the reason, it is clear that the 2-D modelling of the tipper data are not sufficient, and therefore the 2-D TE-TM-Tipper models will not be considered valid in further analysis.

The fact that the TE and TM modes are fit equally well in the TE-TM model as in the TE and TM models shows that the data justifies all of the models equally. This means that the discontinuity of the dipping conductor in the TE-TM models fits the data just as well as the more continuous conductor in the TE model. But since the TE-TM model is more constrained than just the TE model, it represents the best 2-D model generated in the inversions.

5.2   3-D MT Inversion

A 2-D approach has been widely used in MT inversions over the last 20 years. This is partly due to the availability of stable rapid algorithms such as the one used here. A 2-D inversion is much less computationally intensive than 3-D inversion algorithms which require large amounts of computer time, large amounts of memory, and their behaviour is less well studied. Their large memory requirements mean that only a subset of the MT data collected in southern Alberta can be inverted at one time, and the number of model cells must be limited. This results in relatively coarse models compared to 2-D inversions.

Figure 5.1 shows an outline of the area covered by the final 3-D inversion model. A number of different sized models with different subsets of the MT data were attempted. This section describes the final 3-D model and how it was generated.

5.2.1   The Inversion Algorithm

The 3D inversion algorithm was developed by Siripunvaraporn et al. (2005), and like the 2D inversion used earlier in the chapter, is based on the regularized Occam Inversion (Constable et al. 1987), where the smoothest resistivity model is generated that will fit the measured MT data.

Each iteration of the inversion algorithm first calculates the sensitivity matrix from the previous iteration (or from the starting model in the case of the first iteration). Using this sensitivity matrix the lowest r.m.s misfit is found by varying the Lagrangian multiplier and calculating the resulting model response. Once a misfit minimum is found, the corresponding model is used as the starting point for the next iteration. This method results in at least three sub-iterations per iteration step. Normally convergence was found within 5 full iterations, and when time permitted, the inversion was allowed to continue for up to 10 iterations to ensure the final model was as smooth as possible.

The algorithm searches for the lowest misfit, until a user defined value is reached (the ideal misfit value), or a set number of iterations has been reached. A misfit value of 1.0 was used in this study, representing a misfit average equal to the errors in the data. A misfit value larger than this means that the data is not being fit within the error floor. Once the inversion algorithm has reached this ideal misfit value, it stops trying to lower

the misfit, and enters a smoothing phase. During the smoothing phase the inversion tries to find the smoothest model possible while holding the same misfit.

To start the inversion, the user defines an initial resistivity model and a prior resistivity model. The initial model is used to start the inversion. Unless otherwise stated, the initial model used in this thesis was a 100 Ω-m half space. The prior model is defined as $\boldsymbol{m}_0$ in equation 1.36 of Appendix A, and the inversion is linearized by allowing only small deviations from this model during each iteration step.

The algorithm is controlled through two parameters: (a) the time step (τ), and (b) the length scale (δ). These parameters define the de-correlation scale of the diffusion equation as $\sqrt{4\delta\tau}$ (Siripunvaraporn et al., 2005). According to Siripunvaraporn & Egbert (2000), if the decorrelation scale is too large the inversion may not be able to find a model which fits the data, and if it is too small static shifts may be confused with deep resistivity structure.

The time step has the effect of producing a smoother model, but requires longer run times. The length scale is defined in the x, y, and z directions, and three separate values ranging from 0 to 1 can be set for each direction. The results of changing both of these parameters are presented below.

3-D MT inversions require very large amounts of computer memory, thus the size of model and the amount of MT data which can be inverted is limited. When these 3-D inversions began in 2009, a serial version of the inversion algorithm was used. This meant that only one processor could be used at a time, and one iteration step of a large model could take up to a week. This meant that the inversion used models with a reduced number of cells, and limited data. If the rough subset of data converged to an acceptable misfit, more data and model cells were added, so that convergence of this next larger model would be found with less time. In the fall of 2010 the parallel version of the code was made available, and it became possible to run large models with about 1.5 times more data, over 10 iterations in less than 2 weeks.

In 3-D MT analysis, there are no distinct TE and TM and no strike angle can be defined. Thus the MT data were not rotated from the acquisition co-ordinates and remained in the measurement coordinate system, where x points north and y points east. This algorithm inverted the impedance tensor $\boldsymbol{Z}$ defined in Appendix A, where:

$$\mathbf{Z} = \begin{bmatrix} Z_{xx} & Z_{xy} \\ Z_{yx} & Z_{yy} \end{bmatrix} \tag{1}$$

Each term in the impedance tensor is a complex number computed from the electric and magnetic field measured in the x or y directions as:

$$Z_{ij} = \frac{E_i}{H_j} \tag{2}$$

where i and j represent the directions x and or y, E_i is the electric field in the i direction, and H_j is the magnetic field in the j direction.

The diagonal components of the impedance tensor (Z_{xx} and Z_{yy}) are computed from the electric and magnetic field components measured in the same direction. In the case of a 1-D or 2-D resistivity structure, these components should be near zero, but in a 3-D region they can be non-zero. Therefore the 3-D inversion algorithm inverts for all components of the impedance tensor. These impedance elements are related to apparent resistivity (ρ_{ij}) as

$$\rho_{ij} = \frac{1}{\omega\mu_0} |Z_{ij}|^2 \tag{3}$$

and phase (Φ_{ij})

$$\Phi_{ij} = tan^{-1}[Z_{ij}] \tag{4}$$

where ω is the angular frequency, and μ_0 is the permittivity of free space.

5.2.2   Test Models

Within the 3-D inversion area (Figure 5.1) there are 69 NIMS sites collected for this study and 143 LIMS sites from the Lithoprobe ABT project. A number of different subsets of this data were chosen, with a preference for using NIMS data that has a wider period range than the LIMS data. Sixteen periods were used in the inversion, in the band 1 to 10,000 s.

These first inversion models were all very rough, which was particularly evident in the near surface conductive layer that corresponds to the Western Canada Sedimentary Basin (Figure 5.14) which should be spatially smooth in the horizontal direction. The time step was set to 5 for these rough models, and since a value of 10 allowed the data to be fit similarly, while allowing a smooth sedimentary basin, a time step of 10 was used for the following models.
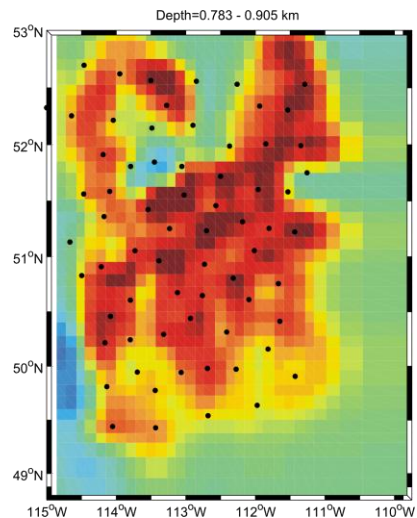
Figure 5.14: A depth slice at 0.7-0.9 km depth, showing the sedimentary basin generated from a model with a time step of 5. The sedimentary basin should appear as a laterally smooth feature but it does not in this model.
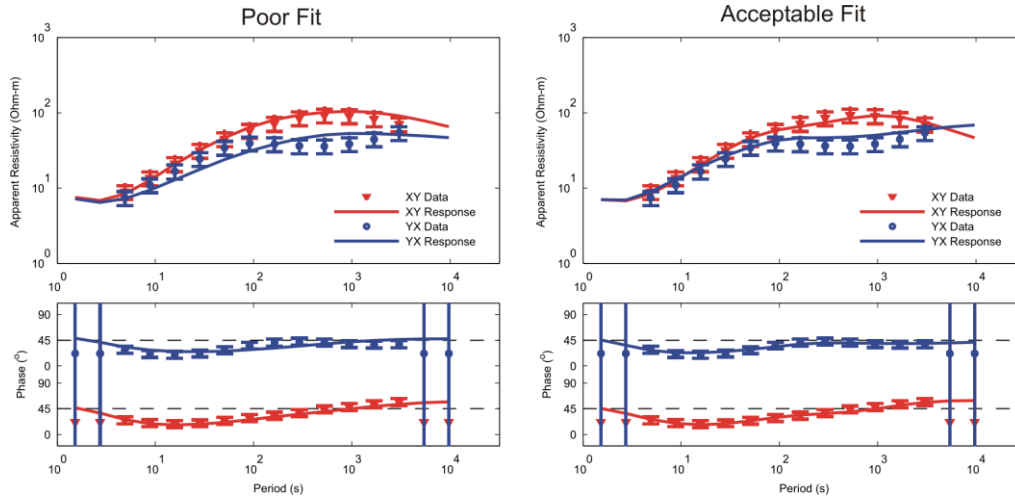
Figure 5.15: The MT data near the Vulcan Structure shows a slight dip in the yx apparent resistivity curve which was not always well fit. The sounding on the left shows a poor fit which characterized many of the initial models. The right sounding shows the response from the final model.

Some of the fine features in the MT data proved difficult to fit, particularly those which had a small misfit penalty when they were not fit. For example, above the Vulcan Structure an obvious dip occurs in the yx apparent resistivity curve between 10-100s as shown in Figure 5.15. The difference in misfit between the two models shown is 0.64, falsely indicating that they both fit the data similarly. This is partially due to a relatively large error floor, which means that a poorly fit model may have a smaller than expected misfit. Many of the initial models did not fit the Vulcan Structure data very well, until the proper parameters were found which allowed the inversion to fit the data much closer.

Another feature which proved difficult for the inversion to fit was a complicated structure near the Foothills. Figure 5.16 shows an example of one model which could not fit the data along the western boundary of the model. In most of the inversions the inversion would converge to a low r.m.s. misfit relatively smoothly, but the inversion model fluctuated significantly from one iteration to the next. Figure 5.16 shows a very large and irregular conductor which the inversion placed in the model but did not fit the data. This model was an inversion of 71 stations spaced somewhat sparsely, and it was determined that the addition of 16 more stations to the grid allowed the inversion to converge smoothly, allowing for realistic structure in the model.

Once it was determined that an inversion of the 87 stations was able to fit the data with a reasonable result, tests were made to investigate the effect of lowering the error floor, changing the length scale, and starting the inversion with an initial model other than 100 Ω-m a half space model.

Three different length scales were tested: 0.2, 0.4, and 0.8. The lowest misfit occurred with a length scale of 0.4, and was the only model which found a misfit low enough to begin the smoothing phase of the inversion algorithm.

Near surface features in resistivity models obtained with a large length scale was smeared to greater depths in the model. Figure 5.17 shows the model with a length scale of 0.8, and although it fits the MT data with an r.m.s. misfit of 1.15, the structure at depth does not seem realistic. The same smearing occurred with a length scale of 0.4, although the values were less extreme.
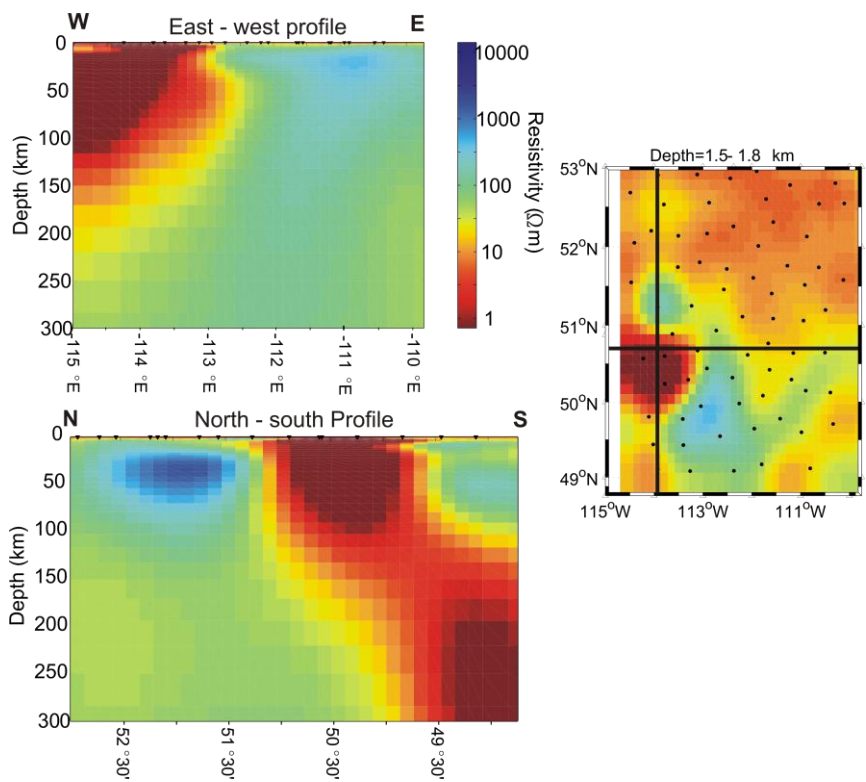
Figure 5.16: This model could not fit the data along the Rocky Mountain foothills. The depth slice on the right shows a slice from within the sedimentary basin. Since the inversion could not fit the data with a realistic model, it has placed an unrealistic conductor in the sedimentary basin. The top left shows an east-west profile through this very large feature with very low resistivity, and the north-south profile shows the extent of this feature. The data was not fit well with this model.

One model with a length scale of 0.4 was run with an initial model containing a 30 Ω-m asthenosphere at a depth of 240 km, and a 100 Ω-m lithosphere above. Introducing structure into the initial model biases the final model towards the initial model, but this test was done to see if introducing an asthenosphere with lower resistivity would stop the smearing of structure into depth while still fitting the data. Figure 5.18 shows a comparison of the initial asthenosphere model with the initial half space model.

Both models show a very similar fit to the measured MT data. The inversion which began from a 100 Ω-m half space model resulted in a final r.m.s. misfit of 1.03, while the inversion that began with a model containing a 100Ω-m lithosphere and a 30 Ω-m asthenosphere had a final r.m.s. misfit of 1.02. The asthenosphere which was placed in the initial model is quite evident in the final inversion model, leaving a discontinuity at depth which is likely not required by the MT data. The positive result of the asthenosphere model is that the resistivity is not unrealistically low, and structure is not as obviously smeared into depth.

Since the initial resistivity of the asthenosphere was 30 Ω-m, compared to 100 Ω-m in the rest of the model, the inversion was able to adequately smooth out the conductor and make it resistive where it is required by the data. The north – south profile in the center of Figure 5.18 shows an area where the inversion has nearly removed the asthenosphere in the south. This shows that the asthenosphere model has not introduced structure which
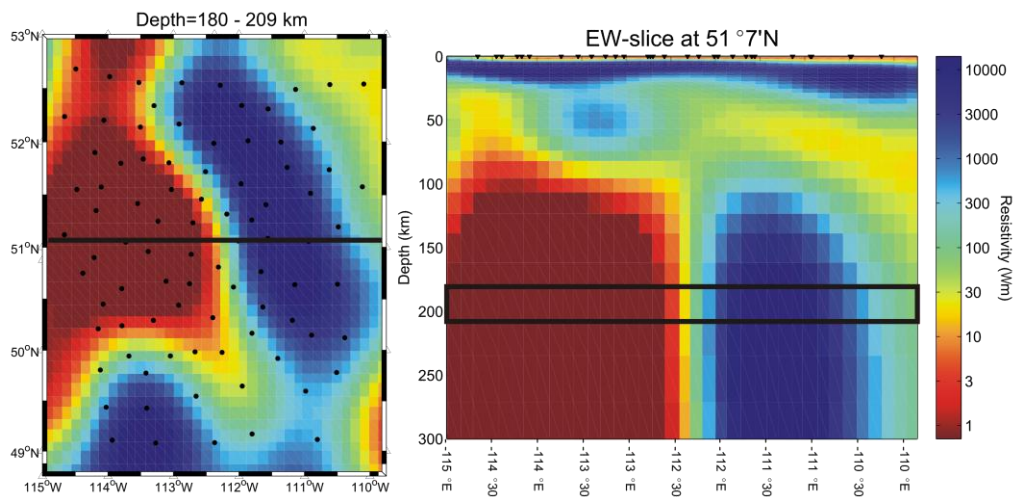
Figure 5.17: A model generated from a length scale of 0.8. The left shows a map of the resistivity at a depth near 200km, and the right shows an east-west oriented profile taken from the model. The black line and box mark the location of each profile and depth slice in relation to one another. With this length scale value the deep structure shows extreme highs and lows, and seems to be smeared into depth.

inhibits the data from being fit, and indicates areas where a conductive asthenosphere is not required by the data.

Early in the inversion attempts it was determined that an error floor of 10% on the off diagonal and 50% on the diagonal elements of the impedance tensor resulted in a smooth convergence of the inversion. The previous models were inverted using this error floor,
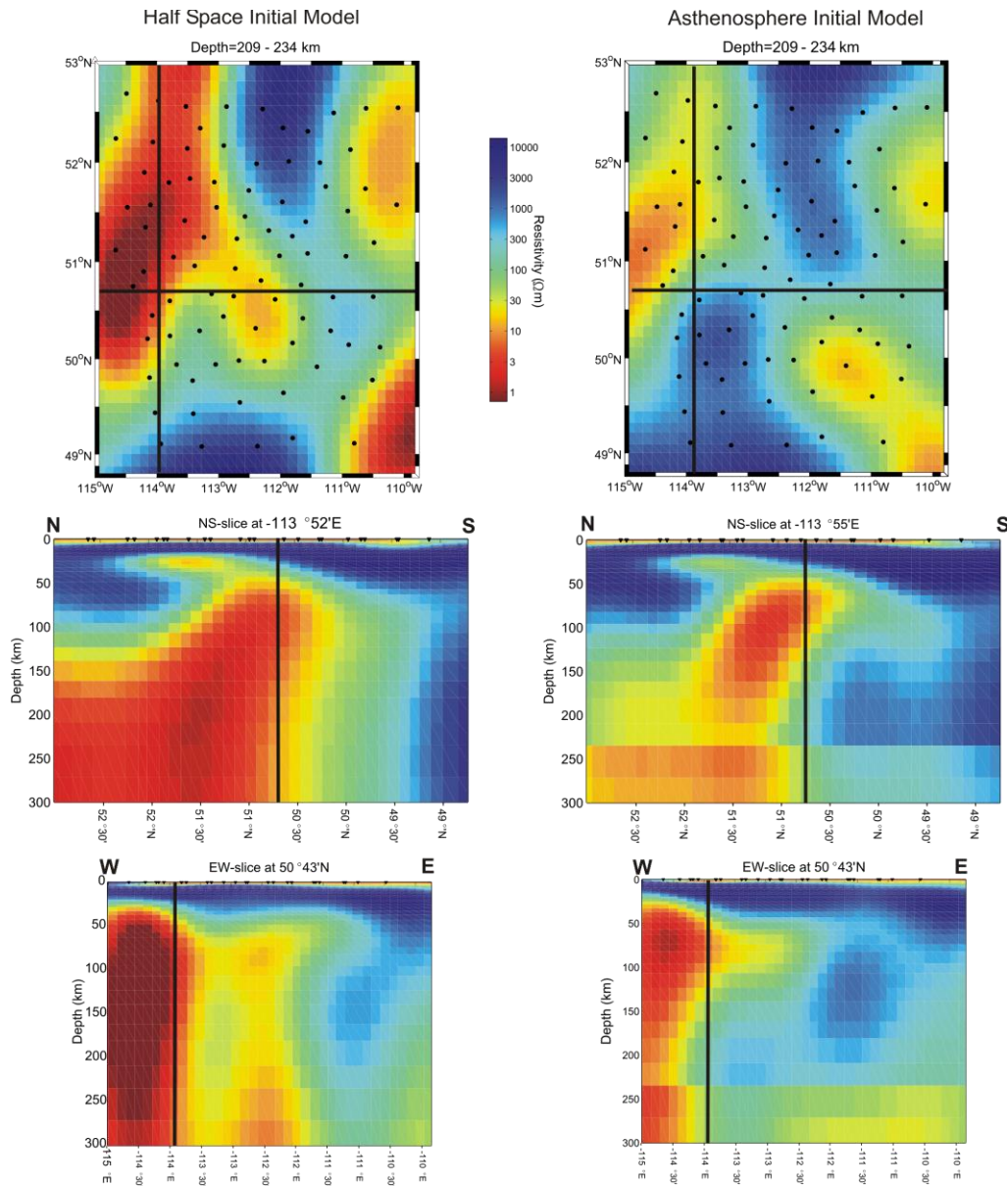
Figure 5.18: A comparison of two models generated with different initial models. The left is with a 100 Ω-m half space initial model, and the right is with a model including a 30 Ω-m asthenosphere at ~240 km depth. The top shows a map from both models of the resistivity at a depth ~215 km. The middle shows north-south profiles from the models, and the bottom shows east-west profiles. The black lines indicate where the slices intersect one another.

and to test this result, one experiment was done using a lower error floor (10% diagonal, 5% off-diagonal) with a length scale of 0.2.

This inversion resulted in a higher misfit value than the previous models, due to the small error floor. Figure 5.19 shows the residuals which are defined as the difference between the observed data and the model data, as a percentage of the observed data. Each of the maps shows the average residuals at each station, where hot colors represent a large residual, and therefore a poor fit to the MT data.
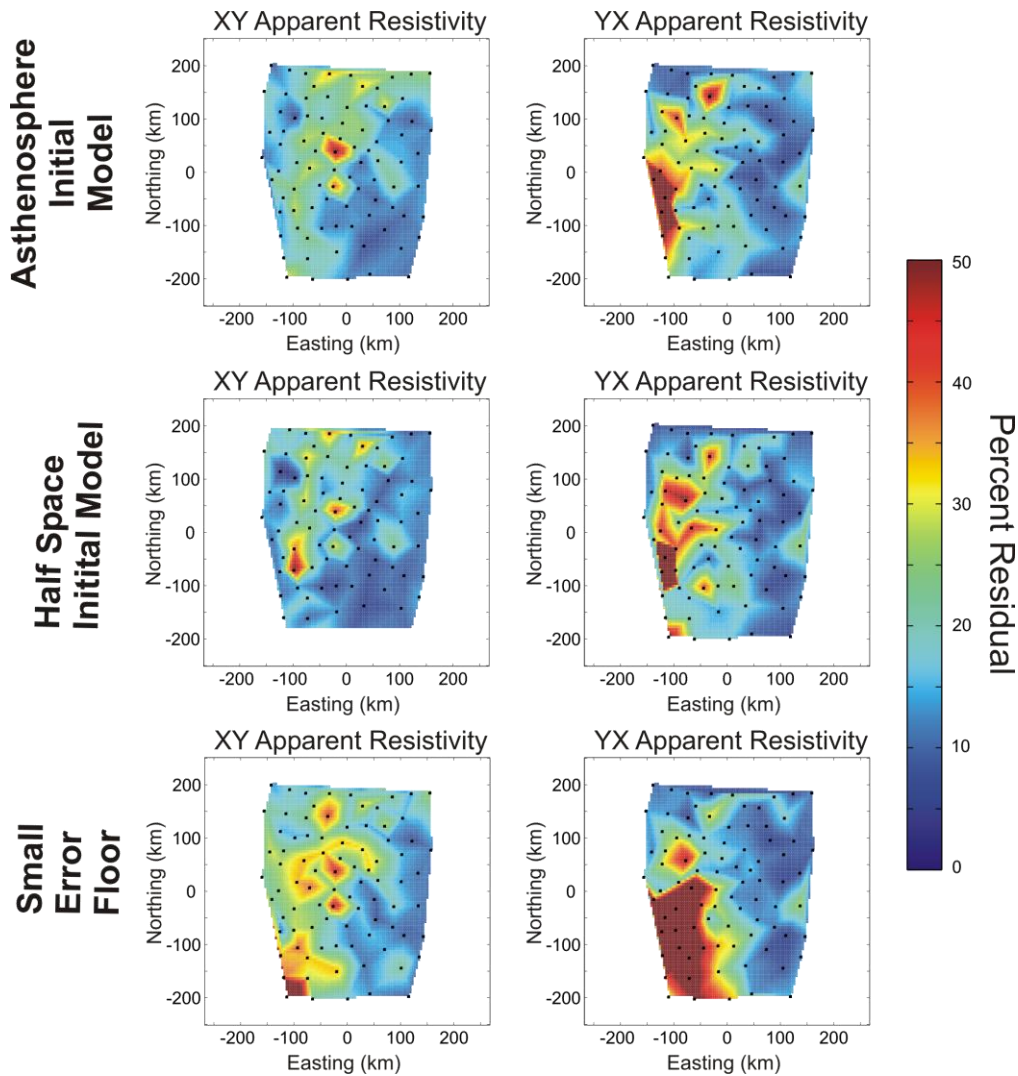
Figure 5.19: Maps of the residual, calculated as the difference between the observed data and model data, displayed as a percentage of the observed data (0.5 is 50%). The top two maps are from the same models as displayed in Figure 5.18, and the bottom map is from a model with a smaller error floor (10% diagonal, and 5% off-diagonal).

Figure 5.20: Examples of the data fit obtained by the 3-D model. The map in the middle indicates where each sounding is located. The small circles are the measured data, and the solid lines are the 3-D model responses.

89
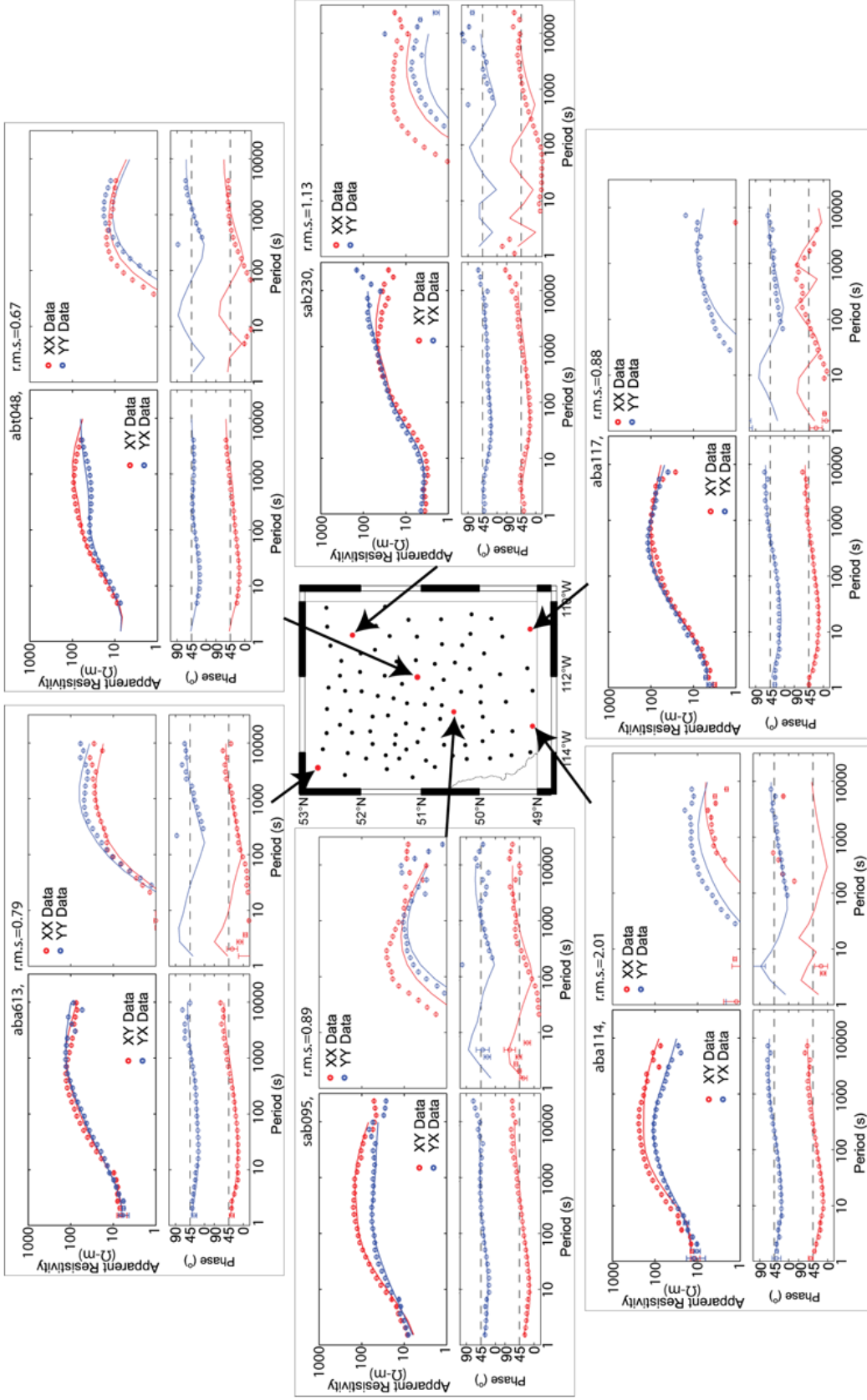
Figure 5.21: Residuals after the data and responses have been rotated to N45°E from the final model.

The top two models in Figure 5.18 both fit the data somewhat similarly, reflecting the fact that they both have a very similar r.m.s misfit, but the small error floor model was not able to fit the data in the southwest very well, particularly the yx apparent resistivity.

Therefore the asthenosphere model and the corresponding 100 Ω-m half space model remain as the two best fitting models. Both models had a length scale of 0.4, and an error floor of 50% on the off-diagonal impedances and 10% on the diagonal impedances. Based on the residuals from each model shown in Figure 5.19 there is no way to choose one model over the other, therefore the final model is chosen based on the more realistic structure in Figure 5.18. The half space initial model shows lower resistivity in the large western conductor, and the structure appears to be smeared into depth compared to the asthenosphere model. Therefore the asthenosphere model is chosen as the best fitting and most realistic model generated from the 3-D inversion of the data grid in southern Alberta.

Examples soundings showing how well the model fits the measured data are shown in Figure 5.20. The xy and yx data tends to be fit better than the *xx* and *yy* data, reflecting the large error floor used for the diagonal impedances.

5.2.3   Comparison of fit between the 2-D and 3-D models

A direct comparison between the 2-D and 3-D models is difficult since the 2-D data were inverted in the strike coordinate frame (N45°E), and the 3-D data were inverted in the geomagnetic coordinate system (N0°E). The 3-D model response can be rotated into the
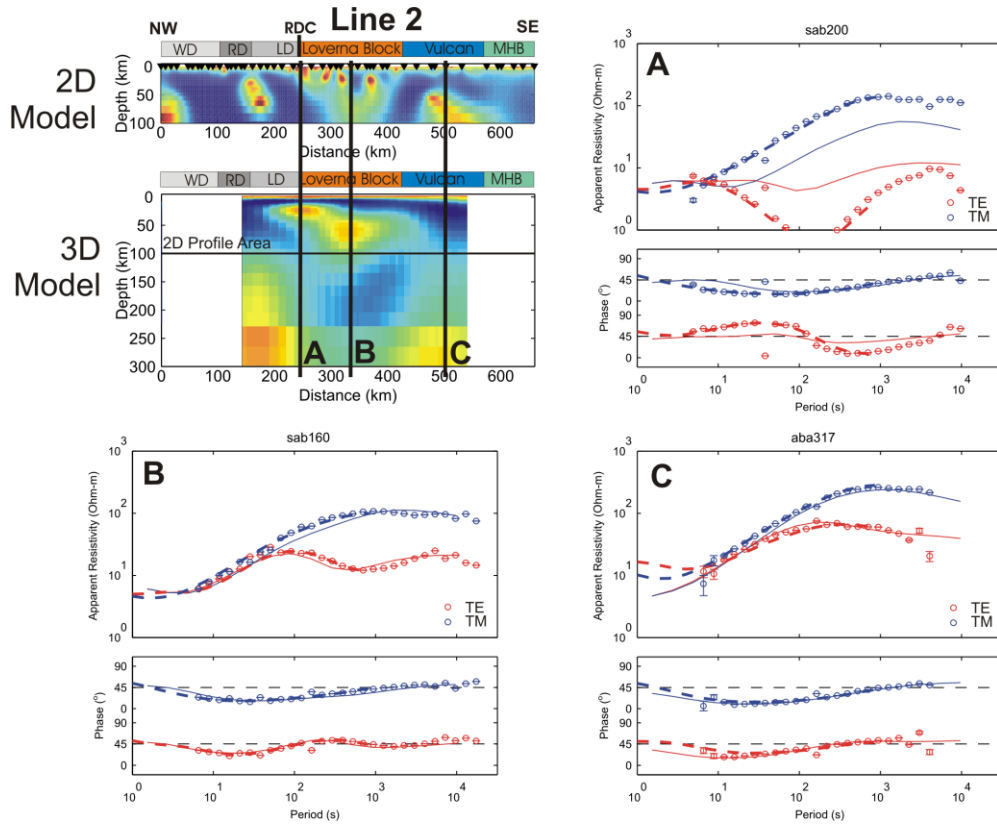
Figure 5.22: Three soundings from along Line 2. The top left shows the 2-D and 3-D models, and each sounding shows a comparison between the measured data (circles), the 2-D model response (dotted lines), and the 3-D model response (solid lines). All the soundings are rotated to N45°E.

strike coordinate frame, but by doing so mixs the *xx* and *yy* responses with the *xy* and *yx* responses. The *xx* and *yy* impedances were down-weighted in the 3-D inversion, and they tend to be noisy to begin with, so they are not fit as well. This means that the 3-D inversion has preferentially fit the *xy* and *yx* data, and rotating the model response will cause the fit to appear worse. For example, Figure 5.21 shows the residuals from the final asthenosphere model after the data and response has been rotated to N45°E.

The residuals in the rotated xy and yx maps are both quite large relative to the unrotated residuals in Figure 5.19. It is quite possible that equal weighting to the diagonal and off-diagonal impedance elements in the 3-D inversion would have allowed the data to be fit regardless of rotation angle. The problem with this is that the diagonal components are much noisier, and if they are not down weighted the inversion will try to fit the noise, probably causing an overall worse fit to the data.

The data directly surrounding the RDC was not fit perfectly by the inversion, which is seen in both the unrotated and rotated residual maps. Regardless, the data to the south and east in the grid has been fit well, giving confidence to the structure around the Vulcan Structure, the eastern portion of the Loverna Block, and the Medicine Hat Block. To illustrate this, the fit along profiles 2 and 3 are compared to the 2-D models in Figure 5.22
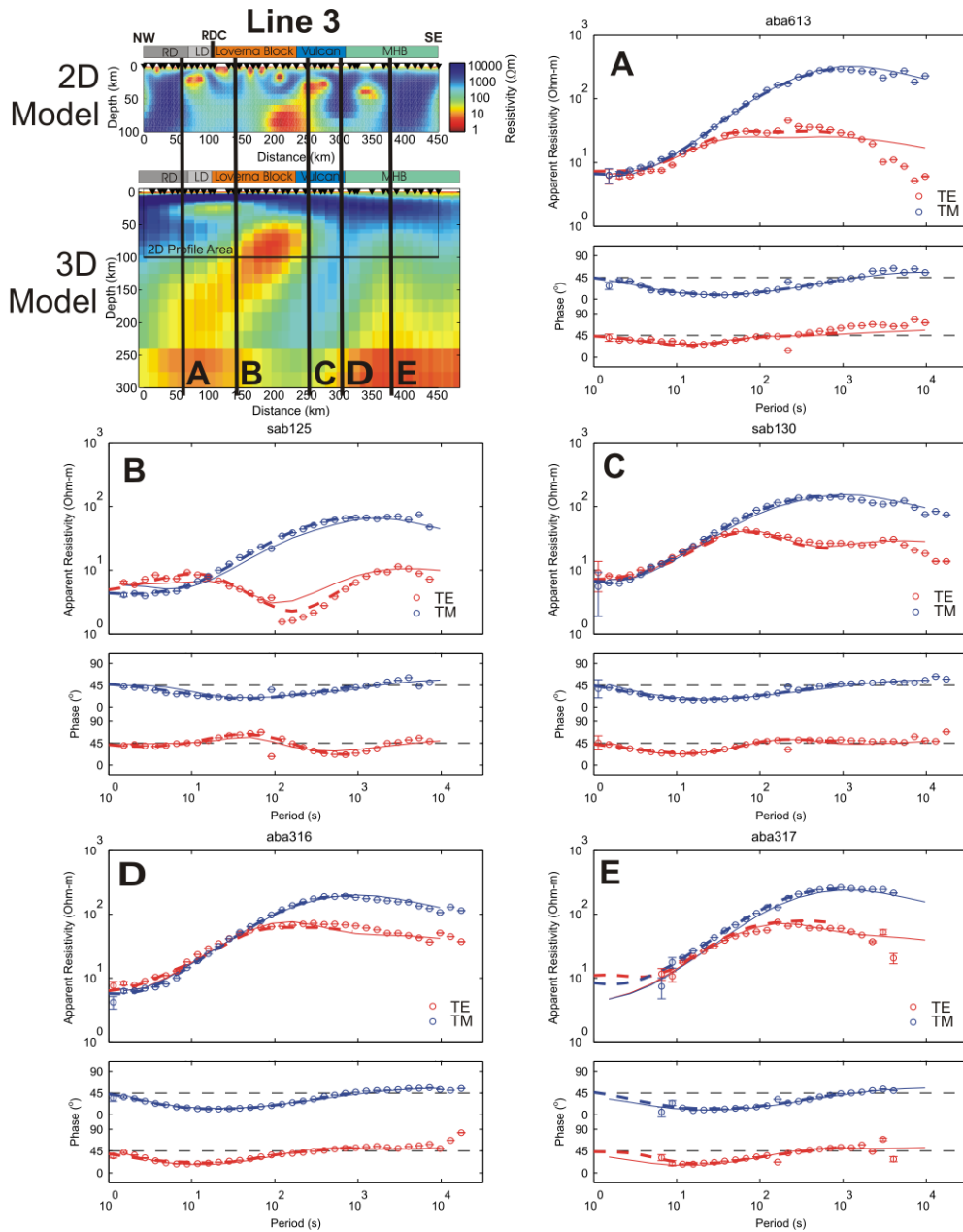
Figure 5.23: A comparison of the 2-D and 3-D data fit along Line 3. The dotted lines show the 2-D model response, the solid lines are the 3-D model response, and the small circles are the measured data.
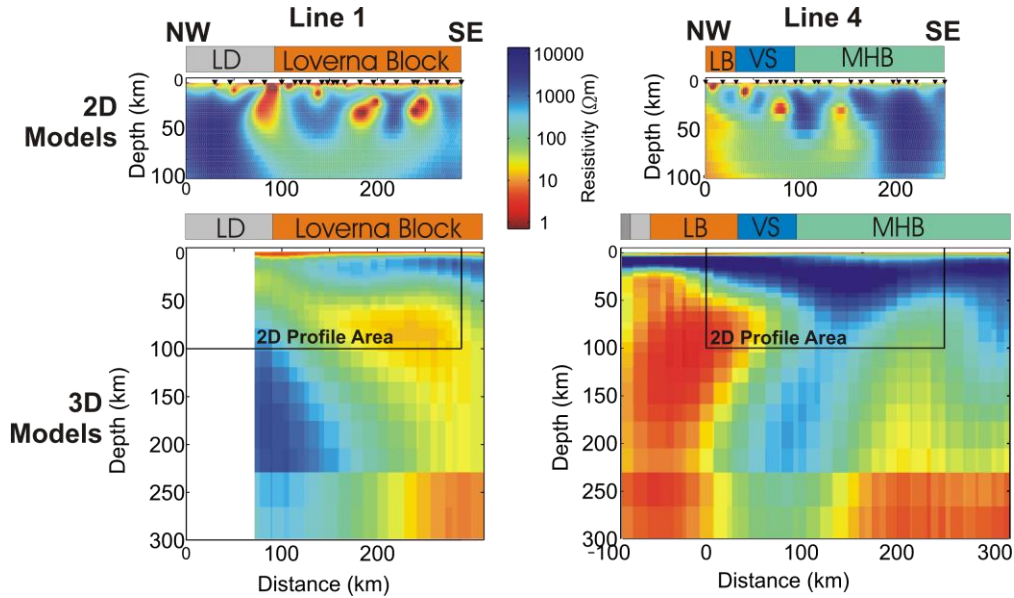
Figure 5.24: 2-D and 3-D inversion model comparisons along Lines 1 and 4.

and Figure 5.23.

Sample soundings in Figure 5.22 are from Line 2, rotated to N45°E, and show the fit of the 3-D model and the 2-D model to the data. In general the 2-D model is able to fit the data quite well, although this requires a relatively rough resistivity model. The 3-D model shows a more realistic resistivity structure, but the fit is not quite as good, particularly at the RDC, where the fit of the 3-D response is significantly worse than the 2-D.

Away from the RDC the data is fit much better by the 3-D model, showing an acceptable fit to the data at most stations. This is again confirmed by the soundings along Line 3 shown in Figure 5.23. These data are fit best by the 2-D model, but they are fit much more realistically by the 3-D model.

Comparisons between the 2-D and 3-D models of the remaining profiles 1 and 4 are shown in Figure 5.24. These comparisons indicate that although the 2-D model fits the data better than the 3-D model overall, the resistivity structure in all of the 2-D models is very erratic. The dipping conductor is discontinuous, which was previously thought to be related to anisotropy by Boerner et al. (2000), but is shown by the 3-D model here that it can also be fit by 3-D resistivity structure which is not necessarily a single dipping conductor. This is confirmed by the fact that the discontinuous conductors change

position depending on which mode is inverted in the 2-D models, indicating that these are likely not actual structures, but instead they are artefacts from the 2-D inversion.

Although the 3-D inversion model could not fit the response of the RDC, it could fit the data to the southeast within the Loverna Block. The 2-D TE inversion model has shown that the dipping conductor exists within the Loverna Block, and the 3-D inversion model fits most of the data in the Loverna Block. Therefore the dipping conductor is fit by the 3-D model without the addition of an unrealistically discontinuous conductor.

In summary, it appears as though the 2-D inversions are able to fit the data better than the 3-D inversions, but they require unrealistic resistivity structures. The 3-D inversion model fits the data acceptably in most places, and its resistivity structure is much more realistic. The inability of the 3-D inversion to fit the response of the RDC is a result of the much coarser grid used in 3-D, as compared to the 2-D inversion, and is also likely associated with the inversion of coordinate system being at an angle to the strike angle of the RDC. The fact that the 3-D model also contains less cells per square kilometre relative to the 2-D model also means that the 3-D inversion is not able to produce a model that is rough enough to represent the subsurface structure. Regardless, the ability of the 3-D model to fit the data, and the realistic structure obtained by the 3-D inversion makes it the preferred resistivity model for southern Alberta.

Since the 3-D inversion could not fit the response of the RDC and surrounding data well, the interpretation in the next chapter will not focus on this area.

Chapter 6

Interpretation

The resistivity model which has been generated from the 2-D and 3-D inversions can now be used to constrain models of the structure of the lithosphere in southern Alberta. This requires an understanding of how the resistivity of these rocks depends on their composition, and this is reviewed briefly in the following paragraphs.

6.1   Resistivity of crustal and upper mantle rocks

Figure 6.1 shows typical resistivities for a range of common rocks. Pure materials found in the Earth have a very wide range of resistivities (less than 10^{-8} Ω-m for metals such as copper, to $8\times10^{-6}\Omega$-m for diamond; Unsworth, 2010). The majority of mineral grains have a very high resistivity because of the absence of charge carriers. Other materials have a very conductive owing to abundant, highly mobile charge carriers. Thus when materials are combined to form a rock, the bulk resistivity of the rock must be calculated by some averaging approach and will be dominated by the conductive material. This occurs even if the conductive material represents a small volume fraction of the whole rock. A number
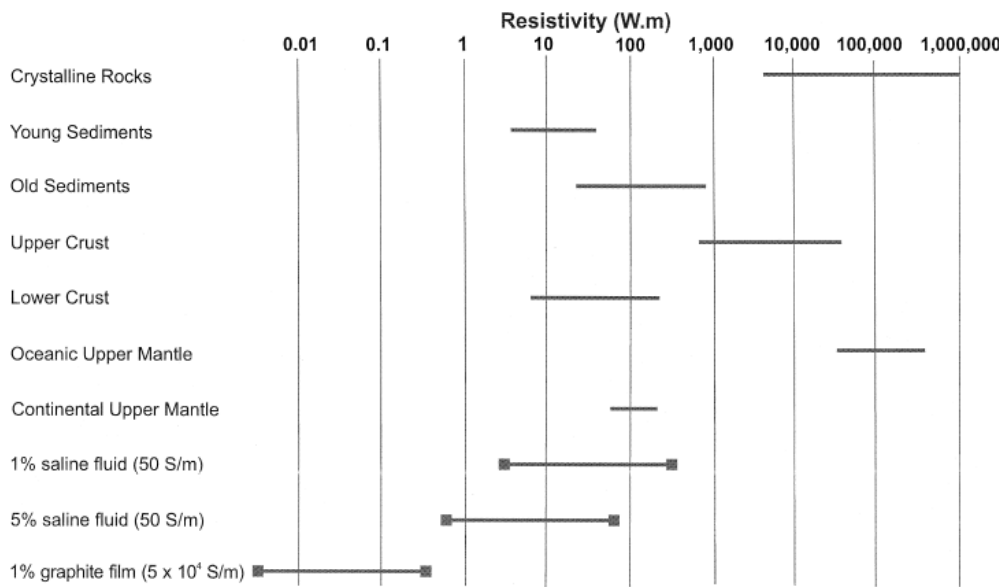
Figure 6.1: From Jones (1999), a table showing typical resistivity values for crustal and upper mantle rocks and fluids.

of conductive materials are found in the Earth.

In the upper crust, saline fluids are widely found in the pore spaces of rock and control the overall resistivity. Since rock grains themselves tend to be quite resistive, the electrical current will flow through interconnected fluids easily. For example, within the sedimentary basin, the primary control on the resistivity will be the porosity and the permeability of the sediments, along with the resistivity of the fluids in the pores (as described by Archie's law; Archie, 1942).

Certain minerals (such as sulphides, graphite etc) can also have a very low resistivity and dominate the overall resistivity of a rock, even if present in very small amounts. This means that conductive anomalies measured by MT can also be explained with minerals along grain boundaries (Jones, 1999).

As depth increases, the concentrations of saline fluids decrease as pore spaces are closed. Therefore anomalies with a low resistivity are more reasonably explained by minerals along grain boundaries such as graphite films (Wannamaker, 2000).

Another minor phase with low resistivity that can control the resistivity of rocks is partial melt. In tectonically active areas, melt can also be a major factor in the resistivity of the lithosphere, but since this is a very old and cold part of the lithosphere, melt is not a likely cause of low resistivity in the crust or upper mantle below southern Alberta. The lithosphere - asthenosphere boundary is marked by the presence of a small amount of partial melt in the asthenosphere, causing an decrease in resistivity below the lithosphere (Eaton et al., 2009).

The top 2-3 km of the crust in southern Alberta have low resistivities (4 - 100 Ω-m), corresponding to the Western Canada Sedimentary Basin (WCSB), and the underlying crystalline rock is quite resistive (~1000 Ω-m). This value is typical for the upper crust on a global scale, where the top 10-15 km commonly shows values on the order of 10^3 to 10^5 Ω-m. The lower crust tends to be much less resistive, with values in the range $1 - 50$ Ω-m (Gough 1986; Hyndman & Shearer 1989; also see Figure 6.1). Anomalies within the upper crust have been explained on the basis of former suture zones, for example the RDC, and the North American Central Plains Conductor in the Trans Hudson Orogen (Boerner et al., 1996).

The origin of the lowered resistivity observed in the lower crust has not been resolved (e.g. Yardley & Valley 1997), although in regions which have been stable since the Mesozoic, the brittle - ductile transition zone may have approached the bottom of the crust (Wannamaker, 2000), meaning that the lower crust below southern Alberta is possibly brittle, and porosity may be created through brittle deformation. In order for saline fluids to cause low resistivity, the pore space has to be connected, but if it is connected then the fluids will escape to the surface, resulting in a dry and resistive lower crust. Therefore, in order for fluids to cause low resistivity in the lower crust, that part of the crust must be brittle, contain sufficient pore space which is connected, but an impermeable cap must exist above the fluids, preventing them from escaping to the surface (Bailey et al., 1989). Some authors have suggested that the brittle ductile transition zone itself may act as an impermeable cap which holds the fluids down (e.g. Gough, 1986b), although this means that saline fluids need to exist in ductile rheology within the lower crust, which might not be possible due to petrological problems with this model (Yardley & Valley 1997).

According to Wannamaker (2000), low resistivity in the deep crust below a stable region (stable since the Proterozoic) is more likely related to graphitic grain boundary conduction as opposed to saline fluids. The graphite could have been emplaced through the subduction of organic matter (carbon), which is then regionally dispersed through metasomatism during the late stages of subduction. After the graphite has been emplaced, porosity may close up and leave thin films of graphite throughout the rock mass (Wannamaker, 2000). This is an attractive interpretation for cases where very low resistivities (2-3 orders of magnitude less resistive than expected crystalline rocks) exist at depths above ~160 km. Below this depth, carbon will not exist as graphite but will instead form diamonds (Jones & Craven 2004).

At temperatures and pressures associated with the upper mantle, olivine is quite resistive (Xu et al., 2000), but many MT studies have found that the resistivity of the upper mantle is 2 – 3 orders of magnitude lower than expected for an olivine dominated mantle (Jones & Craven 2004). Grain boundary conduction mechanisms are the most likely explanation for these lower than normal resistivity. For example, Jones & Craven (2004) interpret a zone of low resistivity in the upper mantle below the Slave craton as graphite films along grain boundaries.

Our resistivity model of southern Alberta constrains the electrical structure of the lithosphere, which in turn constrains its geological structure. This chapter will present the preferred resistivity model and discuss tectonic implications.

6.2   Model Observations

The model derived in Chapter 5 shows 5 main resistivity features:

1) A conductive surface layer (5-10 Ω-m) 1.5 - 2 km thick, with resistivity that is identified as the WCSB.

2) Along the western edge of the modelled area the resistivity structure of nearly all the inversion models shows a linear conductive zone which follows the western edge of the sedimentary basin (see Figure 6.2).

3) Low resistivity within the upper mantle beneath the Loverna Block, here named the Loverna conductor (see Figure 6.3).

4) The Lithosphere – Asthenosphere Boundary (LAB) appears as a zone of low resistivity at a depth of 250 km, although the complicated resistivity structure near the crust makes it difficult to map this feature throughout the model.

5) The Red Deer Conductor (RDC) within the crust, at the base of the WCSB, although since this model cannot fit the data surrounding the RDC
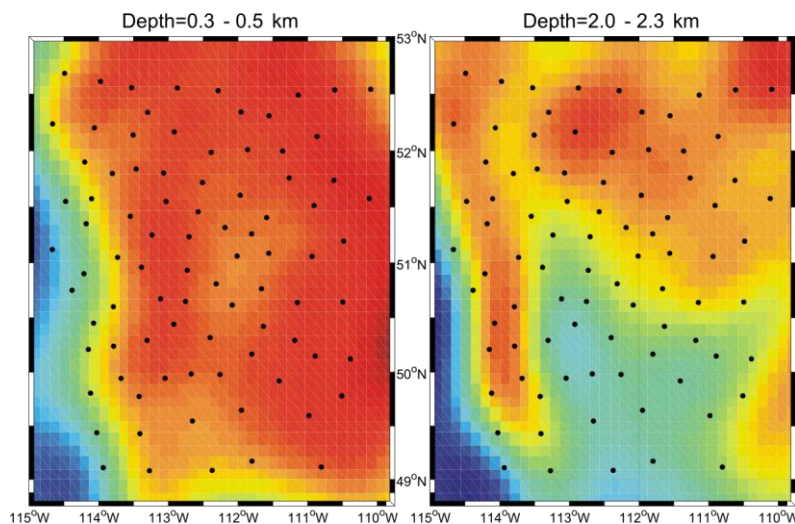
Figure 6.2: Left: the western edge of the sedimentary basin constitutes a sharp boundary between sediments with low resistivity and resistive material in the Rocky Mountains. Right: the sedimentary basin is deepened along a thin north-south trend, marking the boundary between the sedimentary basin and the Rocky Mountains.

adequately, this feature will not be discussed in detail.

Figure 6.3 shows five transects taken from the 3-D model, oriented perpendicular to strike, where lines 1 through 4 correspond to the locations of the 2-D profiles. As a whole these profiles show a very resistive crust, as we would expect with crystalline Precambrian rocks. The RDC occurs as a conductive zone around 25 kilometres deep in the crust, which is deeper than previously thought (see Lines 2 or 3). It is most likely that the RDC is not this deep, since there is little confidence in the model surrounding the RDC (as discussed in the previous chapter).

Every profile shows the existence of a large conductor which occurs in the upper mantle beneath the Loverna Block. This conductor merges with the RDC in places, particularly along the western edge of the grid, although their relationship is not well defined by this model owing to the poor data fit along the RDC. This conductor will be discussed in more detail below.

The LAB is difficult to define in this model, partially because the model is biased by the discontinuity placed in the initial model, and partially because the low resistivity structures in the crust and upper mantle attenuate much of the MT signal before it reaches the LAB. Based on previous MT studies in northern Alberta, we expect that the LAB exists near depths of 200 – 250 km, but conductive regions at that depth in the model can be attributed to smearing of conductors within the upper mantle, or simply a lack of data sensitivity at that depth, so that the structure from the initial model has not been changed.
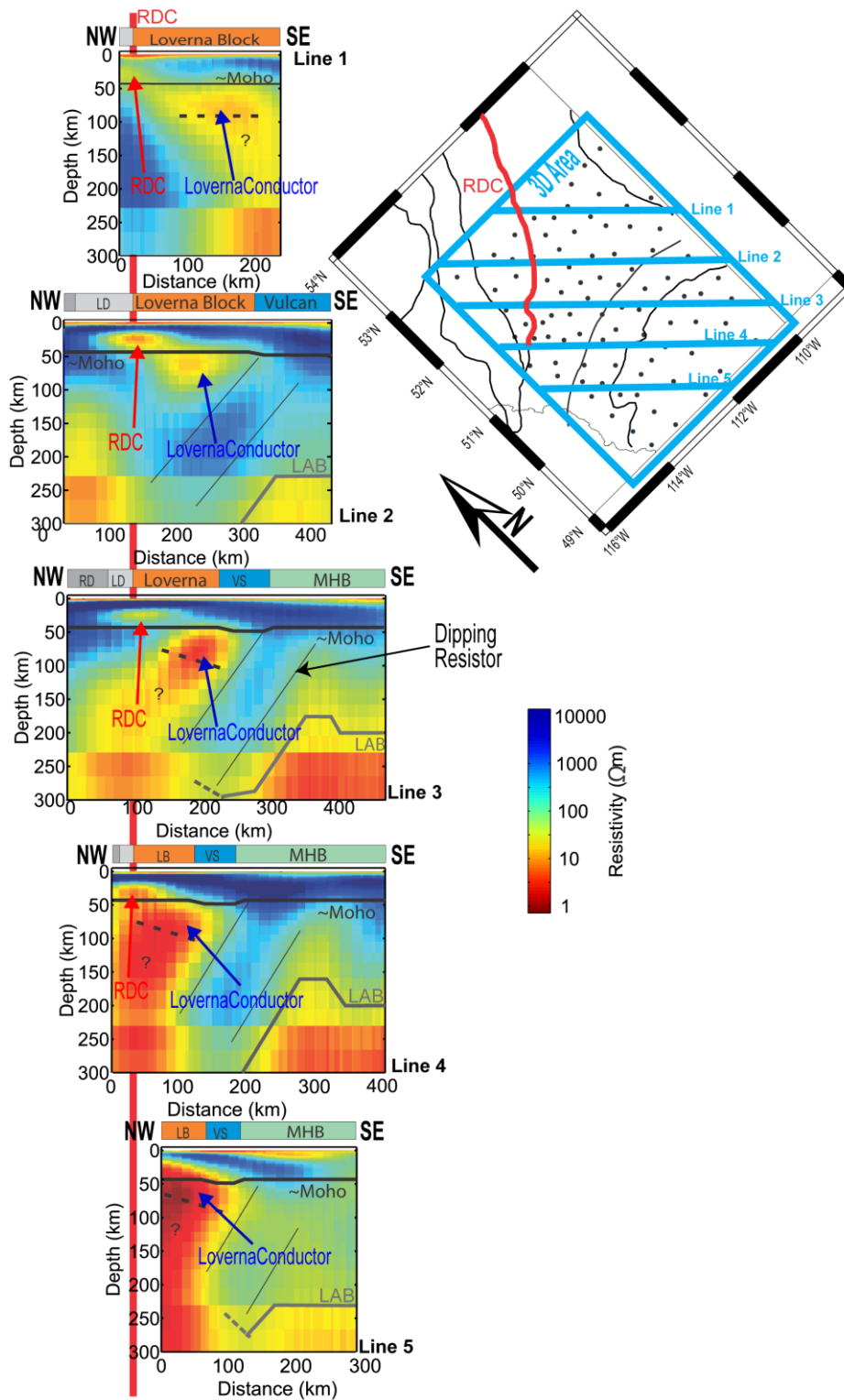
Figure 6.3: Profiles extracted from the 3-D model oriented across strike. The red line represents the location of the Red Deer Conductor, where each profile has been lined up along it. The Moho boundary is approximate, and based on reflection seismic (Bouzidi et al., 2002). Areas marked with a question mark below dotted lines represent areas with little confidence, the LAB is defined based on the model, and the thin dipping lines indicate the dipping resistor discussed in the text.

6.2.1   Linear Foothills Anomaly

Figure 6.2 shows that within the upper 1 km of the model, there is a definitive boundary between the highly resistive Rocky Mountains and the low resistivities in the sedimentary basin. At the bottom of the sedimentary basin, a linear conductor follows this boundary. This conductor appears as a thickening of the sedimentary basin along a narrow corridor coincident with the edge of the sedimentary basin.

Because it appears attached to the sedimentary basin in the model, one possible explanation could be the deepening of the basin along a thin corridor, although such a deepening of the basin has not been measured in drill holes along the Rocky Mountains (see Pilkington et al., 2000). Another more likely explanation would be fractures along the top of the Precambrian basement caused by thrusting of the Rocky Mountains terrane over the basement. Consequential filling of the fracture zone by saline fluids could easily explain the low resistivity.

6.2.2   Loverna Conductor

In Line 3 of Figure 6.3 the Loverna conductor appears to dip into the upper mantle to the northwest, and merges with the RDC along the western edge of the grid. Where it merges in profiles 4 and 5 The Loverna conductor appears as a very large zone of low resistivity throughout the lithosphere and into the asthenosphere. It is known that the low resistivities in the asthenosphere occur at shallow depths beneath the Cordilleran terranes to the west, and it is likely that this western zone of low resistivity is in part associated with the shallow asthenosphere to the west.

Because the western edge of the model is another place where the residuals in the previous chapter showed a poor fit to the measured MT data, and the edge of the data grid is also a place which is less constrained than the center, the western edge of this conductor is less well constrained in the model than the eastern portion.

The five profiles in Figure 6.4 show that the Loverna conductor changes laterally, and never occurs south of the Vulcan Structure.

The Moho in the study area is approximately 45 km deep (Bouzidi et al., 2002), and the only low resistivity anomaly which occurs above this is associated with the RDC. Below a depth of ~40 km the resistivity of the entire Loverna Block changes from ~1000 Ω-m in the upper crust, to less than 100 Ω-m in the upper mantle. At depths near 50-60 km the low resistivities become concentrated in some areas throughout the Loverna Block, showing resistivity values closer to 10 Ω-m.

The southern boundary of the Vulcan Structure remains very resistive at all depths and the profiles in Figure 6.3 show that a zone of high resistivity is correlated with the Vulcan Structure, dipping northwest into the asthenosphere. This resistor occurs in all of the profiles except Line 1 which does not cross the Vulcan Structure, and Line 5 shows it as much less resistive, although this profile is somewhat near the edge of the grid and is less constrained because of it.

This dipping resistor must be viewed with some caution, because the Loverna conductor
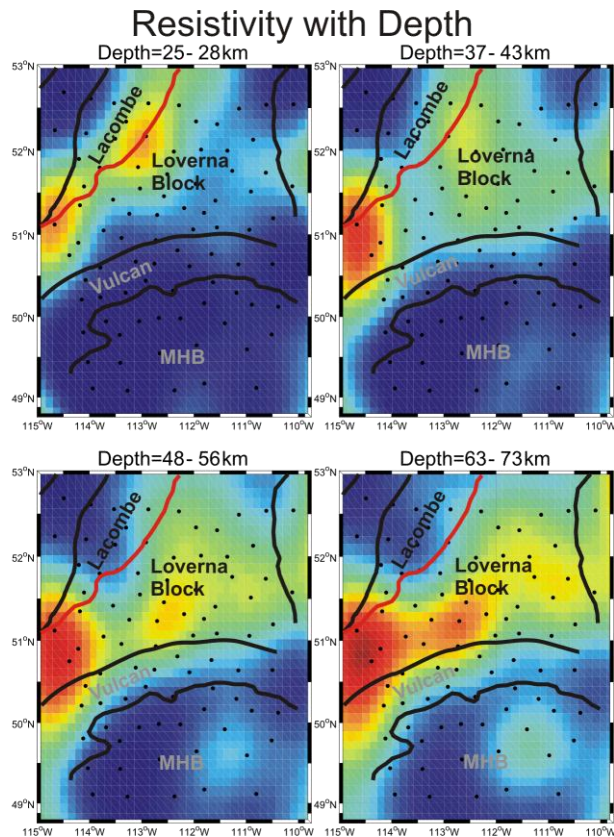
Figure 6.4: Depth slices from the resistivity model, the RDC is marked by the red line, and the black lines represent the Precambrian domain boundaries. The conductor within the Loverna Block never occurs south of the Vulcan Structure, or north of the RDC.

which lies above probably makes the MT data much less sensitive to it, and it is not absolutely clear that this resistor is required by the MT data.

A comparison with the seismic reflectors described by Gorman et al. (2002) in Figure 6.5 show that the top of the Loverna Conductor coincides very closely with one of the two reflectors in their seismic refraction profile. The second reflector coincides very closely to the low resistivity zone south of the Vulcan Structure within the MHB. The top of this conductor can be seen in the bottom right depth slice of Figure 6.4.

The second southerly conductor within the MHB (Figure 6.4) was originally interpreted as a piece of dipping crust associated with north dipping subduction at the Great Falls Tectonic Zone to the south (Gorman et al., 2002).

In summary, the Loverna conductor is regionally pervasive throughout the upper mantle below the Loverna Block. It is sharply cut off along the Vulcan Structure, where a dipping resistor (which must be viewed with some caution) appears to truncate the Loverna conductor to the south. To the north, the conductor may be associated with the RDC, although this is not conclusively shown by this model. The Loverna conductor is associated with a north dipping reflector, and another conductor which occurs below the MHB with a similar reflector bounding it along the top.
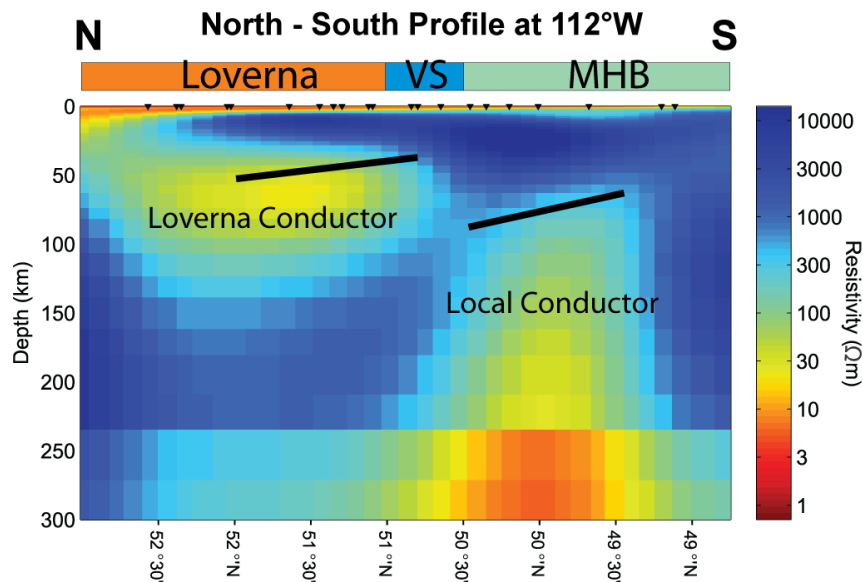
Figure 6.5: A north – south profile taken from the resistivity model at 112°W. The dark black lines represent the locations of two north dipping reflectors discovered by Gorman et al. (2002) in their refraction seismic line crossing southern Alberta (known as Deep Probe).

6.2.3   Lithosphere Asthenosphere Boundary (LAB)

The LAB is commonly seen worldwide as a decrease in resistivity from hundreds of Ω-m's to < 25 Ω-m (Eaton et al., 2009). The profiles in Figure 6.3 show this change from resistive lithosphere to conductive asthenosphere in the depth range 175 to 240 km.

Because the data in the northwest of the grid was not fit well, the LAB cannot be defined in this part of the model, and because MT data is not sensitive to structure below a large conductor, the LAB below the Loverna conductor is also not well defined. The MHB is one place in the model where the LAB is well defined.

The gray lines in Figure 6.3 mark the interpreted LAB based on the change in resistivity at a depth near 200 km. There is a significant amount of change, particularly southeast of the dipping resistor, where the LAB appears to shallow significantly. Because this upwelling of the LAB is coincident with the MHB reflector/conductor noted in the previous section, it is possible that the reflector marks a discrete upper mantle conductor, below which the MT data lacks sensitivity. In this case, the upwelling of the LAB may be an artefact of the inversion, and cannot be trusted.

The north dipping resistor coincident with the Vulcan Structure has pushed the LAB to depths greater than 250 km, which seems to be a robust feature of the model, since it occurs coherently along the entire Vulcan Structure.

The furthest south portion of the grid all show that the LAB is relatively flat lying below the MHB, showing depths between 200 and 240 km.

6.2.4   The Vulcan Structure

Early interpretations of potential field data over the Vulcan Structure assumed that a regional magnetic high located to the north of the Vulcan Structure was related to volcanic terranes resulting from north dipping subduction (Hoffman, 1988). Hope & Eaton (2002) showed that the potential field anomaly along the Vulcan Structure was better explained as the result of a single low density, high magnetic susceptibility body located along the length of the Vulcan Structure. Therefore the magnetic high does not resemble a typical volcanic terrane, and is not indicative of subduction.

Seismic and potential field modelling by Eaton et al. (1999) suggested that the Vulcan Structure was best explained as a suture zone, based on the geometry of reflective zones in the crust. These reflective zones appeared to show an underthrusting of the Loverna Block below the MHB, suggesting south dipping subduction. But the underthrusting of the lower crust could also be attributed to deformation related to collision between the Loverna Block and the Wyoming Province, and the interpretation of south dipping subduction is not necessary.

The potential field maps indicate that the Loverna Block and the MHB are distinct blocks, as indicated by distinct aeromagnetic fabric on both sides of the Vulcan Structure (Lemieux et al., 2000). This means that the Vulcan Structure must have been the site of continental collision at one time, and most likely was accompanied by subduction of an ocean basin which separated the continents. This interpretation also fits well with the seismic evidence from Gorman et al. (2002 - see Figure 6.7), who found a reflector dipping to the north beneath the Loverna Block and attributed this to north dipping subduction at the Vulcan Structure. The MT evidence presented here fits well with this
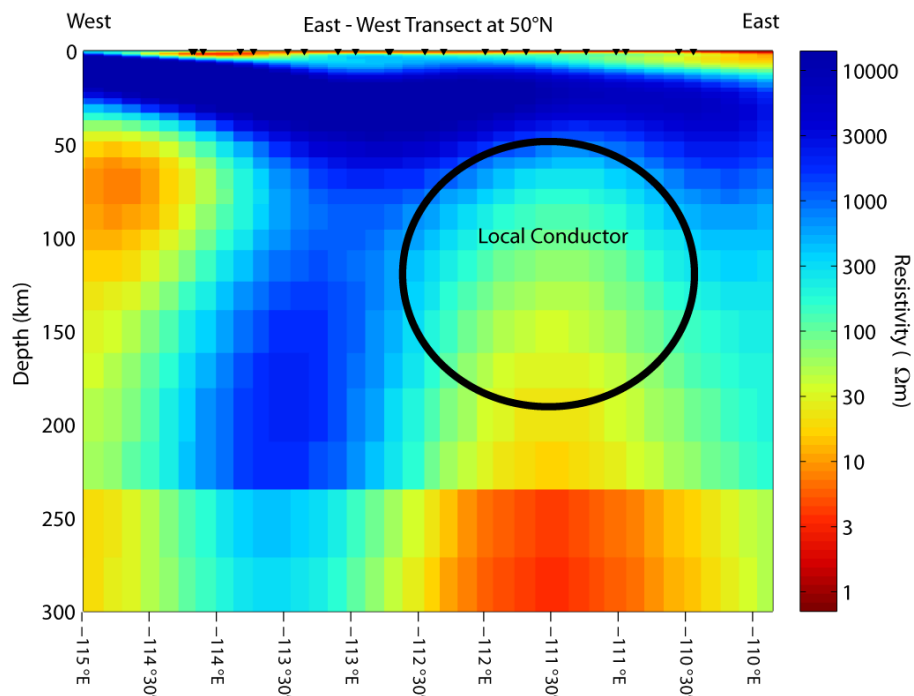
Figure 6.6: An east - west transect taken from the final model at 50°N, crossing the local conductor beneath the MHB associated with the reflector south of the Vulcan Structure.

interpretation, for reasons discussed in the following section.

There is also one more complication which needs to be addressed, and that is the local nature of the low resistivities located to the south of the Vulcan Structure. The Loverna Conductor is bounded to the south by the Vulcan Structure, and it is realistic to believe that the reflector associated with the Loverna Conductor is present even in the western portion of the model (following the conductor from the east where the reflectors were discovered). But the local conductor located to the south of the Vulcan Structure does not exist in the western portion of the model, as indicated by the east-west transect in Figure 6.6. Since the conductor does not exist in the east, it is likely that the reflector is also not present there. Therefore, the Loverna Conductor is similar from east to west, while the MHB conductor is not.
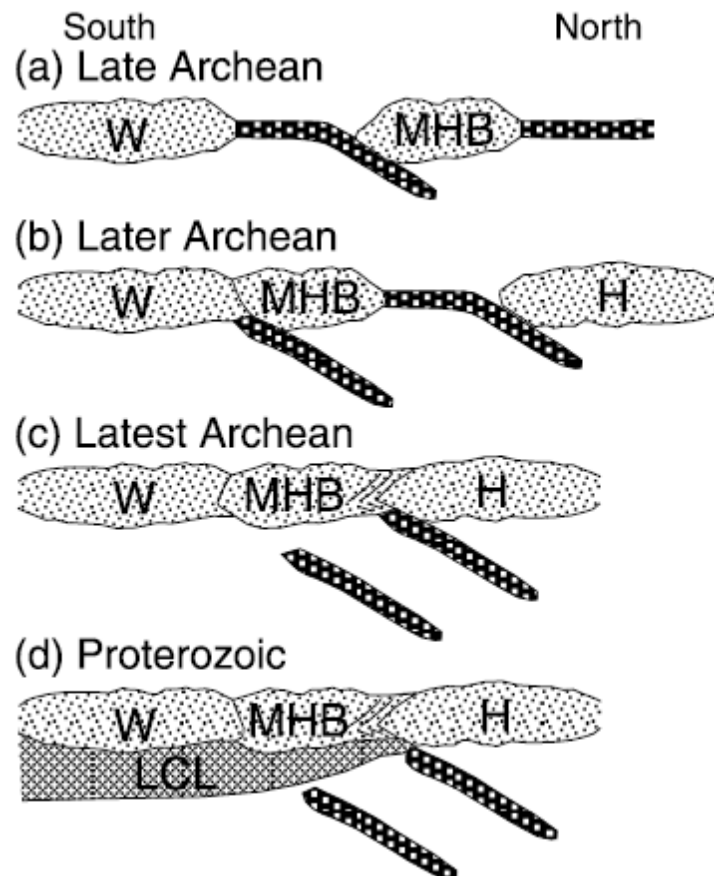
Figure 6.7: From Gorman et al. (2002). A depiction of north dipping subduction at both the Vulcan Structure (between the MHB and the Hearne Domain (H - Loverna Block)) and at the GFTZ (between the Wyoming Province (W) and the MHB). The LCL is the lower crustal layer, a high velocity layer at the bottom of the crust with a Proterozoic age

This change from east to west under the MHB was also documented by Lemieux et al. (2000), who showed from the Lithoprobe seismic reflection data that the MHB crust in the west contains westward dipping crustal imbrications, and the crust in the east appears undeformed. Therefore, the upper mantle which underlies the undeformed portion of the crust has retained the low resistivities capped by the reflector, while the imbricated zone to the west has removed the low resistivities. This may mean that the conductor to the west existed at one time, and deformation causing crustal imbrications removed the conductor, possibly breaking thin conductive films along grain boundaries, leaving the region's upper mantle resistive.

In summary, the interpretation by Gorman et al. (2002) of north dipping subduction at the Vulcan Structure remains a plausible explanation, and evidence from this modelling of MT data appears to agree with this interpretation (see Figure 6.7). It appears possible to explain the upper mantle conductors with a subduction model, and this argument will be developed further in the following section.

6.3   Mechanisms for low resistivity in the upper mantle

The Loverna conductor defined above was first reported by Boerner et al. (1999) in their 2-D, TM mode only, isotropic inversion of a profile of MT data across the Snowbird Tectonic Zone (STZ). As discussed earlier, they found that the upper mantle below the Archean Loverna Block was an order of magnitude less resistive than the upper mantle below the Proterozoic Terranes north of the STZ.

Using more data than just the TM mode, this 3-D model has confirmed the presence of the regional conductor in the upper mantle below the Loverna Block. It has also shown that the Vulcan Structure bounds this feature to the south, except for a local conductivity anomaly in the eastern side of the MHB, associated with the southern reflector discussed in the previous section.

As discussed earlier, low resistivity in the lower crust/upper mantle is most likely caused by either saline fluids in pore spaces, trapped by an impermeable cap, or graphite films along grain boundaries. This particular upper mantle conductor was previously explained by hydrous minerals (phlogopite) which will lower electrical resistivity (Boerner et al., 1999). This was suggested somewhat tentatively based on the discovery of phlogophite in xenoliths near the Great Falls Tectonic Zone (Boerner et al., 1999), although more recent

evidence suggests that phlogopite alone is not capable of explaining such conductive anomalies in the upper mantle (Chen et al., 2009). Therefore, to explain this anomaly will likely require the addition of either graphite films or trapped saline fluids.

The reflector at the top of the conductors naturally suggests an impermeable cap, since it indicates a seismic impedance contrast at that depth, which likely relates to a discontinuity in the geology. But this also means that porosity exists below the reflector, at depths within the upper mantle. The region possibly deforms through brittle deformation at present times, owing to how old and cold it is (Wannamaker, 2000), but the region has been stable for so long that it is unlikely any deformation is occurring which could create porosity. And it does not seem likely that porosity created when the region was actively deforming could remain in the upper mantle for so long.

Instead, graphite appears to be a more likely explanation for the upper mantle Loverna conductor. During subduction in the Proterozoic, carbon was carried into the upper mantle, where it was redistributed during metasomatism through a porous network as graphite. A similar conclusion has recently been reached in the interpretation of a similar structure in the Slave craton. An upper mantle conductor coincident with a dipping seismic reflector in the Slave craton has been interpreted by Chen et al. (2009) as a mixture of phlogopite and graphite which explain both the seismic structure and the resistivity structure. They attributed these minerals to metasomatism caused by subduction, which is equally plausible beneath the Loverna Block.

According to the interpretation by Gorman et al. (2002), subduction occurred at both the GFTZ and the Vulcan Structure, before terminal collision at the THO. This interpretation fits well with the electrical resistivity evidence presented here. The Loverna and local conductors show that the seismic reflectors are most likely related to metasomatism and subduction, following the model presented by Chen et al. (2009) for the Slave craton.

Presumably, subduction at the GFTZ and the Vulcan Structure happened around the same time under similar situations, because the upper mantle structure caused by subduction at the GFTZ and at the Vulcan Structure has caused very similar features in the upper mantle. This is seen in Figure 6.5 which shows the similarity between the conductors and reflectors to the north and to the south of the Vulcan Structure. This is not necessarily true, but if it is, it leads to the speculation that both of these subduction events were ongoing around the same time as subduction beneath the Slave craton was ongoing,

leaving similar upper mantle structure reported by Chen et al. (2009). This subduction is believed to have been ongoing as early as 3.2 Ga, suggesting that subduction along the Vulcan Structure and the GFTZ may have also been ongoing much earlier than 2.1 Ga as earlier proposed. This is a tentative suggestion, but the similarity between upper mantle features under these three Archean blocks strongly suggests such similarities.

Similarly, it is interesting to note that the conductor beneath the Slave craton underlies the Lac de Gras diamondiferous kimberlite field. As explained earlier, the presence of graphite in the upper mantle shows that carbon may exist at depth, and below a depth of ~160 km this carbon may exist in diamond form. The conductor beneath the Slave craton is thought to be an indicator of this situation (Jones & Craven, 2004), and its similarity to the upper mantle structure beneath the Loverna Block suggests that a similar situation may occur in southern Alberta. This means that there is a possibility for diamondiferous kimberlites to exist beneath the WCSB in southern Alberta.

Chapter 7

Conclusions

The inversion of the MT data in southern Alberta has shown that 3-D resistivity models are able to fit the data with a realistic model, and has confirmed with new data that 2-D isotropic inversions cannot realistically fit the measured data.

This does not necessarily mean that 3-D inversions are required to fit the data, since it is still possible that electrical anisotropy exists within the crust. If this is the case, the data might still be 2-D, but anisotropic resistivity structure distorts the data such that it appears 3-D. This was the initial interpretation of the 1-D models of MT data collected in southern Alberta by Vozoff & Ellis (1966), and was also the conclusion of the 2-D modelling of the Lithoprobe data by Boerner et al. (2000). The fact that the 3-D models presented in this thesis are able to fit the data means that anisotropy does not need to be invoked to explain the southern Alberta MT data. However it seems likely that 2-D anisotropic models could also be found that fit the measured data.

Other types of geophysical data correlate well with this model, suggesting that this 3-D model is robust. The spatial coincidence of the seismic reflectors and the top of the Loverna conductor gives strong evidence supporting the existence of this conductor as a geological phenomenon, not an artefact of improper modelling. The MHB was subdivided into zones of high and low resistivity, which correlated spatially with the deformed and undeformed crust discovered by Lemieux et al. (2000). The potential field maps of the Vulcan Structure correlate very well with the southern edge of the Loverna conductor, and the 2-D modelling of the TM mode MT data by Boerner et al. (1999) showed that the upper mantle below the Loverna Block was significantly less resistive than the upper mantle below the younger terranes to the northwest. Therefore this resistivity model represents the most accurate view of the Lithosphere below southern Alberta to date.

One unexpected result of our model is the near surface high resistivity beneath the Foothills and Rocky Mountains to the west. It contrasts significantly with the less resistive WCSB throughout the rest of Alberta, and the boundary is marked by a deepening of the low resistive zone associated with the sedimentary basin. This feature was the most difficult feature in the data to fit with the 3-D inversion, and required a

higher density of stations in the western portion of the model in order to fit it properly. It likely represents the presence of saline fluids in fracture zones at the top of the Precambrian basement, bordering the thrust features of the Rocky Mountains.

The existence of the Loverna Conductor has confirmed the result of Boerner et al. (1999), showing that the upper mantle below the Loverna Block is about two orders of magnitude less resistive than most of the crust. This conductive zone is also existent below the eastern portion of the MHB, and correlates with a reflector which appears to cap the region.

The resistivity model lends support to the interpretation by Gorman et al. (2002), showing that the Vulcan Structure is best explained as a north dipping subduction zone. The timing remains relatively unconstrained, but the striking similarity in structure to an upper mantle feature beneath the Slave craton suggests a possible link. This similarity also indicates that southern Alberta has the potential for diamondiferous kimberlites, based on the existence of carbon in the lithosphere.

Further tests of the 3-D model such as the addition of the tipper data would be useful in trying to fit all of the data in southern Alberta better.

References

Anderson, J. L. (1983). Proterozoic anorogenic granite plutonism of North America. *Proterozoic geology; Selected Papers from an international Proterozoic symposium: Geological Society of America Memoir*.

Archie, G. E. (1942). The electrical resistivity log as an aid in determining some reservoir characteristics. *Petroleum Transactions of AIME*, *146*, 54-62.

Armstrong, R. L. (1988). Mesozoic and early Cenozoic magmatic evolution of the Canadian Cordillera. In S. P. Clark (Ed.), *Processes in Continental lithosphere deformation. Geological Society of America Special Paper* (218th ed., pp. 55-91).

Bahr, K. (1988). Interpretation of the Magnetotelluric Impedance Tensor - Regional Induction and Local Telluric Distortion. *Journal of Geophysics-Zeitschrift fur Geophysik*, *62*(2), 119-127.

Bailey, R. C., Craven, J. A., Macnae, J. C., & Polzer, B. D. (1989). Imaging of deep fluids in Archaean crust. *Nature*, *340*(6229), 136-138.

Bankey, V., Cuevas, A., Daniels, D., Finn, C. A., Hernandez, I., Hill, P., Kucks, R., et al. (2002). Digital data grids for the magnetic anomaly map of North America. Retrieved December 15, 2010, from ftp://ftpext.usgs.gov/pub/cr/co/denver/musette/pub/open-file-reports/ofr-02-0414

Bedard, J. (2006). A catalytic delamination-driven model for coupled genesis of Archaean crust and sub-continental lithospheric mantle. *Geochimica et Cosmochimica Acta*, *70*(5), 1188-1214.

Boerner, D. E., Craven, J. A., Kurtz, R. D., Ross, G. M., & Jones, F. W. (1998). The Great Falls Tectonic Zone: suture or intracontinental shear zone? *Canadian Journal of Earth Sciences*, *35*(2), 175-183. NRC Research Press.

Boerner, D. E., Kurtz, R. D., & Craven, J. A. (1996). Electrical conductivity and Paleo-Proterozoic foredeeps. *Journal of Geophysical Research*, *101*(B6), 13775-13791.

Boerner, D. E., Kurtz, R. D., Craven, J. A., Rondenay, S., & Qian, W. (1995). Buried Proterozoic foredeep under the Western Canada Sedimentary Basin? *Geology*, *23*(4), 297.

Boerner, D. E., Kurtz, R. D., Craven, J. A., Ross, G. M., & Jones, F. W. (2000). A synthesis of electromagnetic studies in the Lithoprobe Alberta Basement Transect: constraints on Paleoproterozoic indentation tectonics. *Canadian Journal of Earth Sciences*, *37*(11), 1509-1534.

Boerner, D. E., Kurtz, R. D., Craven, J. A., Ross, G. M., Jones, F. W., & Davis, W. J. (1999). Electrical Conductivity in the Precambrian Lithosphere of Western Canada. *Science*, *283*(5402), 668-670. AAAS.

Bouzidi, Y., Schmitt, D. R., Burwash, R. A., & Kanasewich, E. R. (2002). Depth migration of deep seismic reflection profiles: crustal thickness variations in Alberta. *Canadian Journal of Earth Sciences*, *39*(3), 331-350.

Brasse, H., Kapinos, G., Li, Y., Mütschard, L., Soyer, W., & Eydam, D. (2009). Structural electrical anisotropy in the crust at the South-Central Chilean continental

margin as inferred from geomagnetic transfer functions. *Physics of the Earth and Planetary Interiors*, *173*(1-2), 7-16.

Buhlmann, A. L., Cavell, P., Burwash, R. A., Creaser, R. A., & Luth, R. W. (2000). Minette bodies and cognate mica-clinopyroxenite xenoliths from the Milk River area, southern Alberta: records of a complex history of the northernmost part of the Archean Wyoming craton. *Canadian Journal of Earth Sciences*, *37*(11), 1629-1650.

Burwash, R. A., Baadsgaard, H., & Peterman, Z. E. (1962). Precambrian K-Ar Dates from the Western Canada Sedimentary Basin. *Journal of Geophysical Research*, *67*(4), 1617-1625.

Cagniard, L. (1953). Basic Theory of the Magneto-Telluric Method of Geophysical Prospoecting. *Geophysics*, *18*(3), 605.

Chen, C.-W., Rondenay, S., Evans, R. L., & Snyder, D. B. (2009). Geophysical detection of relict metasomatism from an Archean (approximately 3.5 Ga) subduction zone. *Science (New York, N.Y.)*, *326*(5956), 1089-91.

Clowes, R. M., Hammer, P., Mandler, H., Ross, G. M., Cook, F. A., & Eaton, D. W. (1997). The Vulcan Low, Matzhiwin High and related domains as revealed by SALT 95 reflection data. In G. M. Ross (Ed.), *Alberta Basement Transects Workshop, Lithoprobe Report #59* (pp. 15 - 22). Lithoprobe Secretariat, University of British Columbia.

Constable, S. C., Parker, R. L., & Constable, C. G. (1987). Occam's inversion: A practical algorithm for generating smooth models from electromagnetic sounding data. *Geophysics*, *52*(3), 289.

Corrigan, D., Galley, A. G., & Pehrsson, S. (2007). Tectonic Evolution and Metallogeny of the Southwestern Trans-Hudson Orogen. In W. D. Goodfellow (Ed.), *Mineral Deposits of Canada:A Synthesis of Major Deposit-Types, District Metallogeny, the Evolution of Geological Provinces, and Exploration Methods* (pp. 881 - 902). Geological Association of Canada, Mineral Deposits Division, Special Publication No. 5.

Davis, W. J., Berman, R., & Kjasrsgaard, B. (1995). U-Pb Geochronology and Isotopic Studies of Crustal Xenoliths from the Archean Medicine Hat Block, Northern Montana and Southern Alberta: Paleoproterozoic Reworking of Archean Lower Crust. In G. M. Ross (Ed.), *Alberta Basement Transects Workshop, Lithoprobe Report #47* (pp. 329 - 334). Lithoprobe Secretariat, University of British Columbia.

DeGroot-Hedlin, C., & Constable, S. (1993). Occam's Inversion and the North American Central Plains Electrical Anomaly. *Journal of geomagnetism and geoelectricity*, *45*, 985-999.

Deiss, C. F. (1941). Cambrian geography and sedimentation in the central Cordilleran region. *Geological Society of America Bulletin*, *52*, 1085-1115.

Eaton, D. W., & Cassidy, J. F. (1996). A relic proterozoic subduction zone in western Canada: New evidence from seismic reflection and receiver function data. *Geophysical Research Letters*, *23*(25), 3791.

Eaton, D. W., Darbyshire, F., Evans, R. L., Grütter, H. S., Jones, A. G., & Yuan, X. (2009). The elusive lithosphere–asthenosphere boundary (LAB) beneath cratons. *Lithos*, *109*(1-2), 1-22. Elsevier B.V.

Eaton, D. W., Ross, G. M., & Clowes, R. M. (1999). Seismic-reflection and potential-field studies of the Vulcan structure, western Canada: A Paleoproterozoic Pyrenees? *Journal of Geophysical Research*, *104*(B10), 23255-23269.

Egbert, G. D., & Booker, J. R. (1986). Robust estimation of geomagnetic transfer functions. *Geophysical Journal International*, *87*(1), 173-194.

English, J. M., Johnston, S. T., & Wang, K. (2003). Thermal modelling of the Laramide orogeny: testing the flat-slab subduction hypothesis. *Earth and Planetary Science Letters*, *214*(3-4), 619-632.

Erdmer, P., Heaman, L., Creaser, R. a, Thompson, R. I., & Daughtry, K. L. (2001). Eocambrian granite clasts in southern British Columbia shed light on Cordilleran hinterland crust. *Canadian Journal of Earth Sciences*, *38*(7), 1007-1016.

Furnes, H., Rosing, M., Dilek, Y., & de Wit, M. (2009). Isua supracrustal belt (Greenland)—A vestige of a 3.8 Ga suprasubduction zone ophiolite, and the implications for Archean geology. *Lithos*, *113*(1-2), 115-132.

Gamble, T. D., Goubau, W. M., & Clarke, J. (1979). Magnetotellurics with a remote magnetic reference. *Geophysics*, *44*(1), 53.

Garcia, X., & Jones, A. G. (2002). Decomposition of three-dimensional magnetotelluric data. In M. S. Zhdanov & P. E. Wannamaker (Eds.), *Methods in Geochemistry and Geophysics; Three-Dimensional Electromagnetics, Proceedings of the Second International Symposium* (35th ed., pp. 232-250).

Gorman, A. R., Clowes, R. M., Ellis, R. M., Henstock, T. J., Spence, G. D., Keller, G. R., Levander, A., et al. (2002). Deep Probe: imaging the roots of western North America. *Canadian Journal of Earth Sciences*, *39*(3), 375-398.

Gough, D. I. (1986a). Mantle Upflow Tectonics in the Canadian Cordillera. *Journal of Geophysical Research*, *91*(B2), 1909-1919.

Gough, D. I. (1986b). Seismic reflectors, conductivity,water and stress in the continental crust. *Nature*, *323*(6084), 143-144.

Gough, D. I. (1992). Electromagnetic exploration for fluids in the Earth's crust. *Earth-Science Reviews*, *32*(1-2), 3-18.

Gough, D. I., Bingham, D. K., Ingham, M. R., & Alabi, A. (1982). Conductive structures in southwestern Canada : a regional magnetometer array study. *Canadian Journal of Earth Sciences*, *19*(8), 1680-1690.

Groom, R. W., & Bailey, R. C. (1989). Decomposition of Magnetotelluric Impedance Tensors in the Presence of Local Three-Dimensional Galvanic Distortion. *Journal of Geophysical Research*, *94*(B2), 1913-1925.

Hanmer, S., Parrish, R., Williams, M. L., & Kopf, C. (1994). Striding-Athabasca mylonite zone: Complex Archean deep-crustal deformation in the East Athabasca mylonite triangle, northern Saskatchewan. *Canadian Journal of Earth Sciences*, *31*, 1287 - 1300.

Hanmer, S., Williams, M. L., & Kopf, C. (1995). Striding Athabasca mylonite zone: implications for the Archean and Early Proterozoic tectonics of the western Canadian Shield. *Canadian Journal of Earth Sciences*, *32*, 178-196.

Hoffman, P. F. (1988). United Plates of America, The Birth of a Craton: Early Proterozoic Assembly and Growth of Laurentia. *Annual Review of Earth and Planetary Sciences*, *16*(1), 543-603.

Hoffman, P. F. (1989a). Speculations on Laurentia's first gigayear (2.0 to 1.0 Ga). *Geology*, *17*(2), 135.

Hoffman, P. F. (1989b). Precambrian geology and tectonic history of North America. *The Geology of North America Vol. A, The Geology of North America-An Overview*. The Geology Society of America.

Hope, J., & Eaton, D. W. (2002). Crustal structure beneath the Western Canada Sedimentary Basin: constraints from gravity and magnetic modelling. *Canadian Journal of Earth Sciences*, *39*(3), 291-312.

Hyndman, R. D., & Shearer, P. M. (1989). Water in the lower continental crust: modelling magnetotelluric and seismic reflection results. *Geophysical Journal International*, *98*(2), 343-365.

Jones, A. G. (1999). Imaging the continental upper mantle using electromagnetic methods. *Lithos*, *48*(1-4), 57-80.

Jones, A. G., & Craven, J. A. (2004). Area selection for diamond exploration using deep-probing electromagnetic surveying. *Lithos*, *77*(1-4), 765-782.

Jones, A. G., & Groom, R. W. (1993). Strike-angle determination from the magnetotelluric impedance tensor in the presence of noise and local distortion: rotate at your peril! *Geophysical Journal International*, *113*(2), 524-534.

Jones, A. G., Evans, R. L., Muller, M. R., Hamilton, M. P., Miensopust, M. P., Garcia, X., Cole, P., et al. (2009). Area selection for diamonds using magnetotellurics: Examples from southern Africa. *Lithos*, *112*, 83-92. Elsevier B.V.

Jones, A. G., Ledo, J., & Ferguson, I. J. (2005). Electromagnetic images of the Trans-Hudson orogen: the North American Central Plains anomaly revealed. *Canadian Journal of Earth Sciences*, *42*(4), 457-478.

Jones, F. W., Munro, R. A., Craven, J. A., Boerner, D. E., Kurtz, R. D., & Sydora, R. D. (2002). Regional geoelectrical complexity of the Western Canada Basin from magnetotelluric tensor invariants. *Earth, Planets Space*, *54*(9), 899-905.

Kanasewich, E. R. (1968). Precambrian Rift: Genesis of Strata-Bound Ore Deposits. *Science (New York, N.Y.)*, *161*(3845), 1002-1005.

Karlstrom, K., Ahall, K.-I., Harlan, S. S., Williams, M. L., McLelland, J., & Geissman, J. W. (2001). Long-lived (1.8–1.0 Ga) convergent orogen in southern Laurentia, its extensions to Australia and Baltica, and implications for refining Rodinia. *Precambrian Research*, *111*(1-4), 5-30.

Kirschivink, J. L. (1992). Late Proterozoic Low-Latitude Global Glaciation: the Snowball Earth. In J. W. Schopf & C. Klein (Eds.), *The Proterozoic Biosphere: A Multidisciplinary Study.* (pp. 51-52). Cambridge University Press.

Lemieux, S., Ross, G. M., & Cook, F. A. (2000). Crustal geometry and tectonic evolution of the Archean crystalline basement beneath the southern Alberta Plains, from new seismic reflection and potential-field studies. *Canadian Journal of Earth Sciences*, *37*(11), 1473-1491.

Maclachlan, K., Davis, W. J., & Relf, C. (2005). Paleoproterozoic reworking of an Archean thrust fault in the Hearne domain , Western Churchill Province : U – Pb geochronological constraints 1. *Canadian Journal of Earth Sciences*, *1330*, 1313-1330.

Maxwell, J. C. (1861). On Physical Lines of Force. *Philisophical Magazine*.

McNeice, G. W., & Jones, A. G. (2001). Multisite, multifrequency tensor decomposition of magnetotelluric data. *Geophysics*, *66*(1), 158.

Mueller, P. A., Heatherington, A. L., Kelly, D. M., Wooden, J. L., & Mogk, D. W. (2002). Paleoproterozoic crust within the Great Falls tectonic zone: Implications for the assembly of southern Laurentia. *Geology*, *30*(2), 127.

Nair, R., & Chacko, T. (2008). Role of oceanic plateaus in the initiation of subduction and origin of continental crust. *Geology*, *36*(7), 583.

Natural Resources Canada. (2010). Canadian Geodetic Information System, Gravity & Geodetic Networks Section, Geodetic Survey Division, Geomatics Canada, Earth Sciences Sector. Retrieved December 15, 2010, from http://gdcinfo.agg.nrcan.gc.ca/contact_e.html#DataCentre

Niblett, E. R., & Sayn-Wittgenstein, C. (1960). Variation of Electrical Conductivity with Depth by the Magneto-Telluric Method. *Geophysics*, *25*(5), 998.

Parkinson, W. D. (1959). Directions of Rapid Geomagnetic Fluctuations. *Geophysical Journal International*, *2*(1), 1-14.

Peeples, W. J., & Rankin, D. (1973). A magnetotelluric study in the western Canadian sedimentary basin. *Pure and Applied Geophysics*, *102*(1), 134-147.

Phillips, J. D., Duval, J. S., & Ambroziak, R. A. (1993). National geophysical data grids; gamma-ray, gravity, magnetic, and topographic data for the conterminous United States. *USGS Digital Data Series DDS-9*. Retrieved December 15, 2010, from ftp://ftpext.usgs.gov/pub/cr/co/denver/musette/pub/GEOPHYSICAL_DATA/cdrom _DDS-9

Pilkington, M., Miles, W., Ross, G. M., & Roest, W. (2000). Potential field signatures of buried Precambrian basement in the Western Canada Sedimentary Basin. *Canadian Journal of Earth Sciences*, *37*(11), 1453-1471.

Price, R. A. (1994). Cordilleran Tectonics and the Evolution of the Western Canada Sedimentary Basin. In G. D. Mossop & I. Shetsen (Eds.), *Geological Atlas of the Western Canada Sedimentary Basin* (Special Re., pp. 13 - 24). Canadian Society of Petroleum Geologists and Alberta Research Council.

Price, R. A., & Sears, J. W. (2000). A Preliminary Palinspastic Map of the Mesoproterozoic Belt-Purcell Supergroup , Canada and USA : Implications for the Tectonic Setting and Structural Evolution of the Purcell Anticlinorium and the Sullivan Deposit. In J. W. Lydon, T. Hoy, J. F. Slack, & M. E. Knapp (Eds.), *The Geological Environment of the Sullivan Deposit, British Columbia* (Special Pu., pp. 61-81). Geological Association of Canada, Mineral Deposits Division.

Rankin, D., & Reddy, I. K. (1969). A Magnetotelluric Study of Resistivity Anisotropy. *Geophysics*, *34*(3), 438.

Reddy, I. K., & Rankin, D. (1971). Magnetotelluric Measurements in Central Alberta. *Geophysics*, *36*(4), 739.

Reddy, I. K., & Rankin, D. (1972). On the Interpretation of Magnetotelluric Data in the Plains of Alberta. *Canadian Journal of Earth Sciences*, *9*, 514-527.

Rodi, W., & Mackie, R. L. (2001). Nonlinear conjugate gradients algorithm for 2-D magnetotelluric inversion. *Geophysics*, *66*(1), 174.

Ross, G. M. (2000). Introduction to special issue of Canadian Journal of Earth Sciences: The Alberta Basement Transect of Lithoprobe. *Canadian Journal of Earth Sciences*, *37*(11), 1447-1452.

Ross, G. M. (2002). Evolution of Precambrian continental lithosphere in Western Canada: results from Lithoprobe studies in Alberta and beyond. *Canadian Journal of Earth Sciences*, *39*(3), 413-437.

Ross, G. M., & Villeneuve, M. E. (2003). Provenance of the Mesoproterozoic (1.45 Ga) Belt basin (western North America): Another piece in the pre-Rodinia paleogeographic puzzle. *Geological Society of America Bulletin*, *115*(10), 1191.

Ross, G. M., Eaton, D. W., Boerner, D. E., & Miles, W. (2000). Tectonic entrapment and its role in the evolution of continental lithosphere: An example from the Precambrian of western Canada. *Tectonics*, *19*(1), 116.

Ross, G. M., Milkereit, B., Eaton, D. W., White, D., Kanasewich, E. R., & Burianyk, M. J. A. (1995). Paleoproterozoic collisional orogen beneath the western Canada sedimentary basin imaged by Lithoprobe crustal seismic-reflection data. *Geology*, *23*(3), 195.

Ross, G. M., Parrish, R., Villeneuve, M. E., & Bowring, S. A. (1991). Geophysics and geochronology of the crystalline basement of the Alberta Basin, western Canada. *Canadian Journal of Earth Sciences*, *28*(4), 512-522.

Sears, J. W., St. George, G. M., & Winne, J. C. (2005). Continental rift systems and anorogenic magmatism. *Lithos*, *80*(1-4), 147-154.

Shragge, J., Bostock, M. G., Bank, C. G., & Ellis, R. M. (2002). Integrated teleseismic studies of the southern Alberta upper mantle. *Canadian Journal of Earth Sciences*, *39*(3), 399-411.

Simpson, F., & Bahr, K. (2005). *Practical Magnetotellurics. Cambridge Univ. Press, Cambridge, U. K.* (p. 270). Cambridge: Cambridge University Press.

Sims, W. E., Bostick, F. X., & Smith, H. W. (1971). the Estimation of Magnetotelluric Impedance Tensor Elements From Measured Data. *Geophysics*, *36*(5), 938.

Siripunvaraporn, W., & Egbert, G. D. (2000). An efficient data-subspace inversion method for 2-D magnetotelluric data. *Geophysics*, *65*(3), 791.

Siripunvaraporn, W., & Egbert, G. D. (2009). WSINV3DMT: Vertical magnetic field transfer function inversion and parallel implementation. *Physics of the Earth and Planetary Interiors*, *173*(3-4), 317-329.

Siripunvaraporn, W., Egbert, G. D., Lenbury, Y., & Uyeshima, M. (2005). Three-dimensional magnetotelluric inversion: data-space method. *Physics of The Earth and Planetary Interiors*, *150*(1-3), 3-14.

Soyer, W., & Unsworth, M. J. (2006). Deep electrical structure of the northern Cascadia (British Columbia, Canada) subduction zone: Implications for the distribution of fluids. *Geology*, *34*(1), 53.

Srivastava, S. P., Douglass, J. L., & Ward, S. H. (1963). The Application of the Magnetotelluric and Telluric Methods in Central Alberta. *Geophysics*, *28*(3), 426.

Swift, C. M. (1967). *A Magnetotelluric Investigation of an Electrical Conductivity Anomaly in the Southwestern United States*. *Geology*. Massachusetts Institute of Technology.

Tohver, E., Teixeira, W., van der Pluijm, B., Geraldes, M. C., Bettencourt, J. S., & Rizzotto, G. (2006). Restored transect across the exhumed Grenville orogen of Laurentia and Amazonia, with implications for crustal architecture. *Geology*, *34*(8), 669.

Turkoglu, E., Unsworth, M. J., & Pana, D. I. (2009). Deep electrical structure of northern Alberta (Canada): implications for diamond exploration. *Canadian Journal of Earth Sciences*, *46*(2), 139-154.

Unsworth, M. J. (2010). *C4.2, Geophysics 424 Lecture Notes, September 2010*. *University of Alberta* (pp. 1-12).

Unsworth, M. J., Malin, P. E., Egbert, G. D., & Booker, J. R. (1997). Internal structure of the San Andreas fault at Parkfield, California. *Geology*, *25*(4), 359.

Vozoff, K., & Ellis, R. M. (1966). Magnetotelluric Measurements in Southern Alberta. *Geophysics*, *31*(6), 1153.

Vozoff, K., Hasegawa, H., & Ellis, R. M. (1963). Results and Limitations of Magnetotelluric Surveys in Simple Geologic Situations. *Geophysics*, *28*(5), 778.

Wang, X.-shuo. (1988a). Inversion of magnetovariation event to causative current. I. Current sheet model. *Physics of The Earth and Planetary Interiors*, *53*(1-2), 46-54.

Wang, X.-shuo. (1988b). Inversion of magnetovariation event to causative current. III. Test of channelled current model, SABC conductor inverted as chennelled currents and structure evaluation. *Physics of The Earth and Planetary Interiors*, *53*(1-2), 64-79.

Wannamaker, P. E. (2000). Comment on "The petrologic case for a dry lower crust" by Bruce W. D. Yardley and John W. Valley. *Journal of Geophysical Research*, *105*(B3), 6057-6064.

Weaver, J. T., Agarwal, A. K., & Lilley, F. E. M. (2000). Characterization of the magnetotelluric tensor in terms of its invariants. *Geophysical Journal International*, *141*(2), 321-336.

Wiese, H. (1962). Geomagnetische Tiefentellurik Teil II: Die Streichrichtung der untergrundstrukturen des elektrischen Widerstandes, erschlossen aus geomagnetischen Variationen. *Geofisica Pura e Applicata*, *52*(1), 83-103.

Wilde, S. A., Valley, J. W., Peck, W. H., & Graham, C. M. (2001). Evidence from detrital zircons for the existence of continental crust and oceans on the Earth 4.4 Gyr ago. *Nature*, *409*(6817), 175-8.

Xiao, W., & Unsworth, M. J. (2006). Structural imaging in the Rocky Mountain Foothills (Alberta) using magnetotelluric exploration. *AAPG Bulletin*, *90*(3), 321-333.

Xu, Y., Shankland, T. J., & Poe, B. T. (2000). Laboratory-based electrical conductivity in the Earth's mantle. *Journal of Geophysical Research*, *105*(B12), 27865-27875.

Yardley, B. W. D., & Valley, J. W. (1997). The petrologic case for a dry lower crust. *Journal of Geophysical Research*, *102*(B6), 12173-12185.

Zhao, G. (2004). A Paleo-Mesoproterozoic supercontinent: assembly, growth and breakup. *Earth-Science Reviews*, *67*(1-2), 91-123.

Appendix A
Magnetotelluric Theory and Method

Magnetotelluric (MT) exploration is a geophysical method which uses low frequency electromagnetic (EM) waves to measure the electrical resistivity (or its inverse, conductivity) structure of the Earth from depths that range from the surface to the mantle.

The resistivity structure of the upper crust is mostly defined by its fluid content. Fluid properties such as salinity, and pore attributes such as pore space and connectivity will have the greatest effect on the resistivity of a rock (Archie, 1942). For example, low resistivity in the fracture zone of the San Andreas fault was attributed to fluids in the fractures (Unsworth et al., 1997).

In situations where fluids are not expected (such as the lower crust below continental cratons), variations in resistivity are most likely related to changes in mineralogy. For example, a strong linear conductor located along a Precambrian orogenic zone in North America was attributed to graphite (Jones et al., 2005).

MT uses naturally occurring EM signals that are measured at the surface of the Earth. The depth to which these signals penetrate is controlled by the frequency; so measuring a range of frequencies will give a depth sounding. Note that the signal period is simply the reciprocal of the frequency.

This Appendix explains the theoretical basis for MT exploration, and explains how MT can be used to find a resistivity model of the Earth.

A.1   Governing Equations

The basis for magnetotelluric (MT), and all other electromagnetic exploration techniques, is electromagnetic induction described by Maxwell Equations (Maxwell, 1861). These equations describe the generation of the electric and magnetic fields, and how EM waves travel.

Maxwell's equations describe how EM waves travel within a medium such as the Earth. The medium is described in terms of three parameters: magnetic permeability μ, dielectric permittivity ε, and an electrical resistivity ρ (or its inverse, conductivity σ).

Maxwell`s first two equations are written as:

$$\nabla \cdot \boldsymbol{E} = {}^{\gamma}\!/_{\varepsilon} \tag{0.5}$$

$$\nabla \cdot \boldsymbol{B} = 0 \tag{0.6}$$

where the $\boldsymbol{E}$ is the electric field, $\boldsymbol{B}$ is the magnetic flux density (referred to here as the magnetic field), and γ represents the electric charge density.

The first equation (0.5) describes the fact that the electric field flux through a closed surface is proportional to the electric charge located within that surface. The second equation (0.6) describes the fact that the magnetic flux through a closed surface is always zero. This reflects the fact that electric monopoles can exist, but magnetic monopoles are always found as pairs of opposite sign. Maxwell`s last two equations relate the electric and magnetic fields to each other:

$$\nabla \times \boldsymbol{E} = -\frac{\partial \boldsymbol{B}}{\partial t} \tag{0.7}$$

$$\nabla \times \boldsymbol{B} = \mu \boldsymbol{J} \tag{0.8}$$

where $\boldsymbol{J}$ stands for the total current density.

Equation (0.7) is known as Faraday`s law, and describes how a time varying magnetic field generates an electric field. This equation quantifies the observation that a time varying magnetic field will induce an electric field.

Equation (0.8) is Ampere`s law, and describes how a magnetic field will be generated by a constant electric current. Maxwell showed that equation 0.8 was not complete, the generalized form of Ampere's law includes a term representing the displacement current $\left(\mu_0 \varepsilon_0 \frac{\partial \boldsymbol{E}}{\partial t}\right)$, which shows that a time varying electric field will induce a magnetic field. Since the resistivity of the Earth is relatively large it can be shown that in the frequencies used in MT, the displacement current term is small enough to be ignored. Without the displacement current, there is not wave propagation, instead the EM signals measured in MT travel through diffusion.

The permittivity, resistivity, and permeability of a medium all affect how an EM wave travels through that medium. The relationship between these material properties and the electric and magnetic fields are given by the constitutive relations:

$$\boldsymbol{J} = \sigma \boldsymbol{E} \tag{0.9}$$

$$\boldsymbol{B} = \mu \boldsymbol{H} \tag{0.10}$$

$$\boldsymbol{D} = \varepsilon \boldsymbol{E} + \boldsymbol{P} \tag{0.11}$$

where $\boldsymbol{H}$ is the magnetic field strength, $\boldsymbol{D}$ is the electric displacement field, and $\boldsymbol{P}$ is the polarization density. These three constitutive relations show the relationship of the resistivity, permeability, and permittivity to the electric and magnetic fields described by Maxwell's Equations.

The first of the constitutive relations (0.9) shows that the electric field and the total current density are related through the electrical resistivity of the medium. This means that the electrical resistivity (or its inverse, conductivity) is a measure of how easily current can flow through a medium.

Equation (0.10) relates the magnetic field strength, and the magnetic flux density through the permeability of the medium. This constitutive relation shows that the magnetic flux density depends on how easily a medium is magnetized (the definition of permeability), and the strength of the magnetic field.

The last constitutive relation (0.11) shows that the electric displacement field is dependent on both the polarization density, and the electric field together with the permittivity of the medium. The polarization term represents a divergence associated with the bound charge (electric charge confined to atom or molecule) in a material, and the permittivity term represents the divergence associated with how easily a material transmits an electric field.

In general, all three values (resistivity, permeability, and permittivity) change in the Earth, but in practice, the variations in electrical resistivity are much larger than variations in the other two parameters. Because of this, free space values for permeability (μ_0) and permittivity (ε_0) are used, and it is assumed that they do not vary with location in the subsurface.

Next we seek to understand how EM signals travel in the Earth. To do this we will derive an equation for electric field, by eliminating the magnetic field. Taking the curl of equation (0.7), substituting equation (0.8), and using equation (0.9), we can derive the induction equation, a differential equation which describes the behaviour of electric fields in a resistive medium:

$$\nabla \times (\nabla \times \boldsymbol{E}) = -\mu_0 \sigma \frac{\partial \boldsymbol{E}}{\partial t} \tag{0.12}$$

Note that a similar equation can be derived for the magnetic field by taking the curl of equation (0.8), and substituting equation (0.7).

Equation (0.12) can be further simplified assuming there are no free electric charges within the Earth (which means equation (0.5) becomes $\nabla \cdot \boldsymbol{E} = 0$), giving:

$$\nabla^2 \boldsymbol{E} = \mu_0 \sigma \frac{\partial \boldsymbol{E}}{\partial t} \tag{0.13}$$

Equation (0.13) is a diffusion equation, showing that the electric field travels in the Earth diffusively. A similar equation can be derived for the magnetic field, indicating that both travel in the earth diffusively.

A.2   Electric and Magnetic fields in a 1-D Earth

For the purposes of illustrating the diffusive nature of the electric and magnetic fields in the Earth, this section will describe the solution to the 1-D diffusion equation (where electrical resistivity only varies with depth, see Figure A.0.2). We can seek a one dimensional solution to the diffusion equation (0.13) of the form:

$$\boldsymbol{E} = \boldsymbol{E}_0 e^{-i\omega t - kz} \tag{0.14}$$

Where the value of k describes the medium through which the signal is travelling, $\boldsymbol{E}_0$ is the amplitude of the signal at the earth – air interface, ω is the angular frequency of the signal, t represents the wave's time dependence and z stands for the depth.

Equation (0.14) can be written out in a more intuitive form:

$$\boldsymbol{E} = \boldsymbol{E}_0 e^{-kz}[cos(\omega t) - isin(\omega t)] \tag{0.15}$$

From (0.15) it can be seen that the solution contains an exponential term indicating how the electric field changes with depth, and a sinusoidal term indicating how the wave
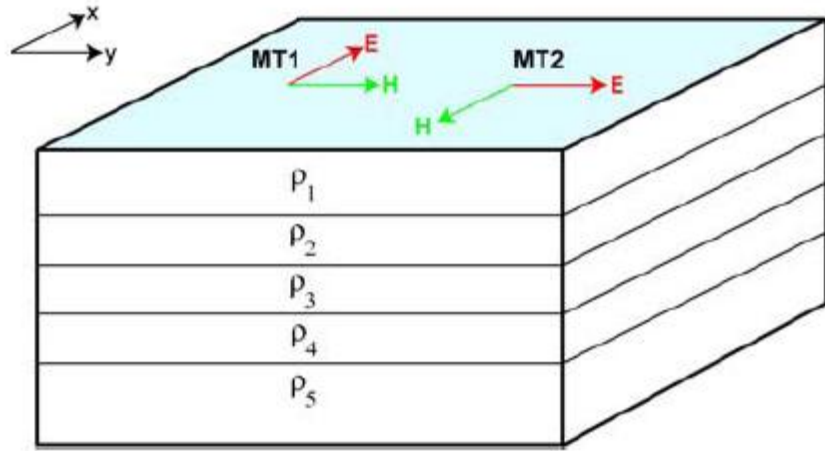
Figure A.0.1: From (Unsworth, 2010); A depiction of a 1-D layered earth, showing that MT measurements of E_x-H_y will give identical results to those derived from E_y-H_x measurement.

travels in time. The exponential term indicates an exponential decrease of amplitude with depth, but also a dependence on the properties of the earth through k.

By substituting (0.14) into (0.13), it can be shown that:

$$k = \pm(1 - i)\sqrt{\frac{\omega \mu_0 \sigma}{2}} \qquad (0.16)$$

The value of k is dependent on the resistivity of the Earth and the frequency of the wave, indicating that the attenuation of the exponential term in (0.15) is also dependant on these values. This attenuation is quantified through the concept of the skin depth.

The skin depth (δ) provides a measure of how deep a signal of a given frequency will penetrate into the Earth before being attenuated. The skin depth is defined as the depth at which the amplitude of the electric field has been reduced to $1/e$ of its amplitude at the surface. If the Earth has a uniform resistivity, then it can be shown that the skin depth is:

$$\delta = \frac{1}{\sqrt{\pi \mu_0 \sigma f}} \qquad (0.17)$$

Equation (0.17) shows that the skin depth is proportional to the Earth's electrical resistivity, and inversely proportional to the frequency (*f*) of the EM signal, meaning that both high frequency and low resistivity will cause shallow attenuation of the EM wave. MT soundings rely on this principle, whereby measuring EM fields over a range of frequencies will sample a range of depths within the earth (see Figure A.0.2).

It should be noted that a diffusion equation with the same form as (0.13) can be derived for the magnetic field, allowing the same form of solution as (0.14). This means that the attenuation of both the electric and magnetic field are governed by the skin depth, and both signals travel sinusoidally according to the same set of equations.

Now that we have established how electric and magnetic fields travel in the earth, we can consider how they interact in the Earth.

A.3   Coupling of the Electric and Magnetic Fields within the Earth

Beginning again with Maxwell's equations, six equations result from expanding Faraday's law (0.7), and Ampere's law (equation (0.8):

$$\frac{\partial B_z}{\partial y} - \frac{\partial B_y}{\partial z} = \mu\sigma E_x \qquad \frac{\partial B_x}{\partial z} - \frac{\partial B_z}{\partial x} = \mu\sigma E_y \qquad \frac{\partial B_y}{\partial x} - \frac{\partial B_x}{\partial y} = \mu\sigma E_z \qquad (0.18)$$

$$\frac{\partial E_z}{\partial y} - \frac{\partial E_y}{\partial z} = -i\omega B_x \qquad \frac{\partial E_x}{\partial z} - \frac{\partial E_z}{\partial x} = -i\omega B_y \qquad \frac{\partial E_y}{\partial x} - \frac{\partial E_x}{\partial y} = -i\omega B_z \qquad (0.19)$$

In the 1-D case, where resistivity varies only with depth, the $\partial/\partial x$ and $\partial/\partial y$ terms will all be zero, resulting in:

$$-\frac{\partial B_y}{\partial z} = \mu\sigma E_x \qquad \frac{\partial B_x}{\partial z} = \mu\sigma E_y \qquad E_z = 0 \qquad (0.20)$$

$$\frac{\partial E_y}{\partial z} = i\omega B_x \qquad \frac{\partial E_x}{\partial z} = -i\omega B_y \qquad B_z = 0 \qquad (0.21)$$

The electric and magnetic fields in the vertical direction will be zero in the 1-D case, and
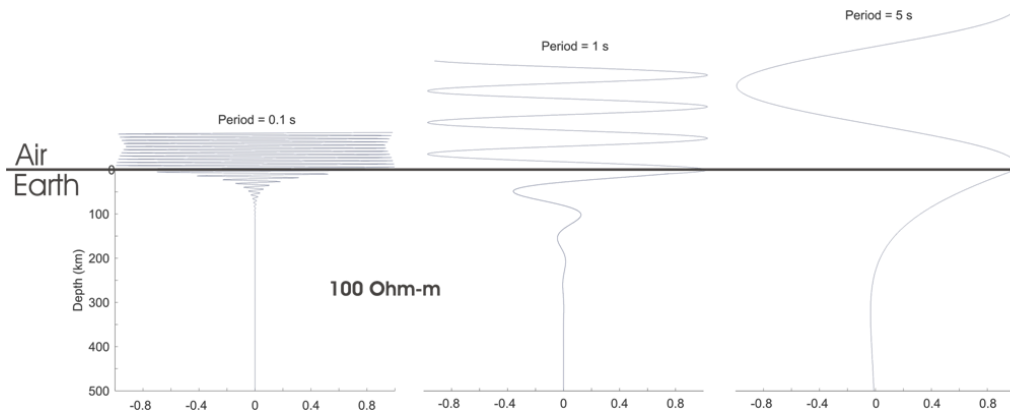
Figure A.0.2: Longer periods (increasing to the right) are sensitive to greater depths in the Earth. The curves represent the real component of an electric field as it passes from the air into the Earth.

the remaining 4 equations are really only 2 equations, since 2 of them are simply rotations of the other 2 (and rotations in the horizontal plane do not matter in the 1-D case; Figure A.0.1). This leaves:

$$\frac{\partial B_x}{\partial z} = \mu\sigma E_y \qquad \frac{\partial E_y}{\partial z} = i\omega B_x \qquad\qquad (0.22)$$

The first thing to see from equation (0.22) is the relationship between perpendicular components of the electric and magnetic field (see Figure A.0.3 for a depiction). Orthogonal components of the electric and magnetic field are coupled, a oscillating magnetic field induces an orthogonal electric field and vice versa.

Up till now we have discussed an Earth model where resistivity varies only in one dimension. However this situation is rarely encountered in the Earth and the 2-D and 3-D scenarios must be considered.

If the Earth has a resistivity structure that varies in two dimensions, then by assuming no changes in resistivity occur in the x direction, the $\partial/\partial x$ terms from (0.18) and (0.19) become zero. This is shown in Figure A.0.4 where the geo-electric strike is defined as the invariant direction and oriented in the x direction. This leaves two sets of equations which are completely independent of one another. The first set is known as the Transverse Electric (TE) mode, and an equation describing E_x can be determined (following
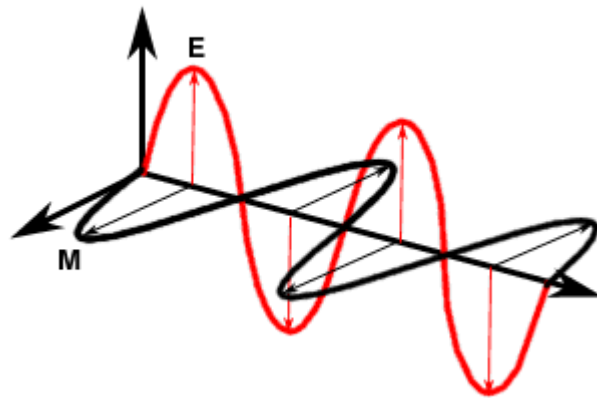
Figure A.0.3: From `http://www.ccrs.nrcan.gc.ca/glossary/index_e.php?id=3104`; A depiction of how the electric and magnetic (M) field interact orthogonally to one another. Notice that this EM wave is travelling in free space, and the electric and magnetic field are in phase with one another (see section 0).

Unsworth; 2010).

$$\frac{\partial^2 E_x}{\partial y^2} + \frac{\partial^2 E_x}{\partial z^2} = i\omega\mu_0 E_x \tag{0.23}$$

The second set of equations is known as the Transverse Magnetic (TM) mode, and result in a partial differential equation describing B_x (again following Unsworth; 2010).

$$\frac{\partial^2 B_x}{\partial y^2} + \frac{\partial^2 B_x}{\partial z^2} = i\omega\mu_0\sigma B_x \tag{0.24}$$

The TE mode corresponds to electric field measurements along strike, while the TM mode corresponds to magnetic field measurements along strike.

Equations (0.23) and (0.24) can be independently solved, which results in two independent solutions for the resistivity of the Earth. Neither of these equations can be solved analytically except for very simple geometries, therefore numerical methods such as finite element or finite difference solutions are used (Unsworth, 2010).

When the Earth has a resistivity structure that varies in three dimensions, no such simplification is possible, and all six equations in (0.18) and (0.19) must be solved simultaneously.
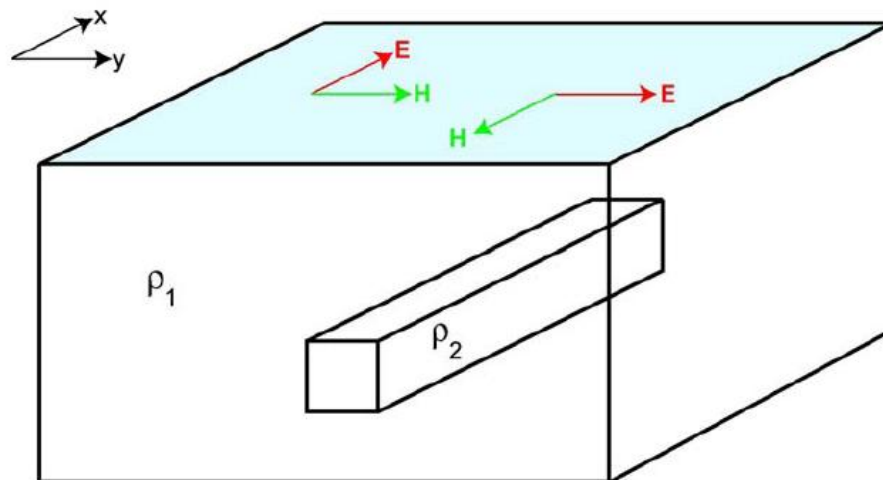
Figure A.0.4: From Unsworth(2010); a depiction of a 2-D region where resistivity only changes in the x direction. Notice that E_x is measured along the low resistivity features (along strike), and E_y is measured across strike.

A.4 Apparent Resistivity and Phase

In MT the measured electric and magnetic fields vary with time. A Fourier transform is often used to convert them into estimates in the frequency domain (see section A-6). This allows us to relate frequency to depth, in a way that is analogous to surface waves in seismic exploration. MT data analysis uses a function called the impedance (**Z**) to remove information about the EM fields. It can be shown that if the impedance is defined as:

$$Z_{xy}(\omega) = \frac{E_x(\omega)}{H_y(\omega)} \qquad (0.25)$$

Then this quantity only contains information about the subsurface structure. Note that H_y is related to B_y through the constitutive relation in (0.10). If we use the definition of E_x from the solution in (0.14), and define H_y in 1-D using (0.22) and (0.10), the impedance becomes:

$$Z_{xy} = -\frac{i\omega\mu_0}{k} = \frac{(1-i)}{\sqrt{2}}\sqrt{\frac{\omega\mu_0}{\sigma}} \qquad (0.26)$$

Equation (0.26) shows that the impedance is not dependant on the amplitude of the EM signal E_0, only on the frequency of the wave, and resistivity of the Earth. To determine Z_{xy}, we need only measure E_x and H_y, transform them into the frequency domain, and divide them as in (0.25). Then re-arranging equation (0.26) the impedance can be related to the resistivity the Earth:

$$\rho_{xy}(\omega) = \frac{1}{\omega\mu_0}\left|Z_{xy}(\omega)\right|^2 = \frac{1}{\omega\mu_0}\left|\frac{E_x(\omega)}{H_y(\omega)}\right|^2 \qquad (0.27)$$

But since the Earth is not actually a uniform half-space with only one resistivity value, the resistivity defined in (0.27) is considered an *apparent* resistivity. The apparent resistivity is an average over a volume which is sampled by the electric and magnetic fields. In depth, this volume is defined by the skin depth equation (0.17).

In free space, the electric and magnetic fields propagate in phase with each other (as shown in Figure A.0.3). Once we introduce a resistive medium, the electric field and magnetic fields travel out of phase with each other. The impedance is a complex number whose argument defines the phase difference as an angle:

$$\Phi_{xy}(\omega) = tan^{-1}[Z_{xy}(\omega)] = tan^{-1}\left[\frac{E_x(\omega)}{H_y(\omega)}\right] \tag{0.28}$$

By this definition, the phase angle will be 0° in free space, and 45° in a half space. It can be shown that when the apparent resistivity increases with period, the phase angle is less than 45°, and while apparent resistivity decreases with period, the phase angle is greater than 45°.

For most applications, MT data is presented as apparent resistivity and phase, since they are more intuitive to imagine than a complex impedance value.

A.5   The Impedance Tensor

So far, we have only looked at the impedance calculated from E_x and H_y (which defines the term Z_{xy}). In the case of a resistivity model that is 1-D, the impedance will not depend on the azimuth of the measured electric field (see Figure A.0.1). In other words, Z_{xy} will be the same as Z_{yx}.

In the case that the Earth has a 2-D resistivity structure (Figure A.0.4), the same will not be true. The values of the impedance in orthogonal co-ordinate systems (Z_{xy} and Z_{yx}) will not be equal because the electric and magnetic fields are being measured either along or across the 2-D structure. For the simplified case where the strike is aligned with the x direction as in Figure A.0.4, Z_{xy} is related to the TE mode, and Z_{yx} is related to the TM mode. For this reason we always measure the electric and magnetic fields in both the x and y directions.

This allows us to estimate four impedance terms: Z_{xy}, Z_{yx}, Z_{xx}, and Z_{yy} which define an impedance tensor:

$$\mathbf{Z} = \begin{bmatrix} Z_{xx} & Z_{xy} \\ Z_{yx} & Z_{yy} \end{bmatrix} \tag{0.29}$$

The impedance tensor defines a relationship between the electric and magnetic fields as

$$\mathbf{E}(\omega) = \mathbf{Z}(\omega)\mathbf{H}(\omega) \tag{0.30}$$

Where $E(\omega) = \begin{pmatrix} E_x(\omega) \\ E_y(\omega) \end{pmatrix}$, $H(\omega) = \begin{pmatrix} H_x(\omega) \\ H_y(\omega) \end{pmatrix}$

Equation (0.30) shows that the impedance tensor (which is dependent on the resistivity of the Earth) is a function which describes how the Earth relates the electric field to the magnetic field in the frequency domain.

A.6   Time Series Processing

Electric field and magnetic field data in MT are measured as a time series. However the analysis developed above considers these fields and the associated impedances in the frequency domain. Impedance estimates are obtained from the very long time series (up to 3 weeks of recording), resulting in apparent resistivity and phase measurements such as the ones presented in section 4.3.

After a transformation of the times series from the time domain to the frequency domain, equation (0.30) can be expanded to two equations relating the electric field to the magnetic field:

$$E_x(\omega) = Z_{xx}(\omega)H_x(\omega) + Z_{xy}(\omega)H_y(\omega) \tag{0.31}$$

$$E_y(\omega) = Z_{yx}(\omega)H_x(\omega) + Z_{yy}(\omega)H_y(\omega) \tag{0.32}$$

$H_x(\omega)$ and $H_y(\omega)$ represent the Fourier transforms of the magnetic field time series, $E_x(\omega)$ and $E_y(\omega)$ are the Fourier transforms of the electric field.

Multiplying (0.31) and (0.32) by the complex conjugates of the Fourier transformed electric and magnetic fields gives 8 equations which can be used to solve for the impedance elements. For example, one of the equations is:

$$\langle E_x^* E_x \rangle = Z_{xx}\langle E_x^* H_x \rangle + Z_{xy}\langle E_x^* H_y \rangle \tag{0.33}$$

Where the * represents the complex conjugate, and the $\langle \ \rangle$ brackets represent averages at specific evaluation frequencies, and are known as cross-powers and auto-powers. The cross power terms are the mixed terms such as $\langle E_x^* H_y \rangle$, and the auto-power terms are the ones multiplied by their own complex conjugate such as $\langle E_x^* E_x \rangle$.

For a 1-D Earth, one solution for Z_{xy} is of the form:

$$Z_{xy} = \frac{\langle E_x H_y^* \rangle}{\langle H_y H_y^* \rangle} \qquad\qquad (0.34)$$

With sufficient averaging, random noise will be cancelled in the cross-power term, but noise in the auto-power term will be multiplied with itself, and enhanced. This results in a large downward bias to Z_{xy}, enhancing noise in the magnetic channel and causing incorrect impedance estimates (Sims et al., 1971).

In order to suppress this effect, magnetic fields from a second MT instrument can be used to calculate the power spectra. This is called the remote reference technique and was developed by (Gamble et al., 1979). Instead of calculating the cross and auto power spectra using the complex conjugate of its own magnetic field, the complex conjugate of a remote magnetic field is used. This means that the auto power spectra is no longer a magnetic field component correlated with itself, but is instead one magnetic field correlated with a magnetic field nearby, and uncorrelated noise should average out.

Noise may also be amplified in the cross power terms when the noise is correlated in more than one channel. This may happen near 60 Hz power lines, or pipelines with cathodic protection. The latter issue has tended to cause the most amounts of problems in collecting MT data in southern Alberta, owing to the large number of (marked and unmarked) natural gas pipelines crisscrossing the province in a dense grid.

Since averaging of noise does not always remove all the effects of outliers, and at times an insufficient amount of data has been collected in order to average out all the noise, robust statistics are used to calculate the impedance values. Egbert & Booker (1986) describe a method of automatically choosing data using a weighted least squares algorithm, which has been utilized for processing the MT data described in this study.

The skin depth equation (0.17) shows that the sensitivity depth of MT data is inversely related to the square root of period. This means that the choice of evaluation frequencies should be chosen logarithmically, and the size of the spectral window (which defines what frequency band is included in the average) should decrease logarithmically with frequency (or increase logarithmically with period). This results in impedance estimates which are logarithmically spaced with period, reflecting the logarithmic frequency – depth relationship.

A.7 Data Dimensionality and the Impedance Tensor

In the absence of noise, the impedance tensor can be used to determine the dimensionality of a region. If the Earth has a 1-D resistivity structure, then Z_{xx} and Z_{yy} will be zero. This is because the electric and magnetic fields should not be associated since the electric field is induced at right angles to the magnetic field (equation (0.22). Also, Z_{xy} and Z_{yx} will be equal to each other as discussed earlier.

Similarly, if the Earth has a 2-D resistivity structure, Z_{xx} and Z_{yy} will also be zero in the strike coordinate frame. However in this case, Z_{xy} and Z_{yx} will not be the same, since 2-D structure is defined by a difference in the *x* and *y* directions).

A 3-D earth can be recognized by significantly nonzero Z_{xx} and Z_{yy} terms in the impedance tensor at all rotation angles. This may happen when the source electric field becomes 'turned' by complex resistivity structure. One could imagine an example where an 'L' shaped conductor turns the electric field around a corner, and causes the *xx* and/or the *yy* electric and magnetic field to become correlated.

In fieldwork, the x-direction is chosen to be magnetic north for simplicity, but if the region has a 2-D resistivity structure then it is unlikely that the geo-electric strike will line up with magnetic north or west. Therefore the impedance tensor must be mathematically rotated into the strike coordinate frame. In order to determine this strike direction (Swift, 1967) rotated the impedance tensor to minimize the diagonal impedance elements in the *Swift strike* direction. If the MT data is truly 2-D, the Z_{xx} and Z_{yy} values will be zero after a rotation into the Swift strike coordinate frame. The *Swift skew* is also used as a normalized measure of how small the diagonal components of the impedance tensor are after rotation (Swift, 1967):

$$Swift\ skew = \frac{Z_{xx} + Z_{yy}}{Z_{xy} - Z_{yx}} \tag{0.35}$$

In practice, Swift skew values below 0.2 have been considered an indication that the data can be considered 2-D in the absence of noise (e.g. (Reddy & Rankin, 1971).This approach works well in the presence of noise with a Gaussian distribution, but coherent noise can bias estimates of the impedance tensor (see section 0), and galvanic distortion can cause high diagonal impedance terms in a 1-D or 2-D region (section 0). Therefore

different methods are often used to estimate the regional strike and/or the dimensionality of a region.

A.8   Galvanic Distortion of MT data

Measured MT is often distorted by small scale, near surface structures. Because this distortion is frequency independent, it is referred to as galvanic distortion. It occurs when the magnitude and direction of the electric fields is changed by near surface conductors.

A common manifestation of galvanic distortion is known as a static shift. This is seen as a magnitude change in the apparent resistivity curve while the phase remains unchanged (Figure A.0.5). This can happen in the presence of a shallow conductor which cannot be resolved by the shortest period (highest frequency) MT data. The shallow conductor lowers the apparent resistivity of the volume sampled by the MT data, but does not appear as a low resistivity feature in the sounding due to its small size and shallow depth.

Static shifts are a major problem in 1-D regions, since there is no way to determine if they are caused by local galvanic distortion, and modelling of the data requires unrealistic models. Static shifts become less of a problem in 2-D or 3-D since a number of stations will be collected in a profile or grid, and the galvanic distortion will cause local effects to
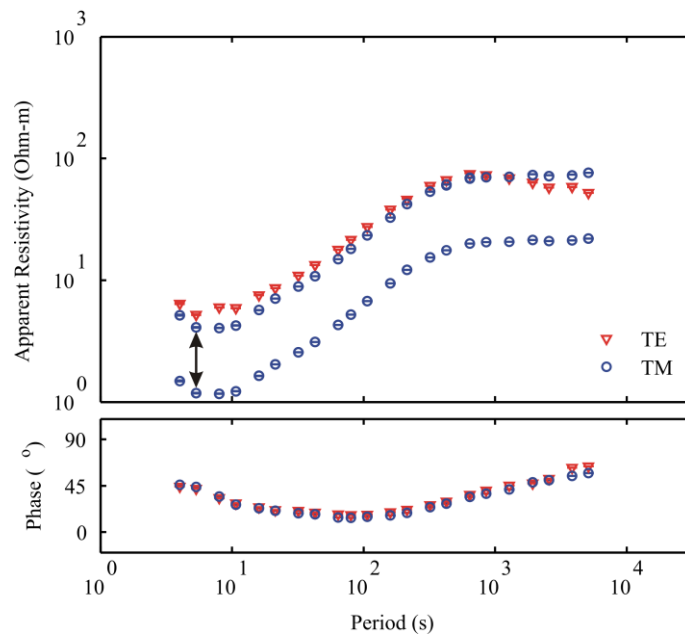

Figure A.0.5: An example of a static shift. Notice that the TM mode curve has been shifted relative to the TE mode, but the phase remains unchanged.

133

each station separately. In this case the local affects can be removed by determining regional trends and removing local outliers (DeGroot-Hedlin & Constable, 1993)

Not only can galvanic distortion cause magnitude changes in apparent resistivity, the direction of the electric field can also be changed. This happens in the presence of an elongated conductor in the near surface (for example and elongated swamp can polarize the electric field in one direction). Figure A.0.5 is an example where the TE and TM curves show a split, indicative of 2-D or 3-D structure. But if the curves are shifted such that they overlap, the data appear to be 1-D.

This can cause a major problem in determining the dimensionality of a region, or determining the regional strike direction. If the region is 2-D, and galvanic distortion causes the electric field to be turned away from the regional strike, an incorrect strike angle will be determined at that station. Therefore in a 2-D region, it is important to analyze the data and find the correct strike direction without galvanic distortion.

One method of finding the regional strike and estimating the dimensionality of MT data was proposed by (Bahr, 1988). He noted that the galvanic distortion tensor is real and non-inductive; therefore in the coordinate frame of the regional strike, the phase in each column of the impedance tensor should be the same, for example:

$$\frac{Real(\mathbf{Z}_{xx})}{Imag(\mathbf{Z}_{xx})} = \frac{Real(\mathbf{Z}_{yx})}{Imag(\mathbf{Z}_{yx})} \tag{0.36}$$

The same is true for the impedance elements in the second column of the tensor (Z_{yy} and Z_{yy}). The angle which either makes (0.36) true, or minimizes the difference between the phase in both columns is known as the *phase sensitive strike*, or the *Bahr strike*. A rotationally invariant parameter known as the *phase sensitive skew* can be used to see if equation (0.37) can be used to describe the data. According to (Simpson & Bahr, 2005), a phase sensitive skew value greater than 0.3 indicates that the region may be 3-D, and the data is not just affected by local 3-D affects. Below 0.3, MT data may be 2-D, although this in itself is not enough of an indicator.

A more common way to separate the regional 2-D regional impedance and the near surface distortion is called tensor decomposition. Tensor decomposition has the advantage of statistically fitting a model to the measured data in a least-squares approach. A number of algorithms have been published but the most popular is that of Groom &

Bailey (1989). They showed that an impedance tensor measured in a region with a 2-D resistivity structure, where the telluric field is affected by a near surface galvanic body, can be described by:

$$\mathbf{Z}_{measured} = \mathbf{RCZ}_{2D}\mathbf{R}^T \qquad (0.37)$$

where $\mathbf{R}$ is a rotation tensor, describing a rotation from the measured coordinate system into the regional strike direction, and $\mathbf{C}$ is a distortion tensor describing the effects of a galvanic body on the 2-D impedance tensor ($\mathbf{Z}_{2D}$). In order to obtain the undistorted 2-D impedance tensor ($\mathbf{Z}_{2D}$) and the regional strike direction (described by $\mathbf{R}$), an estimate of the distortion tensor is made following (Groom & Bailey, 1989) by writing the distortion tensor as the sum of four terms:

$$\mathbf{C} = g\mathbf{TSA} \qquad (0.38)$$

where g represents a scalar gain, $\mathbf{T}$ is termed the *twist*, $\mathbf{S}$ is called the *shear*, and $\mathbf{A}$ represents an anisotropy term. The twist and shear are determinable from the measured impedance, while the gain and anisotropy cannot be uniquely obtained. The term anisotropy is used to represent different concepts. In this case it describes the polarization of the electric field along or across the strike direction due to galvanic distortion, but it can also refer to a material property which causes current to preferentially flow in one direction.

The twist tensor rotates the direction of the electric field, while the shear tensor causes anisotropy at an angle to the regional strike direction. Both the twist and shear are described in terms of an angle, the twist angle and the shear angle. The scalar gain and anisotropy tensor adds to the static shift effect, where g scales the impedance by a constant value without rotating it, and the anisotropy tensor adds to any regional anisotropy which may exist (McNeice & Jones, 2001). The indeterminability of static shifts is represented by the indeterminability of g and $\mathbf{A}$.

In order to estimate the determinable parameters from distorted MT data, the Groom and Bailey (1989) algorithm uses a least squares approach, posing tensor decomposition as an inverse problem. The (Groom & Bailey, 1989), algorithm was extended by (McNeice & Jones, 2001) to fit impedance data at multiple frequencies with a single distortion model. This algorithm computes the twist angle, shear angle, strike angle, and the 2-D impedance tensor that give the best fit to the measured MT impedance data.

The methods above describe an approach to remove galvanic distortion from MT impedance data collected over a regionally 2-D earth. It must be stressed that if the regional response is 3-D, then the tensor decomposition can fail and return incorrect results (Garcia & Jones, 2002). Therefore it is important to classify the regions dimensionality before decomposition.

The impedance tensor can also be distorted by noise. Non-zero diagonal impedance terms are never observed in field data, even when there are no galvanic effects, and the region is 2-D. This is partly due to how impedance estimates are obtained from the originally measured time series (see section 0).

A.9   Induction Vectors

Induction vectors are derived from vertical magnetic fields measured during MT data collection. They are defined as the ratio of vertical to horizontal magnetic fields. Maps of induction vectors point away from (in the Weise convention; (Wiese, 1962), or towards conductors (in the Parkinson convention; Parkinson, 1959).

As discussed in section A.7, a 1-D Earth will result in no vertical magnetic fields, but if there are lateral variations in resistivity, then the current distribution in the Earth will be non-uniform and cause the horizontal magnetic field to tip into the vertical field (Simpson & Bahr, 2005). This is why the ratio of vertical to horizontal magnetic field is also called the tipper. Larger vectors represent a larger tipping of the magnetic field, and correspond with a large resistivity gradient.

A.10   Data Modelling

Once the impedances have been calculated, and the dimensionality and strike angle determined, the next step in MT data analysis is to find a resistivity model of the Earth which can explain the data. This is done through both forward modelling, and inverse modelling.

Forward modelling involves the calculation of synthetic data d from a resistivity model m using a forward operator F as

$$F[m] = d \tag{0.39}$$

136

In MT modelling, the model m is a model of electrical resistivtiy in the region of interest, and the synthetic data d is either the predicted impedance or apparent resistivity and phase resulting from the model.

Finding the forward operator F involves solving the equations derived from Maxwell's laws in section 0 (equation (0.22) for 1-D, (0.23) - (0.24) for 2-D, and (0.18) - (0.19) for 3-D). If the earth has a 1-D structure then an analytic forward solution can be derived (Wait, 1954). However, if the Earth has a 2-D or 3-D resistivity structure, then the forward problem will generally require a numerical solution. Common approaches to this include the finite difference or finite element methods.

One approach to forward modelling is to guess an initial resistivity model, calculate the synthetic response, and then determine how well the synthetic MT data matches the measured MT data. If the fit is not statistically significant, then the model is updated and new synthetic data is generated. This process can go on for many iterations, and it is a time consuming process to manually change the model each time.

This iterative process can be automated with a computational approach called inversion. Inversion refers to the process of 'inverting' equation (0.39) to solve for the model m from the data d. This approach is much quicker than forward modelling, and the inversion algorithm finds a model automatically to fit the measured data. This process is problematic, since it can be shown that the MT inverse problem is both non-linear and inherently non-unique. Finding a model automatically requires an inversion methodology which allows the algorithm to find a single model which not only fits the data, but can also be considered a robust result.

A.10.1 Occam's Inversion

In MT, inversion philosophies are generally based on Occam's razor (Constable et al. 1987), where the simplest solution is found by requiring that the misfit between measured and predicted data is minimized and imposing additional constraints such as minimizing the spatial roughness of the model. The idea is that since MT measures diffusive fields, rough boundaries between layers cannot be detected accurately. Rough models can be generated to fit the data, but are not required by the data in most cases, therefore to find a unique model (or as unique as possible given data error), the roughness should be minimized.

In order to construct the inversion, a functional U which represents the value to be minimized is constructed:

$$U(\boldsymbol{m}, \lambda) = [(\boldsymbol{m} - \boldsymbol{m}_0)^T \boldsymbol{C}_m^{-1}(\boldsymbol{m} - \boldsymbol{m}_0)]$$
$$+ \lambda^{-1}[(\boldsymbol{d} - \boldsymbol{F}[\boldsymbol{m}])^T \boldsymbol{C}_d^{-1}(\boldsymbol{d} - \boldsymbol{F}[\boldsymbol{m}]) - X^2] \tag{0.40}$$

Where X represents the desired misfit (for most cases the desired misfit is 1 (Constable, Parker, & Constable, 1987), $\boldsymbol{C}_d$ is the data covariance matrix, $\boldsymbol{C}_m$ is the model covariance matrix, $\boldsymbol{m}$ is the resistivity model, and $\boldsymbol{m}_0$ is the prior model.

λ^{-1} is known as the Lagrange Multiplier, and represents a trade-off between the first and second term in (0.40). Larger values will place more emphasis on the misfit (the second term), while smaller values will put more emphasis on the roughness (first term).

For this study, U was minimized using the algorithms and software developed by (Siripunvaraporn et al., 2005) for the 3-D inversions, and (Rodi & Mackie, 2001) for the 2-D inversions.

Both algorithms use an iterative method to linearize $\boldsymbol{F}[\boldsymbol{m}]$. The 3-D algorithm minimizes U using a data space approach (instead of the model space) in order to limit the amount of memory required by the inversion (which is the biggest barrier to 3-D MT modelling). The 2-D inversion uses a non-linear conjugate gradient algorithm to solve for a realistic model which is both smooth and fits the data. The 2-D algorithm can invert the TE, TM, and induction vector data for one model, or it can solve separate models for each mode (and any combination of modes).

Since in 3-D there are no TE and TM modes (they are mixed), the 3-D algorithm inverts the impedance data, and recent developments have allowed the induction vector data to be included in the inversion as well (Siripunvaraporn & Egbert, 2009).

Various parameters can be used to control how the two algorithms change the model between iterations, and how they choose the best model. The corresponding modeling in Chapter 3 includes an explanation of the parameters used by each algorithm.